

Title	Investigation of numerical atomic orbitals for first-principles calculations of the electronic and transport properties of silicon nanowire structures
Authors	Sharma, Dimpy
Publication date	2013
Original Citation	Sharma, D. 2013. Investigation of numerical atomic orbitals for first-principles calculations of the electronic and transport properties of silicon nanowire structures. PhD Thesis, University College Cork.
Type of publication	Doctoral thesis
Rights	© 2013, Dimpy Sharma. - <a href="http://creativecommons.org/licenses/by-nc-nd/3.0/">http://creativecommons.org/licenses/by-nc-nd/3.0/</a>
Download date	2024-04-20 07:12:21
Item downloaded from	<a href="https://hdl.handle.net/10468/1136">https://hdl.handle.net/10468/1136</a>

Ollscoil na hÉireann  
NATIONAL UNIVERSITY OF IRELAND



**Investigation of numerical atomic orbitals for first-principles calculations of the electronic and transport properties of silicon nanowire structures**

by

**Dimpy Sharma**

January 2013

Supervisor: **Dr. Giorgos Fagas**

Head of Department: **Prof. Michael Morris**

*A thesis presented to*

*The National University of Ireland, Cork*

*for the degree of*

**‘Doctor of Philosophy’ (Ph.D.)**

*in Chemistry*



Tyndall National Institute

University College Cork

Cork, Ireland

## Contents

<b>Acknowledgements .....</b>	<b>4</b>
<b>Abstract.....</b>	<b>5</b>
<b>Dissemination.....</b>	<b>6</b>
<b>Chapter 1: Introduction .....</b>	<b>7</b>
1.1 Semiconductor nanowires as device nanomaterials .....	7
1.2 State-of-the-art experiments .....	8
1.3 First-principles calculations as a design tool .....	12
1.4 Overview of the thesis .....	15
<b>Chapter 2: Background to methods.....</b>	<b>20</b>
2.1 Chapter introduction .....	20
2.2 Electronic structure from first-principles .....	20
2.2.1 Theoretical foundations of DFT.....	22
2.2.2 Basis sets for solving the Kohn-Sham equations .....	27
2.2.2.1 Plane wave basis sets.....	28
2.2.2.2 Numerical atomic orbitals basis sets.....	29
2.3 Quantum theory of transport .....	31
2.3.1 Landauer formalism .....	32
2.3.2 S-matrix.....	37
2.3.3 Self-consistency using NEGF.....	40
2.4 Computational packages.....	41
2.4.1 Quantum Espresso.....	41
2.5.2 OpenMX .....	42
2.5.3 TiMeS .....	43
<b>Chapter 3: Structural and electronic properties of hydrogenated and hydroxylated SiNWs .....</b>	<b>46</b>
3.1 Chapter introduction .....	46
3.2 Benchmarking of numerical atomic orbitals .....	48
3.2.1 Hydrogenated silicon nanowires .....	48
3.2.2 Hydroxylated silicon nanowires.....	56
3.3 Analysis of band structure properties .....	61
3.4 Transferability of optimised numerical atomic orbitals .....	65
3.5 Conclusions .....	67

<b><i>Chapter 4: Structural, electronic and transport properties of doped silicon nanowires.....</i></b>	<b><i>68</i></b>
4.1 Chapter introduction .....	68
4.2 Electronic properties of doped silicon nanowires .....	70
4.3 Scattering properties of n- and p-type dopants in silicon nanowires .....	79
4.4 Conclusions .....	85
<b><i>Chapter 5: Basis set dependence of transport properties and electrical device characteristics in Si nanowire setups.....</i></b>	<b><i>86</i></b>
5.1 Chapter introduction .....	86
5.2 Computational details.....	90
5.3 Transport properties.....	91
5.4 Electrical characteristics.....	94
5.5 Conclusions .....	100
<b><i>Chapter 6: Hole mobility in low-doped silicon nanowires .....</i></b>	<b><i>102</i></b>
6.1 Chapter introduction .....	102
6.2 Electronic structure and transmission properties .....	104
6.4 Hole mobility .....	109
6.5 Conclusions .....	115
<b><i>Chapter 7: Concluding remarks and outlook .....</i></b>	<b><i>116</i></b>
<b><i>8. Bibliography .....</i></b>	<b><i>121</i></b>

## **Acknowledgements**

I would like to express my extraordinary gratitude to my supervisor, Dr. Giorgos. Fagas, without whom this work would have been impossible. Throughout my PhD period, he provided encouragement, sound advice, good teaching, good company, and lots of good ideas. His patience, vast knowledge, keen observation and sheer enthusiasm were always inspiring for me.

I would like to address my special thanks to Dr. Simon D. Elliot, Dr. Justin D. Holmes, Dr. Baruch Feldman and Dr. Jim Greer for their helpful discussions during my PhD. I am indebted to many members of the Electronics Theory Group/Computational Modelling Group for providing a stimulating and fun environment in which to learn and grow.

I also thank all members of IT department of Tyndall National Institute, and their help in many occasions are acknowledged. I also thank Irish High End Computing Systems and Science Foundation Ireland, for the computational facilities. I acknowledge the financial support derived from the Science Foundation Ireland grant number 06/IN.1/I857.

Lastly, and most importantly, I wish to thank my parents Dr. Lakhan. C. Sharma and Mrs. Arati Sharma and my brother Apurba. To them I dedicate this thesis.

## Abstract

This thesis is focused on the application of numerical atomic basis sets in studies of the structural, electronic and transport properties of silicon nanowire structures from first-principles within the framework of Density Functional Theory. First we critically examine the applied methodology and then offer predictions regarding the transport properties and realisation of silicon nanowire devices. The performance of numerical atomic orbitals is benchmarked against calculations performed with plane waves basis sets. After establishing the convergence of total energy and electronic structure calculations with increasing basis size we have shown that their quality greatly improves with the optimisation of the contraction for a fixed basis size. The double zeta polarised basis offers a reasonable approximation to study structural and electronic properties and transferability exists between various nanowire structures. This is most important to reduce the computational cost. The impact of basis sets on transport properties in silicon nanowires with oxygen and dopant impurities have also been studied. It is found that whilst transmission features quantitatively converge with increasing contraction there is a weaker dependence on basis set for the mean free path; the double zeta polarised basis offers a good compromise whereas the single zeta basis set yields qualitatively reasonable results. Studying the transport properties of nanowire-based transistor setups with  $p^+ - n - p^+$  and  $p^+ - i - p^+$  doping profiles it is shown that charge self-consistency affects the I-V characteristics more significantly than the basis set choice. It is predicted that such ultrascaled (3 nm length) transistors would show degraded performance due to relatively high source-drain tunnelling currents. Finally, it is shown the hole mobility of Si nanowires nominally doped with boron decreases monotonically with decreasing width at fixed doping density and increasing dopant concentration. Significant mobility variations are identified which can explain experimental observations.

## Dissemination

1. D. Sharma and G. Fagas: ‘A study of atomic orbital basis sets for doped silicon nanowires’, J. Phys.: Conf. Ser. **367**, 012003 (2012) [6 pages]
2. D. Sharma, H. Arefi, and G. Fagas: ‘Atomic basis sets for first-principles studies of Si nanowires’, Comp. Theoret. Chem. **991**, 32 (2012) [8 pages]
3. D. Sharma, L. Ansari, B. Feldman, M. Iakovidis, J. C. Greer, and G. Fagas: ‘Transport properties and electrical device characteristics with the TiMeS computational platform: basis set dependence in silicon nanowires’, *accepted for publication in Journal of Applied Physics* (2013)
4. D. Sharma and G. Fagas: ‘Hole mobility in low-doped Si nanowires limited by neutral impurity scattering’, *in preparation*

## **Chapter 1: Introduction**

### **1.1 Semiconductor nanowires as device nanomaterials**

All material properties, e.g., electrical, magnetic and optical properties, are strongly influenced by structure and this is even more evident at the nanoscale. As a result nanostructured materials have attracted increased interest by the scientific world. Specifically, nanowires – defined as one dimensional rods with diameter of 100 nanometres or less – are the topic of my thesis and these can be metallic, semiconducting or insulating depending not only on their composition but also on the cross-section size and surface treatment. Because of their two dimensional confinement nanowires exhibit intriguing behaviour, e.g., nanowires made of bulk semimetals such as Bi or Sn show semiconducting behaviour below a threshold diameter.<sup>1,2</sup>

Herein the focus is on semiconductor nanowires which have been shown to be excellent candidates as nanomaterials for electronic devices such as nanowire-based solar cells, batteries, biosensors, transistors, and photodiodes (a detailed literature review follows below).<sup>3-18</sup>

In particular, silicon nanowires (SiNWs) with their high surface to volume ratio can be fabricated in a CMOS-compatible process<sup>9-11</sup> and are ideal for integration in “end-of-roadmap” technologies. Moore’s law implies that the number of transistors on an integrated circuit doubles in approximately every two years.<sup>9</sup> Up to the beginning of the 21<sup>st</sup> century physical scaling was the dominant driver. More recently, increased power consumption, technical challenges and cost led to the introduction of technology boosters such as strained silicon and high-k dielectric materials to



enhance the charge carrier mobility and reduce the gate leakage, respectively. However, as aggressive scaling continues the International Technology Roadmap for Semiconductors (ITRS) predicts that metal-oxide-semiconductor field-effect-transistors (MOSFETs) will reach sub-10 nm dimensions in 2018. Sub-deca nanometer devices show short-channel and quantum tunneling effects that degrade device performance.<sup>19</sup> To address these challenges, new transistors use nanowires in ultra scaled FET designs.<sup>8,20</sup> These consist of ultrathin channels surrounded by a gate dielectric and allow for better electrostatic control and body inversion.<sup>21</sup> The Intel Corporation has already started utilising multigate fin-like FETs in the design of its Ivy Bridge microprocessors which have been in production since 2012.

## 1.2 State-of-the-art experiments

Thanks to advanced growth and fabrication techniques, bottom-up and top-down nanowire devices have been miniaturised down to ultrasmall diameters. SiNWs of diameter 1-7 nm have been characterised by Ma *et al.*<sup>22</sup> and the device characteristics of transistors with a gate wrapped around a cylindrical Si core of diameter less than 5nm have been measured.<sup>23</sup> Most recently, using undoped SiNW multifunctional devices, including Schottky diode and logic gates, have been fabricated and their electron transport properties have been studied.<sup>24</sup>

SiNWs are fabricated by both top down and bottom up approaches. Top-down approaches are based on optical<sup>25</sup> and electron beam lithography,<sup>26</sup> ion implantation,<sup>27</sup> and etching.<sup>28</sup> The bottom up approach mostly includes catalyst-assisted growth<sup>29,30</sup> using vapor-liquid-solid technique,<sup>31</sup> laser ablation,<sup>30</sup> chemical vapour deposition (CVD),<sup>32</sup> plasma CVD,<sup>33</sup> solution-based<sup>34,35</sup> and thermal evaporator reactor methods.<sup>36</sup> Top down fabrication can produce SiNWs of any

orientation whereas the orientation of catalytically grown wires depends on the diameter. The performance of SiNWs can be enhanced by doping for applications in solid-state devices. Experimentally the most common dopants of interest are P and B which are found to form *n*- and *p*-type active material.<sup>37,38</sup> The use of doped SiNWs has been demonstrated in applications ranging from energy harvesting and storage<sup>36</sup> and ultrasensitive low-power sensors<sup>39,40</sup> to ultrascaled field-effect transistors.<sup>8,41</sup>

Low cost and high efficiency p-n junction SiNW photovoltaics have been fabricated using both simple self-assembly and top-down fabrication. In either case, it has been found that there is an enhancement in light trapping due to higher absorption in nanowire arrays<sup>42</sup> and silicon photovoltaic devices that show tuneable characteristics have been recently fabricated based on core-shell *p-i-n* nanowires with different cross-sectional morphology.<sup>43</sup> Solar cells made with radial heterostructures of nanowires show promising performance with power conversion efficiencies at 10% (expected to reach as high as 18%).<sup>44</sup> Recently, significant thermoelectrics efficiency was shown in surface-treated silicon nanowires (SiNWs)<sup>3</sup>. Another team of US researchers has shown that the use of SiNWs in a lithium rechargeable battery doubles the capacity of the battery.<sup>45</sup>

Nanowires have been proposed with great success as field-effect-transistor (FET) devices for highly-sensitive, selective (bio-) chemical sensing with ultra small power consumption of the order of a few nanowatts.<sup>46</sup> SiNW FET-based biosensors have been employed in the detection of proteins, DNA sequences, small molecules, cancer biomarkers and virus infections.<sup>6</sup> Using top down fabrication with CMOS compatibility, they have been successfully designed for ultra sensitive detection of nucleic acids and diagnosis of avian influenza.<sup>47</sup> In another example, they have been used to detect viruses by using antibody functionalized nanowires<sup>48</sup> and as ultra-

sensitive label-free biosensor immunodetection.<sup>49,50</sup> The sensitivity and selectivity of the device can be improved by surface functionalisation, dopant type and doping level optimisation along with other design such as the nanowire surface-to-volume ratio and dual gates.<sup>51</sup> In one of the recent experiments it has been demonstrated that back-gated silicon nanowire FET gives ultrahigh sensitivity and selectivity in sensing targeted DNA in biological species. By optimising the sensor at low buffer solution, these sensors showed good percentage of current response in the subthreshold regime and improved DNA detection.<sup>52</sup> Also surface modification of hydroxylated SiNWs has produced fluorescence sensors for detecting Cu (II), thereby establishing a method which can be helpful for optical biochemical sensing of different analytes.<sup>53</sup>

Work performed in the Lieber group has shown the utility of SiNWs in computation for digital electronics by demonstration of logical gates.<sup>54</sup> Nanowires have also been used in tunnel FET geometries in order to decrease the subthreshold slope and realise low-power electronics with better electronic switches.<sup>15</sup> However, difficulties are associated with low on-currents, abrupt junction fabrication and only local improvement of the subthreshold slope over a limited voltage range. On the other hand, ultrasmall transistors based on conventional heterojunctions ( $p^+-n-p^+$  or  $n^+-p-n^+$  doping profiles) present short channel effects. This led to the proposal of multigate MOSFETs nanowire-based transistors since narrow-diameter MOSFETs surrounded by gate dielectrics provide the best electrostatic control of the channel.<sup>21</sup> For these designs the difficulty to control the dopant profile is another complication that needs to be addressed. Recently, a homogeneously doped device ( $n^+-n^+-n^+$  or  $p^+-p^+-p^+$ , i.e., without junctions) has been proposed. This junctionless transistor has been shown to yield ideal MOSFET characteristics.<sup>21,55</sup> The channel length and

diameter in these devices are 40 nm and 20 nm, respectively. The question remains whether these nanowire-based transistors can be aggressively scaled towards the atomic scale.

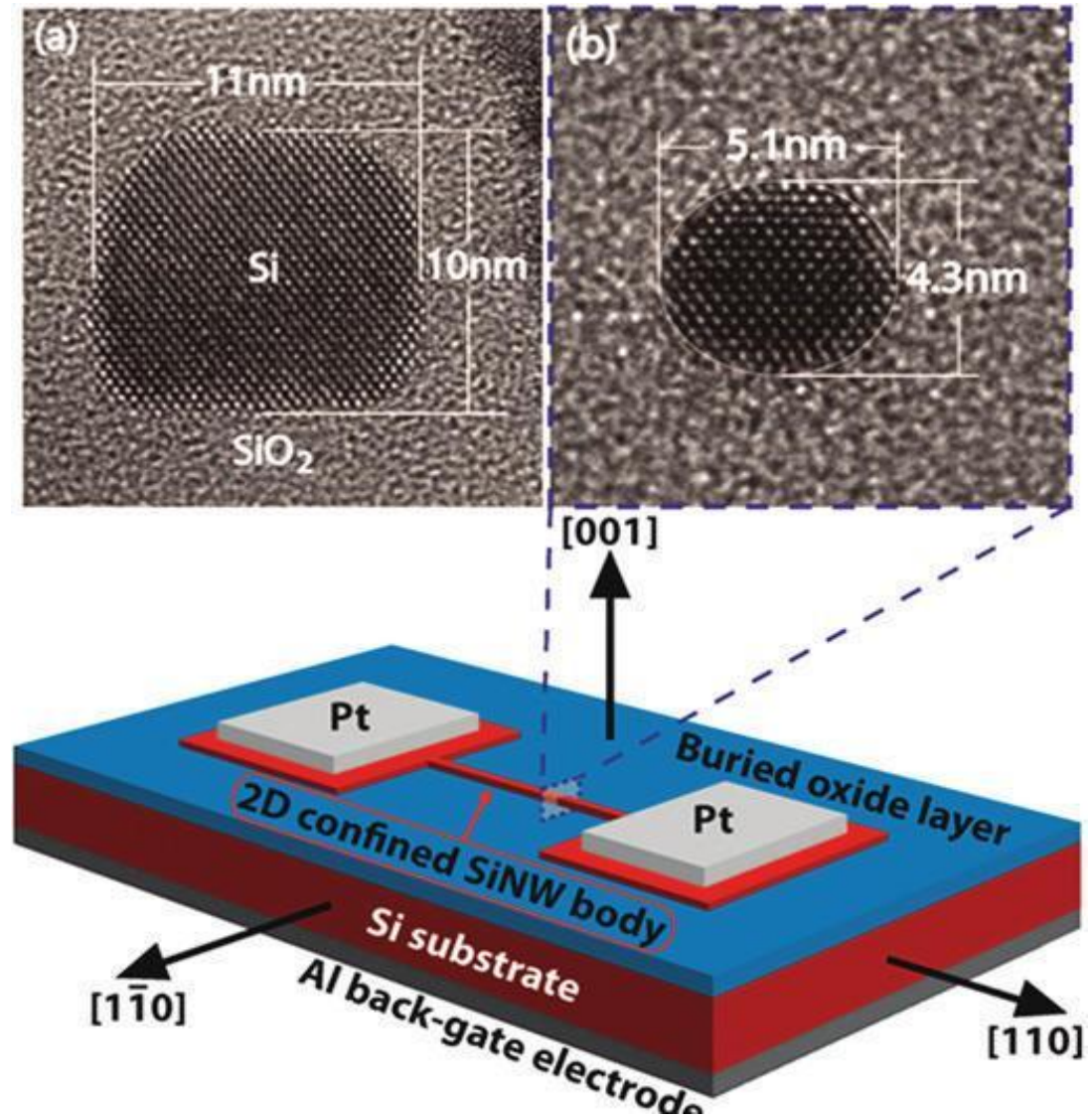


**Figure 1.2:** Schematic of three dimensional back-gated SiNW FET patterned on a silicon-on-insulator (SOI) substrate of buried oxide (BOX) (a) lithographically fabricated sub-5 nm thick Si nanowire field-effect transistors before oxidation (b) after oxidation<sup>26</sup>.

Regarding the electrical performance of SiNWs, it has been found that during the fabrication process the removal of surface defects improves and stabilizes the electrical conductivity.<sup>56</sup> Also, highly doped accumulation mode gate all around (GAA) SiNW FET of sub-5 nm SiNWs have been fabricated using top-down silicon-on-insulator (SOI) platform with high tensile strain which boosts the carrier mobility.<sup>57</sup> The current voltage characteristics have been recently studied experimentally in silicon nanowire transistors of diameter 3-5 nm (shown in Figure 1.2). In Ref. 26 it is found that SiNW FETs with sub-5 nm channel width and nominally doped with boron (doping density  $2 \times 10^{15} \text{ cm}^{-3}$ ) show improvement in drive current with high on/off ratio and low drain current leakage. The authors find peak mobility of  $1200 \text{ cm}^2/(\text{Vs})$  for a channel oriented along the  $\langle 110 \rangle$  crystallographic direction. This is larger than a nanobelt control sample and it is due to strong one dimensional quantum confinement in the nanowire FET as compared to the two dimensional nanobelt.

### **1.3 First-principles calculations as a design tool**

To be able to design better experiments or interpret measured results, a better understanding of the materials properties and their relation to measured quantities is required. In particular, for the development of electronic devices with improved performance the interplay between structural and electronic properties and their effect on electron transport behaviour in ultrathin SiNWs are essential to address. For the length scales of interest experimental data were difficult to obtain since the traditional trial-and-error approach can be challenging, time-consuming and expensive. To this end, modelling and device simulations can provide complementary guidance by probing yet unexplored regions and phenomena.

There have been plenty of theoretical studies on SiNWs that employ a range of continuum to atomic-scale models. But as dimensions shrink to the order of the Fermi wavelength of the electrons, the effective masses and other properties of the materials can change dramatically and interface/surface effects can dominate; hence, atomic-scale effects need to be taken explicitly into account. In particular, electronic structure calculations from first-principles have become an indispensable tool in the analysis of atomic and molecular properties, the design and characterisation of solid-state (opto-) electronic devices and the search of new materials. The challenge is to provide an efficient yet accurate enough answer to predict the materials and device properties.

There are numerous first-principles studies on the electronic structure of semiconductor nanowires made of various materials. Due to the increased surface to volume ratio, significant variations are expected in the electronic properties depending on the geometrical shape of the cross-section and growth orientation of the nanowire axis,<sup>58-61</sup> defects and surface roughness,<sup>62-64</sup> passivation and surface termination by different functional groups.<sup>65-67</sup> The effect of electron-phonon coupling has been investigated<sup>68,69</sup> and found to give rise to anisotropic deformation potentials.<sup>69</sup> Below, a brief presentation on the theoretical results obtained for very small diameter SiNWs (typically of the order of 5 nm and smaller) are given.

SiNWs can be found in different preferential orientations  $\langle 100 \rangle$ ,  $\langle 110 \rangle$ ,  $\langle 111 \rangle$ ,  $\langle 112 \rangle$  based on their fabrication technique. For catalytically grown nanowires it has been experimentally demonstrated that SiNWs with  $\langle 110 \rangle$  orientation are favourably grown at smaller diameter (3 to 10-15 nm) while at diameters larger than 30 nm  $\langle 111 \rangle$  is the most stable orientation.<sup>70</sup> In theoretical studies from first principles it was found that the stability of SiNWs at different orientations varies

depending on their surface passivation as well as diameter. For example the  $\langle 111 \rangle$ -orientation has been shown to be the most stable orientation for unpassivated SiNWs at diameter 6 nm.<sup>67</sup> However, the  $\langle 110 \rangle$ -orientation was most stable for non-hydrogenated SiNWs of diameter 2-5 nm.<sup>71</sup> Theoretically it was found that 1.2 nm diameter of  $\langle 110 \rangle$  oriented SiNWs with hydrogen passivation are the most stable structures.<sup>72</sup> A strong dependence of the band gap on surface functionalization group in SiNWs has been identified using first-principles. Surface terminating groups cause strong hybridization effects in the valence band which yield band gap changes of up to 1 eV for a fixed diameter.<sup>65</sup>

The presence of dopants has a huge impact on the electronic properties not only by tuning the Fermi energy but also as a source of resonant scattering. The effect of doping in the electronic and transport properties of silicon nanowires has been discussed both theoretically and experimentally. Different behaviour can be seen depending on the radial distribution of the dopants along the nanowire cross-section. For example if the dopant is located in the body of the nanowire it can cause back scattering. This is absent if the dopant is located near the surface while it couples to dangling bonds at the surface.<sup>73,74</sup> A recent experiment reveals different segregation behaviour of B and P dopants which resulted in varying radial distributions in SiNWs.<sup>75</sup> Nevertheless, the carrier mobility in SiNWs is expected to be affected by different scattering mechanisms including acoustic phonon scattering,<sup>76</sup> neutral dopant scattering, ionised impurity scattering<sup>77</sup> and surface roughness scattering. Electron-phonon scattering depends on the nanowire and device dimensions as well as the nanowire axis.<sup>61,76,78</sup> It has been confirmed that when quantum confinement was not significant in SiNWs of diameter 30-50 nm, scattering from ionised dopants or phonons limited the carrier mobility.<sup>78</sup> In ultrascaled devices the interplay

between the various scattering mechanisms is expected to depend on orientation and cross-section and surface properties.

The effect of surface confinement on the low-field mobility of  $\langle 110 \rangle$  p-type Si nano-channels has been reported. Using first-principles and the Boltzmann transport method was found that  $\langle 110 \rangle$  and  $\langle 110 \rangle$  channels show a significant enhancement in hole mobility compared to the  $\langle 100 \rangle$  channel.<sup>79</sup> In some recent theoretical work, the current in a SiNW transistor has been shown to improve. By suppressing the quantum mechanical coupling between heavy and light holes in p-type SiNWs doubling of the current is observed in devices with channel width at 5 nm.<sup>80</sup> It has also been shown that SiNWs oriented along the  $\langle 110 \rangle$  direction support more efficient current processes<sup>76,81</sup> and longer scattering lengths.<sup>82</sup> Previously, transistor behavior in junctionless nanowire-based gate-all-around (GAA) setups with just a 3 nm gate length was predicted.<sup>83,84</sup> The excellent device characteristics at such ultrascaled dimensions have been recently confirmed.<sup>153</sup>

## 1.4 Overview of the thesis

Herein first-principles methods were employed in the Density Functional Theory (DFT) framework<sup>85</sup> to calculate the electronic structure of nanowires and extract a Hamiltonian matrix description for charge carrier transport studies. The aim is to:

- Critically examine the use of numerical atomic basis sets in studies of the structural, electronic and transport properties of silicon nanowire materials
- Establish the basis set dependence in obtaining electrical devices characteristics
- Apply finally the computational tools in predictive simulations.



DFT, despite the limitations of its various approximations, is by now a fairly well-established tool in electronic structure calculations. The use of a proper basis set has always been a most basic issue as well as challenging from the viewpoint of accuracy and computational cost. The details of Plane waves have been discussed in latter part of the thesis, which is at section 2.2.2.1. Plane waves (PWs) provide stable convergence and may be very accurate and efficient for various systems up to 1000 electrons.<sup>86,87</sup> But they present serious limitations when considering larger systems as PW basis sets tend to be large, thereby, needing very high memory for storage as well as calculation time for matrix operations. Also, plane waves are extended in space and are not well suited for transport calculations where the open boundary conditions are better captured by localised basis functions. An alternative is to use orbitals localised at the various atomic sites. Such atomic orbital (AO) basis sets have been extensively studied in Quantum Chemistry and used to investigate the properties of atoms and molecules. Their use in solid state has been more recent in linear-scaling implementations.<sup>88-91</sup> The drawback is that AOs are more difficult to improve systematically for quantitative predictions. However, their transferability in a different environment cannot be guaranteed. The construction of numerical atomic orbitals (NAOs) and their on-the-fly optimisation promises a remedy. Several schemes exist to obtain NAOs. These have been shown to be relatively accurate and extremely efficient in various materials applications but additional studies are required to reach the same level of confidence as for PW predictions.<sup>92</sup>

The above issues touched upon the first part of this thesis where it was focused on basis set investigation in an effort to identify the most appropriate atomic basis set for studies of silicon nanowires based on a compromise between computational demands and predictability. Atomic basis sets have been commonly used in studies

of electronic structure and transport properties of SiNWs and the size of the basis set were ranged typically from a minimal to a double zeta polarised basis set. However, there has been no report that compares variations between the various expansions and that benchmarks results against plane wave calculations. The systematic improvement of atomic orbitals with respect to the basis size or optimisation has not been studied. In addition, the basis set dependence on transport properties has attracted little attention with relatively few exceptions.<sup>94,95</sup>

Herein, the first systematic validation of numerical atomic orbitals for SiNWs with oxygen and dopant impurities and the results are used to study charge-carrier scattering from impurity atoms and the transport characteristics of ultrascaled junctioned nanowire-based transistors. Variations of the mobility by neutral impurity scattering are discussed as a function of dopant position and nanowire diameter. It is also found that charge self-consistency affects the device characteristics more significantly than the choice of the basis set. Junctioned transistor designs would likely fail to keep carriers out of the channel as these devices yield source-drain tunneling currents of the order of 0.5 nA and 2 nA for p-n-p junction and p-i-p junction, respectively.

The rest of the thesis is divided into the following chapters, which is briefly described here:

- In Chapter 2, the theoretical background on calculation methodologies of electronic structure and electron transport properties is provided followed by a short description of the computational implementations have been used.
- In Chapter 3, numerical atomic orbital basis sets are benchmarked against plane waves and an extensive comparison between various contraction

schemes are given. The aim is to build a solid background for calculations on SiNWs using numerical atomic orbitals. Results on total energy calculations and electronic structure properties of various ideal structures including hydrogenated and hydroxylated SiNWs are presented in detail followed by band structure analysis to obtain the effective mass and group velocity of subbands.

- In Chapter 4, the results of Chapter 3 is used and is extended to first-principles calculations of doped silicon nanowires. Boron, phosphorous, gallium and arsenic atoms were used as dopants. Structural and electronic properties are studied and the performance of optimised basis sets is benchmarked. The transferability of numerical atomic orbitals for studies of silicon nanowires is tested by applying in nanowires with different orientations. In this chapter, we also provide a first discussion on the generic effect of n-and p-type dopants on the transport properties of electrons and holes.
- In Chapter 5, the studies of chapter 3 is extended to discuss the basis set dependence on the transport properties of non-ideal nanowire structures and the device characteristics of conventional transistor setups based on nanowire structures. The basis set dependence was compared against the effect of charge self-consistency on the device characteristics. Finally, predictions regarding the performance of ultrascaled (3 nm length) nanowire-based transistors with p-i-p and p-n-p doping profiles are given.
- In Chapter 6, motivated by the recent results of Ref. 26 we study in detail the scattering by boron impurities in SiNWs. By placing the dopant in different positions on the cross-section and varying the nanowire width, firstly the

transmission properties across single impurities is calculated. Then these results were used and an approximate method based on scattering from independent impurities and the relaxation-time to predict variations in the mobility.

- The thesis is concluded in Chapter 7 with a discussion of the findings and the outlook of this PhD work.

## Chapter 2: Background to methods

### 2.1 Chapter introduction

This chapter provides the theoretical background to the computational methodologies employed later in the thesis. The chapter consists of three parts. In Section 2.2, the first-principles approach for structural and electronic structure calculations was described. These are applied throughout the core chapters of the thesis where new results are presented (Chapters 3-6). Following a brief introduction to the DFT framework, the particular focus is on the distinction between plane wave and numerical atomic basis sets. In the second part (Section 2.3), the theoretical approach to studies of electron transport properties (applied in Chapters 4-6) and the relation to current-voltage characteristics are discussed (applied in Chapter 5). The chapter concludes with Section 2.4 where the computational implementations that have based our results are described in more detail.

### 2.2 Electronic structure from first-principles

The many body Hamiltonian that governs the behaviour of interacting electrons and nuclei is given as follows

$$\hat{H} = -\frac{\hbar^2}{2m_e} \sum_i \nabla_i^2 - \sum_{i,I} \frac{Z_I e^2}{|\vec{r}_i - \vec{R}_I|} + \frac{1}{2} \sum_{i \neq j} \frac{e^2}{|\vec{r}_i - \vec{r}_j|} - \sum_I \frac{\hbar^2}{2M_I} \nabla_I^2 + \frac{1}{2} \sum_{I \neq J} \frac{Z_I Z_J e^2}{|\vec{R}_I - \vec{R}_J|} \quad 2.1$$

where summations over  $i$  and  $j$  correspond to electrons and  $I, J$  correspond to nuclei.

The first term is the kinetic energy of the electrons followed by the attractive electron–nuclei interaction, the electron–electron repulsive interaction, the kinetic energy of the nuclei, and the nuclei–nuclei repulsive interaction. The above equation defines  $Z_I$ ,  $m_e$ ,  $M_I$ ,  $\vec{R}_I$  and  $\vec{r}_i$  as charge on nuclei, mass of electrons, mass of nuclei,

position coordinates of nuclei and electrons respectively. The above equation can be written in more compact form as follows

$$\hat{H} = \hat{T}_e(\{\vec{r}_i\}) + \hat{V}_{eN}(\{\vec{r}_i, \vec{R}_I\}) + \hat{V}_{ee}(\vec{r}_i) + \hat{T}_N(\vec{R}_I) + \hat{V}_{NN}(\vec{R}_I) \quad 2.2$$

where the kinetic operator  $\hat{T}$  and potential operator  $\hat{V}$  depend on the position of electron and nuclei,  $\vec{r}$  and  $\vec{R}$  respectively. Also, assuming that the electrons move in the environment of fixed atomic nuclei and denoting the first three terms as  $\hat{H}_e$  yields the electronic part of the Hamiltonian. The total energy  $E_{Tot}$  is obtained by adding the nuclei contribution  $E_N = \hat{T}_N(R) + \hat{V}_{NN}(R)$  to the electronic energy. The minimisation of  $E_{Tot}$  yields the optimised geometry of the nuclei. Many different schemes have been developed to predict from first-principles the electronic structure for many-electron systems. The most advanced methods are based on controlled approximations of the explicit solution of the many-body Schrödinger equation for  $\hat{H}_e$ .<sup>96</sup> However, while these methods are well suited for a limited number of particles interacting with external fields, the enormous number of electrons in solids restricts the applicability of these methods in solid state physics to model systems with many levels of approximations.

A breakthrough in the treatment of the many-body problem was provided by the advancement of density functional theory by Hohenberg and Kohn. They proved that the ground state density uniquely determines the potential and thus all properties of the system, including the many-body wave functions (that is, it reduces the problem of finding the  $3N$  degrees of freedom of an  $N$ -body system to the 3 spatial coordinates of the density). They also showed that the calculation of the ground state energy for the many-body problem can be replaced by the minimization of an energy functional of the density.<sup>96</sup> Later, Kohn and Sham used the latter theorem to derive a tractable set of single-particle equations by replacing the intractable many-body

problem of interacting particles (electrons for the problems tackled in this thesis) in a static external potential with a fictitious system of non-interacting particles that generate the same density as any given system of interacting particles<sup>85</sup> This has made the problem computationally very attractive, thereby establishing DFT as the cornerstone of modern practical numerical methods that describe solids at an *ab initio* level, i.e., without using external parameters.

## 2.2.1 Theoretical foundations of DFT

The conceptual root of DFT can be traced back to Thomas-Fermi-Dirac model. Based on a classical approximation for the electrostatic interaction and the kinetic and exchange energy of the homogeneous electron gas, this model expresses the total energy of a many-electron system in terms of the electron density.<sup>97</sup> However, the fundamentals of DFT were put on a firm basis by the two Hohenberg-Kohn theorems.

The first theorem states that the ground state electronic density determines the external potential  $V_{ext}(\vec{r})$  to within an additive constant. This implies that the ground state electron density uniquely determines the Hamiltonian operator; hence the ground state properties of  $N$  electrons can be found by reducing the  $3N$  spatial coordinates required for the description of the  $N$ -electron wavefunction  $\Psi_0 = (\vec{r}_1, \vec{r}_2, \vec{r}_3 \dots \vec{r}_n)$  to just the 3 spatial coordinates of the density

$$n_0(\vec{r}_1) = \iiint \dots \int \Psi_0 |(\vec{r}_1, \vec{r}_2, \dots, \vec{r}_n)|^2 d\vec{r}_2 d\vec{r}_3 \dots d\vec{r}_n \quad 2.3$$

The second Hohenberg-Kohn theorem states that the ground state energy functional  $E[\rho]$  is minimized by the ground state electron density  $\rho_0$ , that is  $E[\rho_0] \geq E[n_0]$  for every (positive definite) trial electron density. Figure 2.1 demonstrates graphically the Hohenberg-Kohn theorems.

$$\begin{array}{ccc}
V_{ext}(\vec{r}) & \Leftarrow & n_0(\vec{r}) \\
\downarrow & & \uparrow \\
\Psi_i(\{\vec{r}_i\}) & \rightarrow & \Psi_0(\{\vec{r}_i\})
\end{array}$$

**Figure 2.1:** Visualising the implications of the Hohenberg-Kohn theorems <sup>156</sup>. The single arrows indicate the common solution of the Schrödinger equation where the potential determines all the states including the ground state  $\Psi_0(\{\vec{r}_i\})$ . The double arrow denotes the first Hohenberg-Kohn theorem.

The practical application of DFT owes to the work of Kohn and Sham and their independent particle model.<sup>85</sup> They stated that the many-body problem of interacting electrons in a static external potential can be reduced to a problem of non-interacting electrons moving in an effective potential. The Kohn-Sham mapping (visualised in Figure 2.2) of the density and ground state energy of the fictitious system consisting of non-interacting electrons to the real many-body system described by the many-electron Schrödinger equation allows writing independent particle equations as shown below.

$$\left[ -\frac{\hbar^2}{2m} \nabla^2 + V_{KS}[n(\vec{r})] \right] \psi_i(\vec{r}) = \varepsilon_i \psi_i(\vec{r}) \quad \mathbf{2.4}$$

The method introduced by Kohn and Sham is based on the Hohenberg-Kohn theorem that enables the ground state to be found by minimising the functional  $E[n(\vec{r})]$  by varying  $n(\vec{r})$  over all densities containing  $N$  electrons. The Lagrange multiplier  $\mu$  is chosen to introduce this constraint so that

$$\int n(\vec{r}) d\vec{r} = N \quad \mathbf{2.5}$$

and from the minimisation of the energy functional



$$\frac{\delta}{\delta n(\vec{r})} [E[n(\vec{r})] - \mu \int n(\vec{r}) d\vec{r}] = 0 \quad \mathbf{2.6}$$

$$\Rightarrow \frac{\delta E[n(\vec{r})]}{|\delta n(\vec{r})|} = \mu \quad \mathbf{2.7}$$

Kohn and Sham separate  $E[n(\vec{r})]$  into the following parts

$$E[n(\vec{r})] = T_s[n(\vec{r})] + \frac{1}{2} \iint \frac{n(\vec{r})n(\vec{r}')}{|\vec{r}-\vec{r}'|} d\vec{r}d\vec{r}' + E_{xc}[n(\vec{r})] + \int n(\vec{r})V_{ext}(\vec{r})d\vec{r} \quad \mathbf{2.8}$$

where  $T_s[n(\vec{r})]$  is the kinetic energy of the independent particle system with density  $n(\vec{r})$  and is given as

$$T_s[n(\vec{r})] = -\frac{\hbar^2}{2m} \sum_i f_i \int \psi_i^* \nabla^2 \psi_i d\vec{r} \quad \mathbf{2.9}$$

$$\text{and } n(\vec{r}) = \sum_i f_i |\psi_i(\vec{r})|^2 \quad \mathbf{2.10}$$

where  $f_i$  is the occupation of the one-electron wavefunctions.

Substituting Equations 2.9 and 2.8 in 2.7,  $\mu$  can be rewritten in terms of the effective potential  $V_{KS}(\vec{r})$  as

$$\left[ \frac{\delta T_s[n(\vec{r})]}{\delta n(\vec{r})} \right] + V_{KS}(\vec{r}) = \mu \quad \mathbf{2.11}$$

and solves to find the ground state energy  $E_0$ , and density  $n_0(\vec{r})$  in a system containing non-interacting electrons moving in an external potential. All one has to do is to solve the one-electron equation 2.4 self consistently with  $n(\vec{r})$  since from Equation 2.11

$$\left[ -\frac{\hbar^2}{2m} \nabla^2 + V_{KS}[n(\vec{r})] - \varepsilon_i \right] \psi_i(\vec{r}) = 0 \text{ for each } \psi_i(\vec{r}) \quad \mathbf{2.12}$$

$$\Rightarrow \left[ -\frac{\hbar^2}{2m} \nabla^2 + V_{KS}[n(\vec{r})] \right] \psi_i(\vec{r}) = \varepsilon_i \psi_i(\vec{r})$$

Equation 2.4 is called the Kohn-Sham equation and has the form of a Schrödinger equation in which the Kohn-Sham potential  $V_{KS}(\vec{r})$  forms an effective potential for non-interacting particles. From Equations 2.7, 2.8 and 2.11  $V_{KS}(\vec{r})$  includes the external potential and the effect of interactions between the electrons by considering the classical electrostatic (Hartree) potential and an implicit definition of an exchange-correlation potential. The latter derives from the non-classical electrostatic interaction energy and the difference between the kinetic energies of the interacting and non-interacting systems.

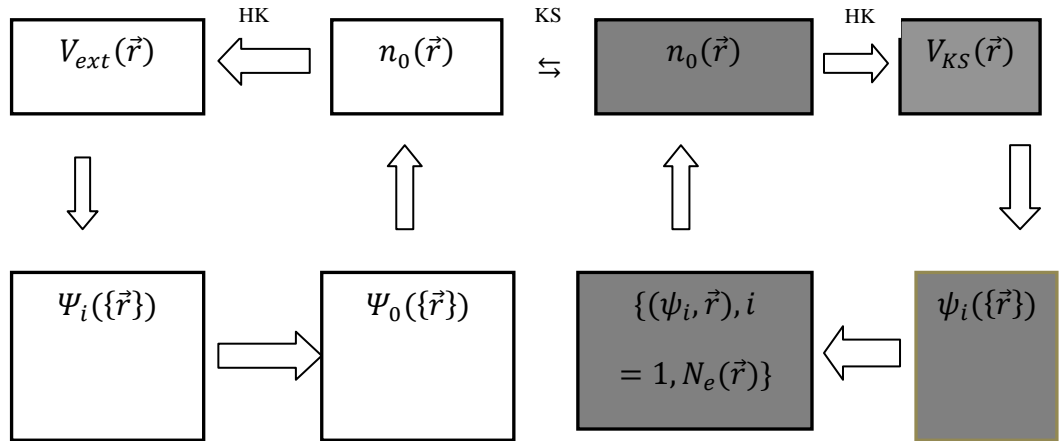


**Figure 2.2:** Visualizing the implications of the Kohn-Sham model. The white left boxes represent the application of the Hohenberg-Kohn theorems (see caption of Figure 2.1). The shaded left boxes (marked with  $HK_0$ ) indicated the application of the theorems to the non-interacting Kohn-Sham system<sup>156</sup> KS indicates the mapping of the many interacting electrons in a static external potential to a problem of non-interacting electrons moving in an effective potential.

The implicit definition of the exchange-correlation potential is given by the functional derivative of the exchange-correlation energy functional

$$V_{xc}(\vec{r}) = \frac{\delta E_{xc}[n]}{\delta n(\vec{r})} \quad \mathbf{2.13}$$

While the exact exchange-correlation energy functional is not known, several approximations exist for its explicit form. The most common approximation assumes that the contribution to the exchange-correlation energy from each infinitesimal volume in space  $d\vec{r}$  is that of a homogeneous electron gas with the same density

$$E_{xc}[n] = \int d\vec{r} \epsilon_{xc}(n(\vec{r}))n(\vec{r}) \quad \mathbf{2.14}$$

where  $\epsilon_{xc}(n(\vec{r}))$  is the exchange-correlation energy per electron in a homogeneous electron gas of density  $n(\vec{r})$ . This is the local density approximation (LDA) in which the exchange-correlation potential  $V_{xc}(\vec{r})$  then takes the form

$$V_{xc}(\vec{r}) = \frac{\delta E_{xc}[n(\vec{r})]}{\delta n(\vec{r})} = \epsilon_{xc}(n(\vec{r})) + n(\vec{r}) \frac{d\epsilon_{xc}(n)}{dn} \Big|_{n=n(\vec{r})} \quad \mathbf{2.15}$$

There are well-known parameterisations for  $\epsilon_{xc}(n(\vec{r}))$ .<sup>98</sup> The LDA applies well if the density variations are small in the length scale of the Fermi wavelength  $\lambda_F$ , namely,  $\frac{|\nabla n(\vec{r})|}{k_F(n(\vec{r}))n(\vec{r})}$ , where  $(2\pi/\lambda_F = k_F = (3\pi n(\vec{r}))^{1/3})$  is the Fermi wavevector. To account for density variations the generalised gradient approximation (GGA) is commonly used in which the exchange-correlation energy functional depends on both the density and its gradient, symbolically

$$E_{xc} = E_{xc}[n(\vec{r}), \nabla n(\vec{r})] \quad \mathbf{2.16}$$

## 2.2.2 Basis sets for solving the Kohn-Sham equations

The Kohn-Sham equations are typically solved numerically on a computer after they are expressed in a specific basis. In performing electronic structure calculations for studies of the ground state and other physical properties there is always a compromise between accuracy and efficiency. One such basic choice involves the selection of the basis set. Plane waves, real-space grids and atom-centred orbitals are most commonly used. Convergence of physical properties with plane waves (PWs) and real-space grids are well controlled by increasing the size of the basis, hence, providing a benchmark for state-of-the-art electronic structure calculations. This is at the expense of computational time and memory requirements.<sup>99,100</sup> On the other hand, basis sets made of atomic orbitals (AOs) can be much smaller; for comparison, a dozen of AOs is required per atom instead of hundreds of PWs per atom for a similar quality calculation.<sup>86,87</sup> In addition, the localisation of AOs has motivated their development for large-scale *order-N* calculations<sup>99,101,102</sup> and simulations of

charge-carrier transport.<sup>76,94,95</sup> However systematic improvements of AOs for quantitative predictions are more challenging.<sup>103</sup>

Atomic orbitals are routinely employed in calculations of atomic and molecular spectra since it is a reasonable starting point. Their convergence properties have been intensively studied in quantum chemistry for decades.<sup>103,104</sup> Implementations also exist for extended solid-state systems<sup>102,105-109</sup> but by comparison the use of AOs is less established. The transferability of tabulated AOs in different chemical environments is an old problem which the construction of *numerical* atomic orbitals (NAOs) promises to remedy,<sup>92,102,110</sup> in particular under various schemes of on-the-fly optimisation.<sup>107,111</sup> After a brief introduction to PWs a scheme of generating NAOs is explained below.

### 2.2.2.1 Plane wave basis sets

Traditionally plane waves have been used in electronic structure calculations of solids where the underlying lattice provides periodicity to the Kohn-Sham wave function. To use these implementations in more general cases where periodicity does not apply (or exists only in certain directions), a repeating unit (supercell) can be set up with sufficient vacuum to make the interaction between repeated atoms, molecules or finite clusters negligible. In any case, the Kohn-Sham wave function  $\Psi_i$  can be expanded in plane waves

$$\Psi_i(\vec{r}) = \sum_{\vec{G} < \vec{G}_{max}} C_{i,\vec{G}} \cdot e^{i(\vec{K}+\vec{G})\vec{r}} \quad \mathbf{2.17}$$

Where  $\vec{K}$  and  $\vec{G}$  are plane waves and reciprocal lattice vector that satisfies the periodicity imposed to the supercell. Systematic convergence can be achieved by increasing the number of plane waves, that is, increasing  $\vec{G}_{max}$ . To allow for that,

one sets a single variational parameter, that is, the maximum kinetic energy  $E_{cutoff} = \frac{\hbar^2}{2m} |G_{max}|^2$  of the plane waves. However, converged sets of plane waves are computational demanding. On the other hand, numerical atomic orbitals (NAOs) can be computationally very efficient but more approximate. A handful of NAOs are required per atoms compared to the hundreds of plane waves.

### 2.2.2.2 Numerical atomic orbitals basis sets

Herein, the scheme to generate numerical atomic orbitals as developed by Ozaki<sup>92 156</sup> has been described. Other proposals follow the same spirit. The method builds on expressing the Kohn-Sham wavefunction  $\psi_i$  as a linear combination of atomic-like basis functions  $\varphi_\mu$  located at the various atomic sites

$$\Psi_i(\vec{r}) = \sum_n \sum_{\mu=1}^K C_{i\mu} \varphi_\mu(\vec{r} - \vec{r}_n) \quad ; \{ \varphi_\mu; \mu=1, 2 \dots K \} \quad \mathbf{2.18}$$

where  $n$  is the site index and  $\mu$  includes the angular momentum  $l$ , magnetic quantum number  $m$  and the multiplicity index  $p$ , namely,  $\mu \rightarrow p, l, m$ . The  $\{\varphi_\mu\}$  basis is obtained by the eigenvectors of the Schrödinger equation for an atom in a slightly modified environment that accounts to some extent for the orbital relaxation when bonding. A confinement barrier added to the atomic potential at a radius  $r_c$ , beyond which the wavefunction vanishes, defines the pseudoatom. The obtained pseudoatomic wavefunctions are referred as primitives, e.g., the notation Smpm'dm" indicates that  $m$ ,  $m'$  and  $m''$  such functions are used to expand  $s$ ,  $p$ , and  $d$  orbitals, respectively. Their properties have been studied in detail for a range of atoms.<sup>92</sup> In analogy to Quantum Chemistry, basis sets are denoted as single-zeta, double-zeta and so on, depending on the number of primitives per valence state.

In spite of their success in describing structural and electronic properties, NAOs require more inbuilt flexibility for optimal numerical efficiency and accuracy.<sup>90,92,112,114</sup> This implies introducing an additional degree of freedom and can be achieved by further expressing the NAOs  $\{\varphi_\mu\}$  as a linear combination of pseudoatomic orbitals with the same  $(l,m)$  index pair, namely,

$$\varphi_\mu(\vec{r}) = \sum_q \alpha_{\mu q} \chi_\eta(\vec{r}) \quad \mathbf{2.19}$$

with  $\eta \rightarrow q, l, m$  and  $\mu \rightarrow p, l, m$ . This leads to contracted or optimised numerical atomic orbitals similar to the Gaussian contractions.<sup>103</sup> The notation `snmpn'm'dn` is used to indicate abbreviation of basis sets, e.g., `s32p32d1` means that two optimised orbitals are constructed from three primitive functions to describe s and p electrons respectively, while one primitive is employed for the d orbitals.

The above scheme of contracted numerical atomic orbitals expresses the functions of the  $\{\varphi_\mu\}$  basis as a functional of the primitive orbitals  $\chi_\eta$  allowing for their optimisation in a given chemical environment. In addition to the expected better accuracy there are other benefits to this approach. First, instead of increasing the number of primitives and their angular momentum to achieve convergence, a much smaller basis set can be used that yields results of similar quality. This is demonstrated in the next Chapter. Orbital optimisation does not only decrease the computational cost by reducing the size of the basis. It makes also highly likely to avoid the issue of basis sets overcompleteness. However, there are associated drawbacks as the optimised contractions for a chemical environment are not *a priori* known. Despite the development of optimisation schemes<sup>92,103,110,112</sup> the computational overhead leads to very often adopting in practice atomic basis sets (pre-)optimised for generic environments.<sup>92,111</sup> In either case, that is, of pre-

optimised or fully optimised orbitals, their make-up and transferability still needs to be established for the system at hand. This is discussed in Chapters 3 and 4 for the case of SiNWs with different surface terminations and dopant impurities.

## 2.3 Quantum theory of transport

Different levels of theories and within varying degrees of approximation have been applied to study the electronic transport in solids starting from classical drift-diffusion equations and the semi-classical Boltzmann transport method to Kubo's formalism and the explicit solution of the Schrödinger equation. In the meso- and nano- scale of materials and as devices scale down, the Fermi wavelength  $\lambda_F$  of charge carriers (1 Å in highly conductive metals to tens of nm in low-dimensional semiconductors) becomes comparable to other characteristic length scales defined by geometric and materials features. It is therefore essential to account for the quantum mechanical nature of charge carriers in order to get reliable predictions about transport properties of materials and electrical device characteristics.

Two methods have been most commonly used for studying quantum transport. These are the Landauer scattering matrix approach<sup>114</sup> and the non-equilibrium Green's function technique (NEGF).<sup>155</sup> The Landauer approach has been considered very successful due to its simplicity in explaining conductance quantisation and other mesoscopic interference effects in low-dimensional systems.<sup>114</sup> It is mostly applied in studies of coherent charge transport, that is, it does not take into account inelastic processes (for example from electron-phonon and electron-electron interactions). There have been generalisations to include these effects but based on perturbation techniques the NEGF framework offers a solid foundation to extend its applicability beyond coherent transport.<sup>156</sup> NEGF also readily accounts for self-consistency of the potentials induced by non-equilibrium charges when external bias is applied. In this



thesis, the Landauer approach was applied to calculate the effect of scattering from impurities in silicon nanowires (Chapters 4, 5 and 6). In Chapter 6, such calculations of the mean free path are combined with a semi-classical approach to derive the mobility dependence on nanowire diameter and dopant position. The NEGF method is applied in Chapter 5 to study the interplay between basis set dependence and charge self-consistency.

### 2.3.1 Landauer formalism

The Landauer formalism relates the current across a nanostructure with the transmission of charge carriers through the material channel in terms of scattering theory. Sometimes it is referred to as describing ballistic transport since it does not take into account inelastic processes such as electron-phonon or electron-electron interaction beyond an effective mean-field potential. This implies that it is applicable when the corresponding mean free path of inelastic processes is much larger than the device dimensions. Nevertheless, the Landauer formalism can always be used to extract physical information about scattering of charge carriers with impurities as well as surface and interface boundaries, allowing for size-quantisation, quantum confinement, quantum interference and quantum diffusion.

Let us consider a central channel region  $L$  of a wire with finite cross-section contacted by two leads which act as ideal reservoirs. For simplicity, we assume that the leads are identical and that they are ideal (uniform along the current direction). The chemical potential of the left and right reservoirs are denoted by  $\mu_L$  and  $\mu_R$  respectively. A typical setup is shown in Figure 2.3.

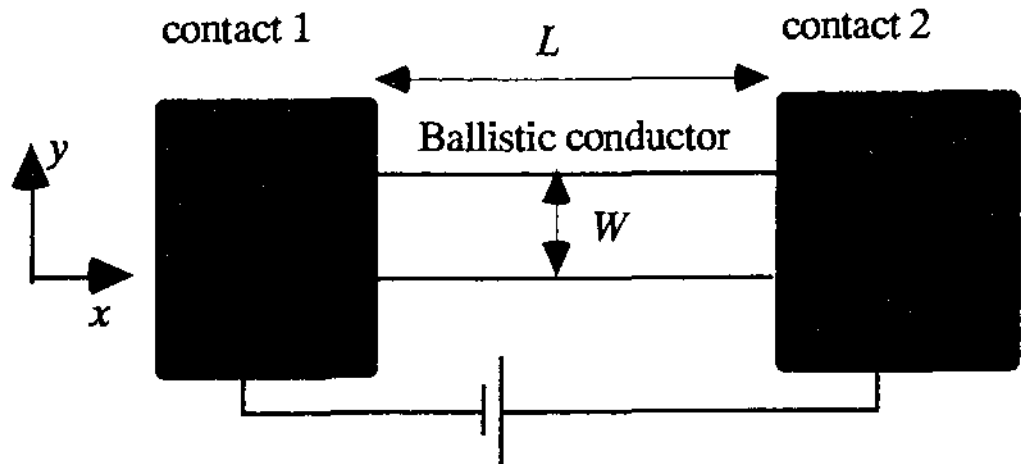


**Figure 2.3:** A ballistic conductor is sandwiched between two contacts across which an external bias is applied. Electrons can flow into conductor from the contacts without any reflection, that is, the contacts are assumed to be ideal or reflectionless. When a source-drain bias voltage is applied the conducting channel region  $L$  remains in a non-equilibrium state as it tries to equilibrate with each of the two chemical potentials of the reservoirs. The left reservoir pushes electrons in the channel while the right reservoir draws away electrons, thus the channel region remains in a balancing act between the source and drain. The difference in chemical potentials gives rise to two different quasi-Fermi levels at the interface with the source and drain. The imbalance in the occupancy of electrons is responsible for electron flow across the material channel.

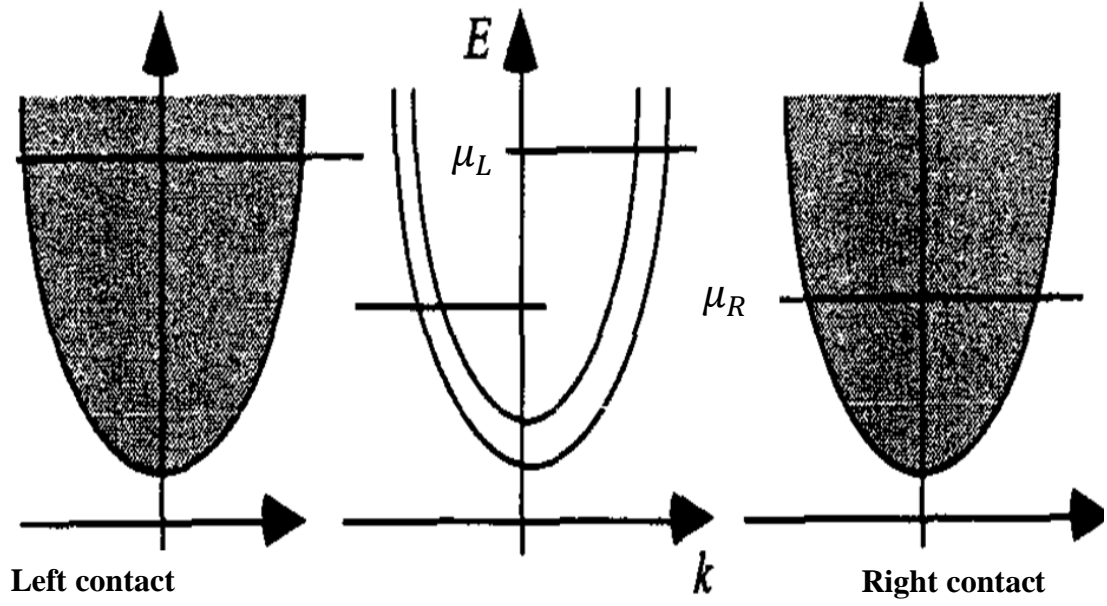


**Figure 2.4:** Occupancy of electrons occurring after applying bias  $V$  in a ballistic conductor. The variation in the electrochemical potential has been shown by  $\mu_L > \mu_R$  for flow of electrons from left to right contacts.

The quantum mechanical solution of the Schrödinger equation in the periodic leads yields propagating plane waves along the wire axis. These are so-called channel eigenstates or modes which for the  $n^{\text{th}}$ -subband can be expressed as

$$\psi_n(x, y, z) = \frac{1}{\sqrt{L}} e^{ik_x^p x} \phi_n(y, z) = X_n(x) \phi_n(y, z) \quad 2.20$$

Assuming simple one-dimensional parabolic sub-bands, the occupancy of electrons occurring after applying bias  $V$  is shown in Figure 2.4. Prior to Eq. 2.20  $x$  should be defined as the transport direction,  $y, z$  as perpendicular. Electrons originating from the left lead occupy the  $+k_x$  states having positive group velocity in the  $x$  direction and their occupation probability is given by the Fermi-Dirac distribution  $f^L(E)$ . The states with negative group velocity ( $-k_x$ ) are occupied by electrons originating from the right lead and are occupied according to the distribution  $f^R(E)$ . Given the

electron density of single transverse mode occupying  $+k_x$  states is  $\frac{1}{L}$  where  $L$  is the length of the conductor, the current carried by the  $+k_x$  states is given by

$$I_{L \rightarrow R}^+ = -\frac{1}{L} \sum_{k_x > 0} e v_x(k_x) f^L(E_{k_x}) \quad \mathbf{2.21}$$

**or**

$$I_{L \rightarrow R}^+ = -\frac{e}{L} \sum_{k_x} \frac{1}{\hbar} \frac{\partial E}{\partial k_x} f^L(E_{k_x}) \quad \mathbf{2.22}$$

$$\text{where } v_x = \frac{1}{\hbar} \frac{dE}{dk_x}$$

An incident flux of charge carriers from the left lead would scatter at the scattering region and out flux would transmit into the right lead or reflect back at the left. The total current can be obtained by taking into account the probability of electrons to cross the channel along with summation of all subbands, that is, the transmittance. Thus, after considering also the spin of the electron, the total current flowing from the left to right reservoir is given as

$$I_{L \rightarrow R}^+ = -2(\text{for spin}) \frac{e}{L} \sum_{n=1}^N \sum_{k_x^n > 0} v_x^n(k_x^n) T_n(E) f^L(E) \quad \mathbf{2.23}$$

$$= -2 \frac{e}{L} \sum_n \frac{1}{2\pi} \int_{-\infty}^{+\infty} dk_x v_x^n(k_x^n) T_n(E) f^L(E) \quad \mathbf{2.24}$$

$$I_{L \rightarrow R}^+ = -\frac{2e}{h} \int_{-\infty}^{+\infty} dE T(E) f^L(E) \quad \mathbf{2.25}$$

$$\text{Where } T \equiv \sum_n T_n \quad \mathbf{2.26}$$

Similarly the current flow from right to left reservoir is given by

$$I_{R \rightarrow L}^- = -\frac{2e}{h} \int_{-\infty}^{+\infty} dE T(E) f^R(E) \quad \mathbf{2.27}$$

The net current is obtained by subtracting  $I_{R \rightarrow L}^-$  from  $I_{L \rightarrow R}^+$

$$I_{L \rightarrow R}^+ - I_{R \rightarrow L}^- = -\frac{2e}{h} \int_{-\infty}^{+\infty} dE T(E) [f^L(E) - f^R(E)] \quad \mathbf{2.28}$$

$$I = -\frac{2e}{h} \int_{-\infty}^{+\infty} dE T(E, V) [f^L - f^R] \quad \mathbf{2.29}$$

In the last expression the dependence of the distribution function on the chemical potential and the electronic temperature  $T_e$  is restored as well as the dependence of the transmittance to the applied potential (if the calculation is performed self-consistently).

However, at low-bias (linear response)

$$\mu_L - \mu_R = eV \rightarrow 0 \quad \mathbf{2.30}$$

the difference in the Fermi-Dirac distributions can be expressed as

$$f^L - f^R \approx \frac{\partial f_0(E - E_F; T_e)}{\partial E_F} (-eV) = \frac{\partial f_0(E - E_F; T_e)}{\partial E} (eV) \quad \mathbf{2.31}$$

thereby yielding

$$I = -\frac{2e^2}{h} V \int_{-\infty}^{+\infty} dE T(E) \frac{\partial f_0(E - E_F; T_e)}{\partial E_F} \quad \mathbf{2.32}$$

after substitution to Equation **2.33**. This implies the definition of the conductance at linear response as

$$G_C = \frac{I}{(\mu_L - \mu_R)/e} = \frac{I}{V} \quad \mathbf{2.33}$$

$$G_C(T_e) = -\frac{2e^2}{h} \int_{-\infty}^{+\infty} dE T(E) \frac{\partial f_0(E - E_F; T_e)}{\partial E_F} \quad \mathbf{2.34}$$

At zero temperature  $\frac{\partial f_0(E - E_F; T_e)}{\partial E_F} = \delta(E - E_F)$ , hence Equation **2.35** yields

$$G_C(T_e \rightarrow 0) = \frac{2e^2}{h} T(E_F) \quad 2.36$$

$$G_C(T_e \rightarrow 0) = \frac{2e^2}{h} \sum_{n=1}^{N_{chan}} T_n(E_F) \quad 2.37$$

The above expression is the celebrated Landauer formula which relates the conductance with transmission. Evidently, the conductance depends on the number of transverse modes of the channel  $N_{chan}$ . If the conductor is much smaller than any scattering length  $L_m$  ( $L \ll L_m$ ) then  $T_n \approx 1$  for all subbands and  $G_C = \frac{2e^2}{h} N_{chan}$ .

This manifests that the conductance is quantised and is proportional to the number of propagating modes.  $G_0 = \frac{2e^2}{h} = 77.48 \mu S$  is the quantum of conductance. The resistance  $R_C (= G_C^{-1})$  defines the contact resistance which arises due to the interface between the reservoirs and the conductor. This is unlike a macroscopic conductor which follows Ohms law  $R_C = \frac{\rho L}{A}$ . Here,  $\rho$  and  $A$  are the resistivity and cross-sectional area of the wire, respectively. As  $N$  is directly proportional to  $A$  the quantum resistance also decreases with increasing cross-section as more subbands are populated but in discrete steps.

### 2.3.2 S-matrix

It is apparent that the central quantity in the Landauer approach is the probability for charge carriers to be transmitted through the scattering region. To this end, it is instructive to sketch how this probability is calculated. Quite generally the problem can be expressed through the quantum mechanical scattering matrix or S-matrix. The S-matrix relates the amplitude of outgoing channel eigenstates to the amplitudes of incoming modes via transmission ( $\hat{t}$ ) and reflection matrices ( $\hat{r}$ ) for each lead

$$\begin{pmatrix} OUT_R \\ OUT_L \end{pmatrix} = \hat{S} \begin{pmatrix} IN_R \\ IN_L \end{pmatrix} \quad \mathbf{2.38}$$

$$where \hat{S} = \begin{bmatrix} \hat{r} & \hat{t}' \\ \hat{t} & \hat{r}' \end{bmatrix} \quad \mathbf{2.39}$$

The dimension of the S-matrix is determined by the number of channels in each lead. For example,  $\hat{r}$  and  $\hat{t}$  are  $N_{chan}^R \times N_{chan}^R$  and  $N_{chan}^L \times N_{chan}^R$  matrices, where  $N_{chan}^R$  and  $N_{chan}^L$  are the number of channels in the right and left lead respectively. And  $\hat{r}'$  and  $\hat{t}'$  defines the reflection and transmission of electrons respectively from right lead. The transmission probability of each mode is obtained by taking the square of the corresponding S-matrix element

$$T_n = T_{L \leftarrow R} = |S_{L \leftarrow R}|^2 \quad \mathbf{2.40}$$

The total transmission probability (transmittance or transmission function) can be obtained from the summation of the transmission probability of each mode

$$T(E) = \sum T_{L \leftarrow R} \quad \mathbf{2.41}$$

To calculate the S-matrix, response Green's functions are employed since they contain information for a response at point  $r'$  due to an excitation at point  $r$ . It is generally impossible to calculate the Green's function for the whole system. However, one may calculate the Green's function for a region that contains the scatterer and connects the left to the right lead. The first step is to divide the system into three parts as before (*left lead + conducting channel/scatterer + right lead*).

The total Hamiltonian can be expressed symbolically as

$$\hat{H} = \hat{H}_L + \hat{H}_C + \hat{H}_R + \hat{H}_{LC} + \hat{H}_{CR} \quad \mathbf{2.42}$$

where L(R) and C stand for the left(right) lead and the conductor in the centre. Let us consider the representation for basis functions as  $\varphi_L$ ,  $\varphi_C$  and  $\varphi_R$  for the left, centre and right regions respectively; in this thesis  $\hat{H}$  is the Kohn-Sham Hamiltonian and the basis functions are numerical atomic orbitals. Then, the Hamiltonian can be expressed in the following matrix form under the assumption that there is no interaction between the left and right leads

$$H = \begin{pmatrix} H_L & H_{LC} & 0 \\ H_{LC} & H_C & H_{RC}^\dagger \\ 0 & H_{RC} & H_R \end{pmatrix} \quad \mathbf{2.43}$$

For non-orthogonal orbitals there is also the corresponding overlap matrix

$$S = \begin{pmatrix} S_L & S_{LC} & 0 \\ S_{LC}^\dagger & S_C & S_{RC}^\dagger \\ 0 & S_{RC} & S_R \end{pmatrix} \quad \mathbf{2.44}$$

Here,  $H_L(S_L)$ ,  $H_R(S_R)$  and  $H_C(S_C)$  are the Hamiltonian (overlap) matrices of the leads and the device and  $H_{LC}(S_{LC})$ ,  $H_{RC}(S_{RC})$  are the coupling matrices between the device region and the leads.

The Green's function for the semi infinite leads is expressed as (here, it is assumed that  $E \equiv E + i0^+$ , thereby defining the retarded Green's function)

$$g_{L(R)}^r(E) = (ES_{L(R)} - H_{L(R)})^{-1} \quad \mathbf{2.45}$$

Defining the self-energies  $\Sigma_L^r$ ,  $\Sigma_R^r$  via

$$\Sigma_L^r(E) = (ES_{LC} - H_{LC})^\dagger g_L^r(E) (ES_{LC} - H_{LC}) \quad \mathbf{2.46}$$

$$\Sigma_R^r(E) = (ES_{RC} - H_{RC})^\dagger g_R^r(E) (ES_{RC} - H_{RC}) \quad \mathbf{2.47}$$



one can solve for the Green's function of the central region

$$g_C^r(E) = [ES_C - H_C - \Sigma_R^r(E) - \Sigma_L^r(E)]^{-1} \quad \mathbf{2.48}$$

where the effect of the leads on to the conductor is taken into account via the self-energies. Finally, the scattering matrix can be calculated using the channel eigenstates and  $g_C^r(E)$ .<sup>155</sup> For example, the transmission function is expressed in terms of Green's function as

$$T(E) = \text{Tr}[g_C^r(E)\Gamma_L(E)g_C^r(E)^\dagger\Gamma_R(E)] \quad \mathbf{2.49}$$

where  $\Gamma_{L(R)}(E) = i[\Sigma_{L(R)}^r(E) - \Sigma_{L(R)}^r(E)^\dagger]$ . The unitarity of the S-matrix can be checked ( $\hat{S}\hat{S}^\dagger = 1$ ) since probability is conserved for each channel.

### 2.3.3 Self-consistency using NEGF

As mentioned in the previous sections we use the Kohn-Sham Hamiltonian  $H_{KS}$  as input to my transport calculations. Following Ke *et al.*<sup>115</sup> the NEGF can be performed independently of the electronic structure step. Solution of the Green's function  $g_C^r(E)$  from  $H_{KS}$  is equivalent to solving the KS equations, so  $g_C^r(E)$  contains information on the state of the system.<sup>155</sup> For an initial Hamiltonian and the corresponding Green's function, the density matrix (DM) is calculated according to

$$\begin{aligned} DM = & -\frac{1}{\pi} \int_{-\infty}^{+\infty} dE \, \text{Im}[(g_C^r(E) f^L(E - \mu_L; T_e))] + \\ & \frac{1}{2\pi} \int_{-\infty}^{+\infty} dE [g_C^r(E)\Gamma_R(E)g_C^r(E)^\dagger][f^R(E - \mu_R; T_e) - f^L(E - \mu_L; T_e)] \end{aligned} \quad \mathbf{2.50}$$

Unlike electronic structure calculations which are typically carried out with periodic or cluster boundary conditions (BCs), the above equation yields the DM for the *open* system, with self-energies taking into account the semi-infinite electrodes. The first term in Equation 2.50 is the equilibrium (linear-response) contribution to the DM, and the second term is the non-equilibrium (polarization and current flow) contribution, which vanishes when  $\mu_L = \mu_R$ .

The charge density can be computed straightforwardly from the DM according to

$$\rho(r) = \sum_{\mu,v} \varphi_{\mu}^*(r) \text{Re}[(DM)_{\mu,v}] \varphi_v(r) \quad 2.51$$

As a general principle, codes based on KS-DFT can find the entire system Hamiltonian  $H_{KS}$  from knowledge of just the electronic density, so this density is used in the electronic structure code to extract the new Hamiltonian matrix of the device region. This process of computing the density matrix from the Hamiltonian and vice versa iterates until the charge density converges, after which the S-matrix and the transmission function  $T(E)$  are computed for the converged density.

## 2.4 Computational packages

Below a brief description follows of the computational tools used in the calculations.

### 2.4.1 Quantum Espresso

Quantum Espresso is an open source integrated suite of computer codes for geometrical optimisations of the atomic structure and electronic structure calculations.<sup>116</sup> It is based on a plane wave implementation of DFT. Pseudopotentials (both norm-conserving and ultra soft) are employed to eliminate core states. Quantum Espresso builds onto newly-restructured electronic-structure codes (PWscf, PHONON, CP90, FPMD, and Wannier) that have been developed and tested by

some of the original authors of novel electronic structure algorithms - from Car-Parrinello molecular dynamics to density-functional perturbation theory - and applied in the last twenty years by some of the leading materials modelling groups worldwide. Quantum Espresso can perform the following types of calculations:

- 1) Geometrical optimisation
- 2) Band structure, projected density of states
- 3) Electron-phonon interactions

The most important input parameters in Quantum Espresso are the atomic geometries (number and types of atoms in the periodic cell, bravais-lattice index, crystallographic or lattice constants), the kinetic energy cutoff, the type of pseudopotentials, and the total maximum force on an individual atom for geometry optimizations.

Quantum Espresso is a very simple approach towards predicting the electronic properties of materials or a combined system. As Quantum Espresso uses plane wave basis sets it is one of the most accurate DFT tools. However, it has limited capability when applied in large systems due to the computational cost.

### **2.5.2 OpenMX**

OpenMX (Open source package for Material eXplorer) is a software package for nano-scale material simulations based on DFT.<sup>156</sup> Unlike Quantum Espresso OpenMX solves the Kohn-Sham equations using pseudo-atomic localized basis functions (NAOs with a finite radius) which is useful for  $O(N)$  calculations. Open-MX uses the local density approximation (LDA and local spin density approximation) and generalized gradient approximation to the exchange-correlation potential with norm-

conserving pseudopotentials. It requires similar inputs to Quantum Espresso with the main difference arising from the use of the NAOs as described in Section 2.2.2.2.

Open-MX calculates many structural and electronic properties such as total energy, forces, band structure, density of states (DOS) and projected DOS, and can perform full and constrained geometry optimisation. Since the code is designed for the realization of large-scale ab initio calculations on parallel computers, it is anticipated that OpenMX can be a useful and powerful tool for nano-scale material sciences in a wide variety of systems such as bio-materials, carbon nanotubes, magnetic materials, and nanoscale conductors.

### 2.5.3 TiMeS

TiMeS (Transport in Mesosopic Systems) is an in-house modular transport simulator that allows measurement of both the intrinsic electronic transport properties of materials and the electrical characteristics of devices. Based on Green's function techniques, the scattering-matrix, and hence the transmission  $T(E)$  of charge carriers injected at energy  $E$ , can be calculated from a single-particle Hamiltonian  $H$  in either the low-bias (non-self-consistent) Landauer approximation or in fully self-consistent NEGF theory.

The non-self-consistent (NSC) version of TiMeS operates as a post-processing step after the electronic structure computation. Importantly, TiMeS is completely modular in that it needs, and has, no information about the representation used by the electronic structure code *except* for the single-particle (typically Kohn-Sham) Hamiltonian and overlap matrices. TiMeS currently has interfaces to accept this information from OpenMX,<sup>92</sup> DFTB<sup>+117</sup> and the Quantum Espresso DFT code *via* transformation of plane waves to Wannier orbitals.<sup>118</sup>

Like other localized-orbital electronic transport codes based on Landauer or NEGF theory,<sup>119,120</sup> TiMeS calculates the self-energy of the semi-infinite electrodes based on the surface Green's function for the given on-site and hopping Hamiltonian and overlap matrices for the electrodes. The entire transport region is broken into three sub-regions: the two electrodes and a scattering region.<sup>115</sup> The electrodes are semi-infinite repetitions of periodic cells. These cells and the scattering region must be “principal layers”<sup>115</sup> such that overlap elements vanish for orbitals separated beyond the adjacent principal layers. Therefore, just one hopping Hamiltonian is needed for each electrode. TiMeS then proceeds to solve the scattering problem as described in Section 2.3.1.

Starting with this low-bias algorithm, TiMeS is extended to perform fully self-consistent NEGF calculations to retain modularity. NEGF is implemented independently of the electronic structure step and TiMeS calculates the electronic density matrix from the (typically KS-DFT) Hamiltonian output by the electronic structure code. The procedure to obtain the converged density matrix using open boundary conditions (BCs) was explained in Section 2.3.2. The integration in Equation.2.50 is done by Gaussian quadrature, and the equilibrium part may also use complex contour integration (starting appreciably below the lowest energy band), such that each integral usually requires evaluation of  $G(E)$  at  $\sim 50$  or fewer energies  $E$ . Note that even in a zero-bias calculation, the linear-response density in NEGF can differ from the non-self-consistent result because of the inclusion of the self-energies representing open BCs rather than the periodic BCs of the electronic structure step. In the limit of an ideal calculation, the central region should be made long enough that the BCs are virtually irrelevant, but this is not always the case in practice. In the case of applied bias, convergence is ensured by extending the scattering region.

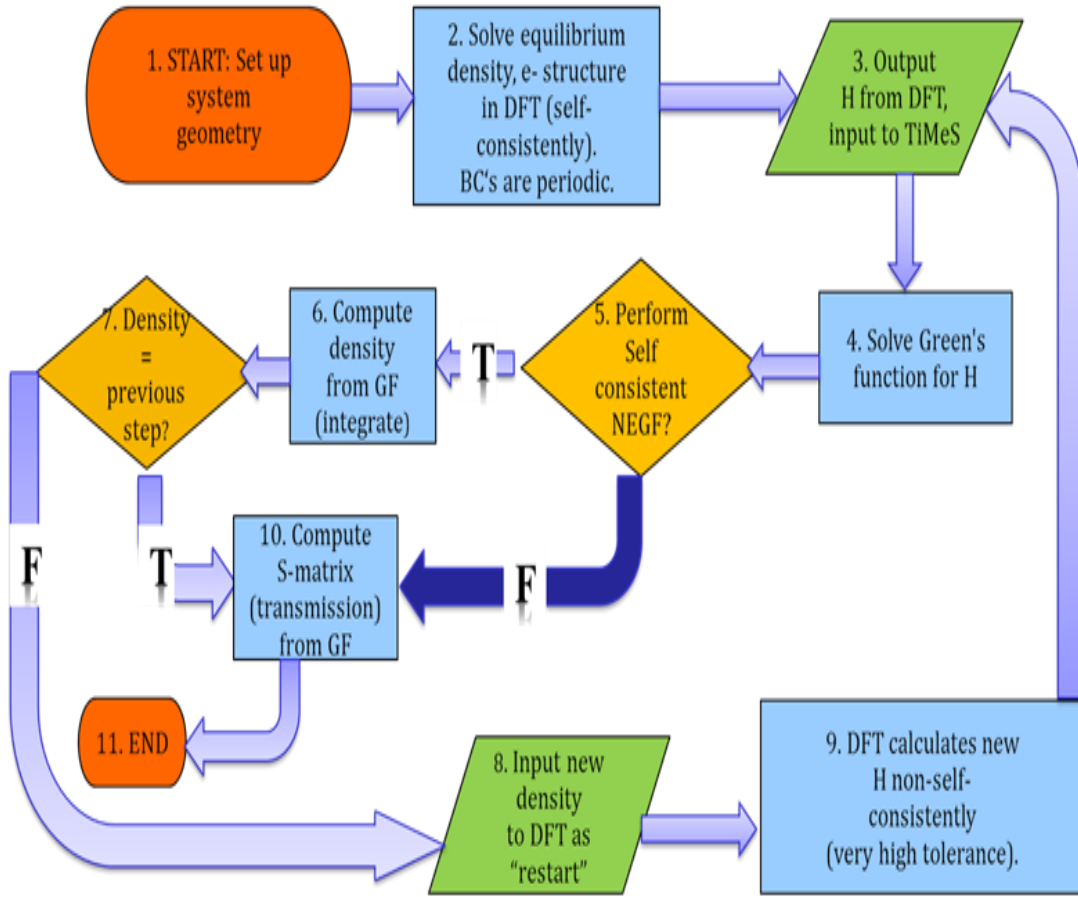


**Figure 2.5:** The TiMeS flowchart shows the cross-platform of quantum transport implementation. The non-self-consistent step is indicated by the dark (blue on line) arrow.

The non-self-consistent and the NEGF flowchart are shown in Figure 2.5. This flexibility and modularity allows for easy continuation of interrupted runs, as well as interchange and comparison of different electronic structure approaches or density functionals. The programme flow is specifically designed to allow a modular incorporation of differing electronic structure methods to obtain the single-particle Hamiltonian. In the present work, matrix representations of the Hamiltonians of the relaxed structures were obtained from OpenMX.

## Chapter 3: Structural and electronic properties of hydrogenated and hydroxylated SiNWs

### 3.1 Chapter introduction

The properties of silicon nanowires have been previously explored using DFT with plane wave<sup>69,112,121</sup> and atomic basis sets.<sup>92,110</sup> Other approximate methods such as empirical tight-binding<sup>76,83,117</sup> and DFT within the approximate Harris-Foulkes functional<sup>76</sup> have also been used. Most studies identified the qualitative dependence of the band gap magnitude and character as a function of nanowire diameter, orientation axis, cross-section shape and surface preparation. It is generally found that the band gap in silicon nanowires becomes direct due to zone folding and increases with decreasing diameter due to size-quantisation.<sup>65</sup> For a fixed cross-section, hydrogen passivated SiNWs grown along the orientations  $\langle 111 \rangle$ ,  $\langle 110 \rangle$ , and  $\langle 100 \rangle$  show larger band gap in the given order<sup>58</sup> whereas surface termination with species other than hydrogen tends to decrease the band gap.<sup>65</sup>

In this Chapter, the issue of quantitative estimates in SiNWs derived from DFT implementations using numerical atomic orbitals (NAOs) is revisited. It is the purpose of this chapter to examine the method proposed by Ozaki et al.<sup>92, 111</sup>, and implemented in the OpenMX package<sup>156</sup> and take a first step towards a systematic validation of its accuracy for electronic structure calculations (and derived quantities) in SiNWs. Early studies in bulk-Si<sup>105</sup> have indicated that a double-zeta polarised (DZP) basis set may suffice and variational freedom from larger basis sets may be required for converged forces in atomic relaxations.<sup>124</sup> This rule of thumb is not always followed in SiNW calculations, specifically in asserting qualitative

trends, and more importantly there is no point of reference. Here, the systematic improvement of electronic structure calculations in SiNWs with respect to the basis size and optimisation has been studied.

By using the basis sets provided by the OpenMX library and varying the number of functions their quality was established their quality before and after orbital optimisation, in calculating properties such as total energies, band gaps, effective masses and group velocities. The latter are important to estimate the charge-carrier mobility in SiNWs. Results are benchmarked against the PW implementation in the Quantum Espresso electronic structure platform.<sup>118</sup> The addition of d-polarisation functions is a minimum requirement to obtain the correct bonding geometries and qualitative description of the electronic structure. It was found that a DZP basis with orbital optimisation provides a good compromise between efficiency and accuracy yielding overall significant improvement at a small cost. Most importantly, the optimised orbitals are transferable to different wire orientations and surface terminations. These conclusions should be applicable to other semiconductor nanostructures. Notably, bond lengths, atomisation energies, and Kohn-Sham eigenvalue spectra were compared previously between PW and OpenMX NAOs basis sets for dimers and it was found that chemical accuracy can be obtained even with a small set of orbitals.<sup>114</sup>

The structure of the chapter is as follows. For benchmarking of NAOs with PWs, in Section 3.2 we consider two systems of common interest (see Figure 3.1): (a) intrinsic hydrogen-passivated SiNWs (SiNW:H) and (b) intrinsic SiNWs with hydroxyl surface termination (SiNW:OH) as a minimal model of an oxidised surface. A more detailed analysis of band structure properties is given in Section 3.3 for the



common case of hydrogenated SiNWs followed by a discussion of transferability in Section 3.4.

## 3.2 Benchmarking of numerical atomic orbitals

### 3.2.1 Hydrogenated silicon nanowires

Hydrogenated SiNW grown along the  $\langle 110 \rangle$  crystallographic direction with diameter 1.15 nm (24 Si and 16 H atoms in the unit cell) were constructed by cutting a hexagonal cross-section from the bulk-Si structure and passivating the free surfaces with hydrogen. These structures are considered as prototype models due to their common occurrence using bottom-up synthesis. The DFT methodology has been discussed in Section 2.3.

First, the electronic structure has been calculated using plane wave basis sets as implemented in the Quantum Espresso (QE) package. This sets the benchmark with respect to results obtained from NAO basis sets. The structure was geometry optimised with force threshold of  $0.01 \text{ eV/\AA}$  and Monkhorst-Pack k-point sampling on a  $15 \times 1 \times 1$  grid in the Brillouin zone. The PW kinetic energy cut-off was chosen to be 30 Ry (408.17 eV). The PBE generalised gradient functional (GGA) and norm-conserving pseudopotentials have been used throughout the simulations. The cross-section of the relaxed SiNW:H is shown in Figure 3.1(a). The Si-Si bond distance is  $2.362 \text{ \AA}$  at the core and  $2.351 \text{ \AA}$  at the surface. These are in good agreement with previous PW calculations obtained from the VASP programme package<sup>125</sup> by using the same functional and projector augmented wave (PAW) method with an [Ar] core for Si. Similarly, the predicted Si-H bond length in the relaxed geometry is  $1.5 \text{ \AA}$  which is the same as the experimental value.<sup>22</sup>

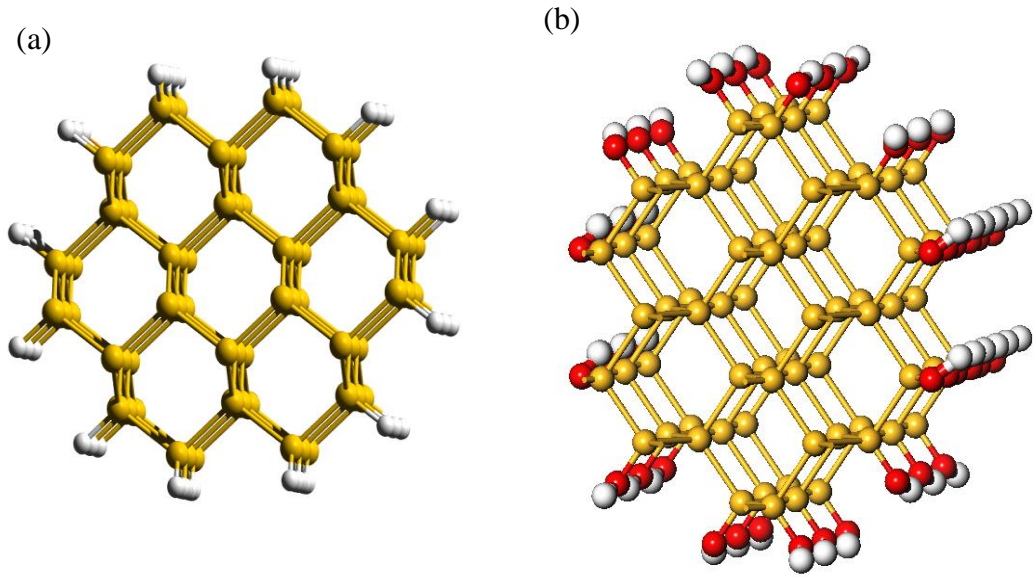


**Figure 3.1:** Three dimensional cross-sectional views of nanowires oriented along the  $\langle 110 \rangle$ -crystallographic direction as studied here; (a) intrinsic hydrogen-passivated SiNWs (SiNW:H) and (b) intrinsic SiNWs with hydroxyl surface termination (SiNW:OH) as a minimal model of an oxidised surface.

Geometry relaxation and calculated the electronic structure of the same SiNW:H using numerical atomic orbital basis sets in the OpenMX implementation of Ozaki et al<sup>92</sup> are also performed. Norm-conserving pseudopotentials are used. Also, the inputs of force threshold, approximate exchange-correlation functional and k-point sampling are the same as in the plane wave calculations. The basis size for Si was varied while keeping a minimal basis set (s1) for H. A systematic convergence test of the quality of the basis set for Si was performed by increasing the number of primitive orbitals describing the valence electrons and by adding higher angular momentum functions (d-polarisation).

In Table 3.1, two tests are summarised (a graphical representation of the data follows in Figure 3.2). Firstly the total energy per atom (Figure 3.2(a)) is considered. It decreases with increasing the contraction and/or adding polarisation function until

convergence to less than 0.1 meV per atom. This is a minimum requirement regarding the basis set sufficiency of NAOs and it is demonstrated here for the extended system of SiNWs.

The optimisation of orbitals overall yields significant improvement and it becomes less important as the number of contractions increases as may be expected. An important feature is the apparent lower energy of the double-zeta (s2p2) and triple-zeta (s3p3) basis sets compared to the single-zeta with d-polarisation functions (s1p1d1) which nevertheless yields some erroneous results. Use of a minimal basis set for Si (SZ, DZ, TZ from the OpenMX library and their optimised counterparts) yields a stretched Si-H bond with length 1.68 Å, much longer than the typical Si-H bond length. As a result the silicon surface is not properly saturated, thus, affecting the band structure. In contrast to expectations from simple zone-folding of bulk-Si bands<sup>124</sup> and the plane wave calculations, an indirect gap was observed. It is found that it is necessary to add d-polarisation functions to silicon in order to obtain the experimental bond length of 1.5 Å. This also improved the quality of the band structure yielding a direct band gap as can be deduced from Figure 3.3.

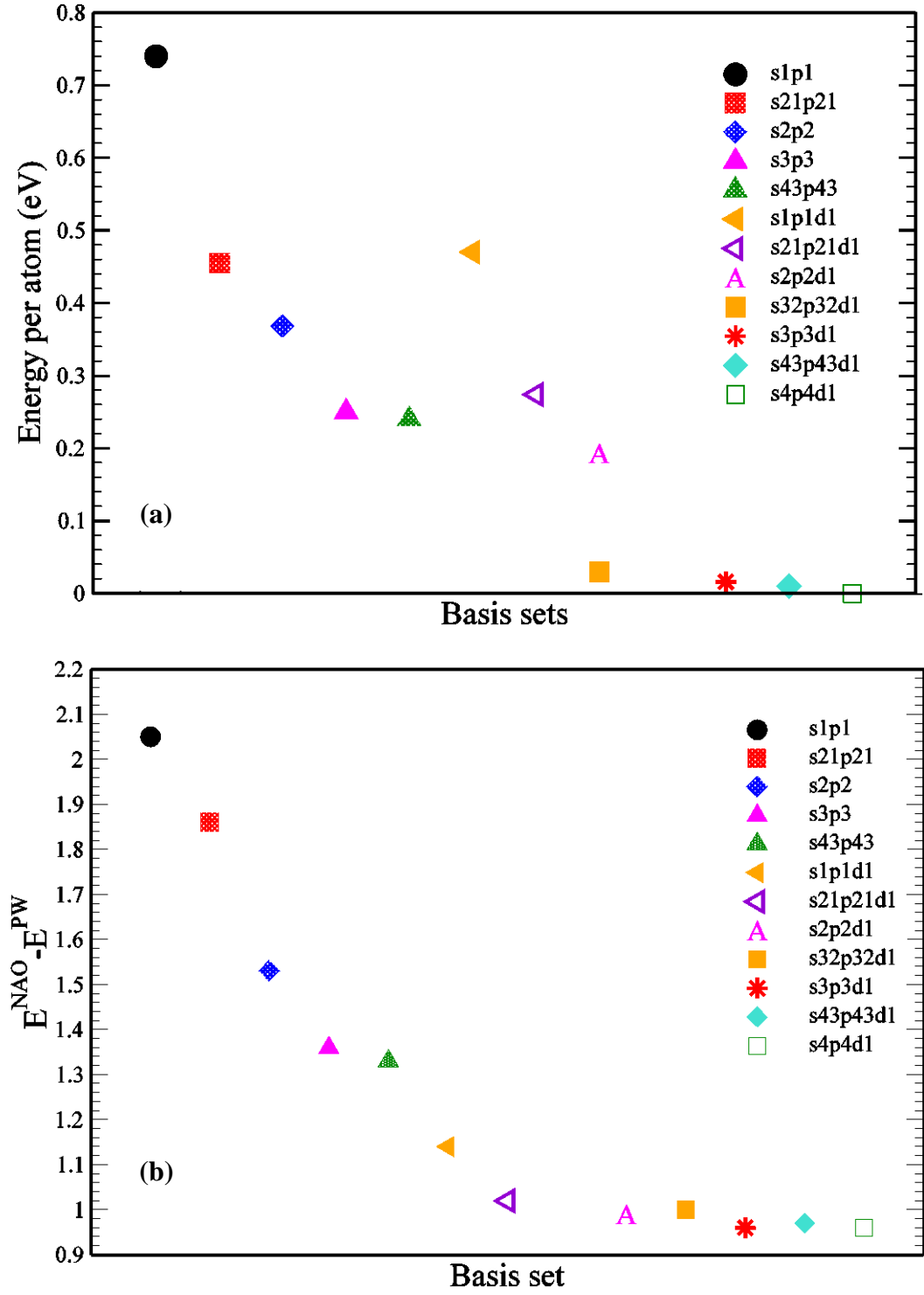


**Figure 3.2:** (a) Variation of the total energy per atom in  $\langle 110 \rangle$ -oriented hydrogenated silicon nanowire ( $\text{Si}_{24}\text{H}_{16}$ ) for different numerical atomic basis sets with respect to s4p4d1. (b) Difference in the band gap energies obtained from the numerical atomic orbital basis sets with respect to plane waves.

**Table 3.1:** The total energy per atom and the band gap of the <110>-oriented nanowire with unit cell  $\text{Si}_{24}\text{H}_{16}$ , calculated using numerical atomic basis sets as implemented in OpenMX. Various contraction schemes are shown along with optimized basis sets. The band gap is consistently overestimated compared to the plane wave calculation. In the last column the band gap of bulk Si is shown as reference.

<b>Basis set on Si</b>	<b>Total energy per atom (eV)</b>	<b>Band gap (eV)</b>	<b><math>E_g^{\text{NAO}} - E_g^{\text{PW}}</math></b>	<b>Band gap of Bulk Si</b>
s1p1	-71.139	3.32	2.05	0.98
s21p21	-71.424	3.13	1.86	0.91
s2p2	-71.511	2.80	1.53	0.91
s3p3	-71.629	2.63	1.36	0.90
s43p43	-71.639	2.6	1.33	0.90
s1p1d1	-71.408	2.41	1.14	0.88
s21p21d1	-71.605	2.29	1.02	0.86
s2p2d1	-71.686	2.26	0.99	0.86
s32p32d1	-71.849	2.27	1.0	0.83
s3p3d1	-71.863	2.23	0.96	0.83
s43p43d1	-71.869	2.24	0.97	0.82
s4p4d1	-71.879	2.23	0.96	0.82

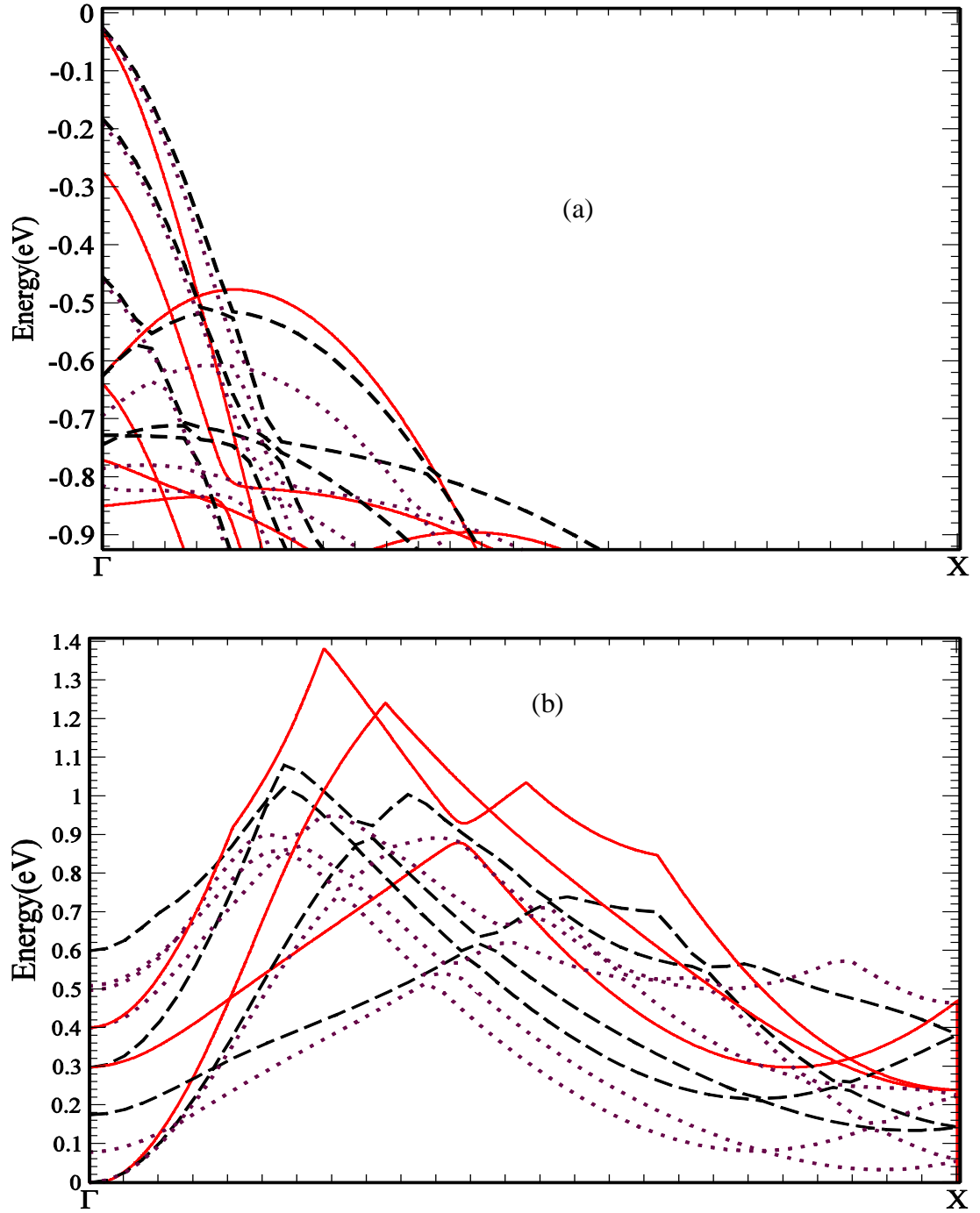


**Figure 3.3:** Comparison of the (a) valence and (b) conduction (sub-) bands of hydrogenated SiNWs ( $\text{Si}_{24}\text{H}_{16}$ ) calculated using PWs (Red solid lines), double-zeta polarised NAOs (purple dotted lines) and optimised double-zeta polarised NAOs (black dashed lines). All curves have been referenced to the top (bottom) of the valence (conduction) bands.

As a second test we look at the band gap difference with respect to the PW calculation (Figure 3.2(b)). The underestimation of the band gap in DFT is a well-known issue and such an analysis can only be used qualitatively.<sup>65</sup> For example, the calculated band gap for bulk Si obtained from a plane wave calculation is 0.8 eV and this should be compared to the experimental value of 1.11 eV. In this chapter, and in the future, we are interested in retrieving and assessing basic device modelling parameters from the band structures. This comparison then serves as a preamble to the results of Section 3; a variation of 25 meV around the saturation value would hint to a converged electronic structure calculation from which the required quantities can be extracted. The size of the NAO band gap decreases with the extended basis sets. However, it is 75.6% larger compared to the PW calculation as commonly observed. The band gap of bulk Si is also shown in the last column of Table 3.1 as reference. Again there is convergence with increasing basis set size and contractions towards 0.82 eV. This is just 0.02 eV larger than the plane wave calculation, implying that the difference between the plane wave and NAO band gap grows due to quantisation as the diameter of the nanowire decreases. One contributing factor could be the lower effective mass obtained with NAOs (discussed later in Section 3.3) which increases the band gap widening at small diameters.

It is stressed again that simply using more orbitals to optimise the minimal basis set is not sufficient to yield the correct electronic structure. For example, the contracted orbital basis s21p21d1 with total of 9 basis functions performs better compared to s3p3 or s43p43 having 12 basis functions. As mentioned previously higher angular momenta functions (d-polarisation) are needed to yield the correct band gap character. Further improvement of the bands is obtained by increasing contraction combined with orbital optimisation as implemented in OpenMX. Interestingly, the

use of optimised orbitals for a fixed size basis set is not as significant as for the total energy calculations. A direct contrast between the first few valence and conduction bands of PW and NAO calculations is shown in Figure 3.3. For comparison, we have referenced the energy with respect to the top of the valence band and shifted the NAO conduction bands by the difference between the OpenMX and Quantum Espresso band gaps. The qualitative and quantitative agreement between the PW and the NAO valence sub-bands is remarkable (Figure 3.3(a)). Comparing the conduction sub-bands yields a qualitative similar picture of electronic structure but it apparently lacks in accuracy (Figure 3.3(b)). This is understood given the delocalised nature of the conduction bands. A more quantitative analysis follows in Section 3.3.

**Table 3.2:** CPU time with respect to size of basis sets for SiNW:H using the same hardware configuration and calculation inputs.

Basis set on Si	CPU time (Hours)
s1p1	1.45
s21p21	1.03
s2p2	2.26
s32p32	2.21
s1p1d1	3.87
s21p21d1	3.81
s2p2d1	4.34
s32p32d1	4.21
s3p3d1	6.04
s43p43d1	5.67
s4p4d1	7.01



Finally, to demonstrate the gain in computational time by using smaller basis sets in Table 3.2 we compare the CPU time for structural relaxation of the SiNW:H supercell using different NAOs. The data clearly show the increase in CPU time with increasing contraction and addition of d-polarisation orbitals. It is also seen that calculations with optimised orbitals require almost similar CPU time as their corresponding with primitives, e.g., s32p32d1 and s2p2d1 basis sets.

### 3.2.2 Hydroxylated silicon nanowires

The hydroxylated SiNWs were obtained by simple substitution of the hydrogen passivation with –OH surface terminating groups. This structure serves as a minimal model to investigate oxygen-silicon bonding as this simple substitution changes the oxidation state of the silicon atoms at the surface.<sup>76</sup> First we inspected the O-H and Si-O bond lengths in the optimised geometries to check the performance of the various NAO contracted schemes. Based on the results for hydrogenated SiNWs and previous studies on the directional Si-O bonding,<sup>125</sup> d-polarisation orbitals for both Si and O for the geometry relaxations are used; otherwise the obtained geometries are unreasonable. The use of polarised orbital for H does not change the results. The relaxed geometry has Si-Si and Si-O bond lengths of 1.7 Å and 0.98 Å, respectively, which are close to the theoretical and experimental values of crystalline silica<sup>126</sup>. The O-H bond length is 0.98 Å which is typical for the hydroxyl group. The cross-section of the simulated wire is shown in Figure 3.1(b).

In Table 3.3, the total energy and the band gap difference between the NAO and the PW calculations is shown for various NAO basis sets. As previously, the total energy can be seen to reduce with increasing the basis contraction or orbital optimisation and converge to less than 0.1 eV per atom.

**Table 3.3:** The total energy per atom of the <110>-oriented nanowire with unit cell  $\text{Si}_{24}\text{O}_{16}\text{H}_{16}$ , calculated using numerical atomic basis sets as implemented in OpenMX. Various contraction schemes are shown along with optimized basis sets. The band gap is consistently overestimated compared to the plane wave calculation.

Basis set on Si and O	Total energy per atom (eV)	Band gap (eV)	$E_g^{\text{NAO}} - E_g^{\text{PW}}$ (eV)
s1p1d1	-177.1932	1.34	0.38
s21p21d1	-177.3409	1.32	0.36
s2p2d1	-177.5383	1.25	0.29
s32p32d1	-177.6795	1.26	0.30
s3p3d1	-177.7185	1.26	0.30
s43p43d1	-177.7258	1.26	0.30
s4p4d1	-177.7617	1.25	0.29

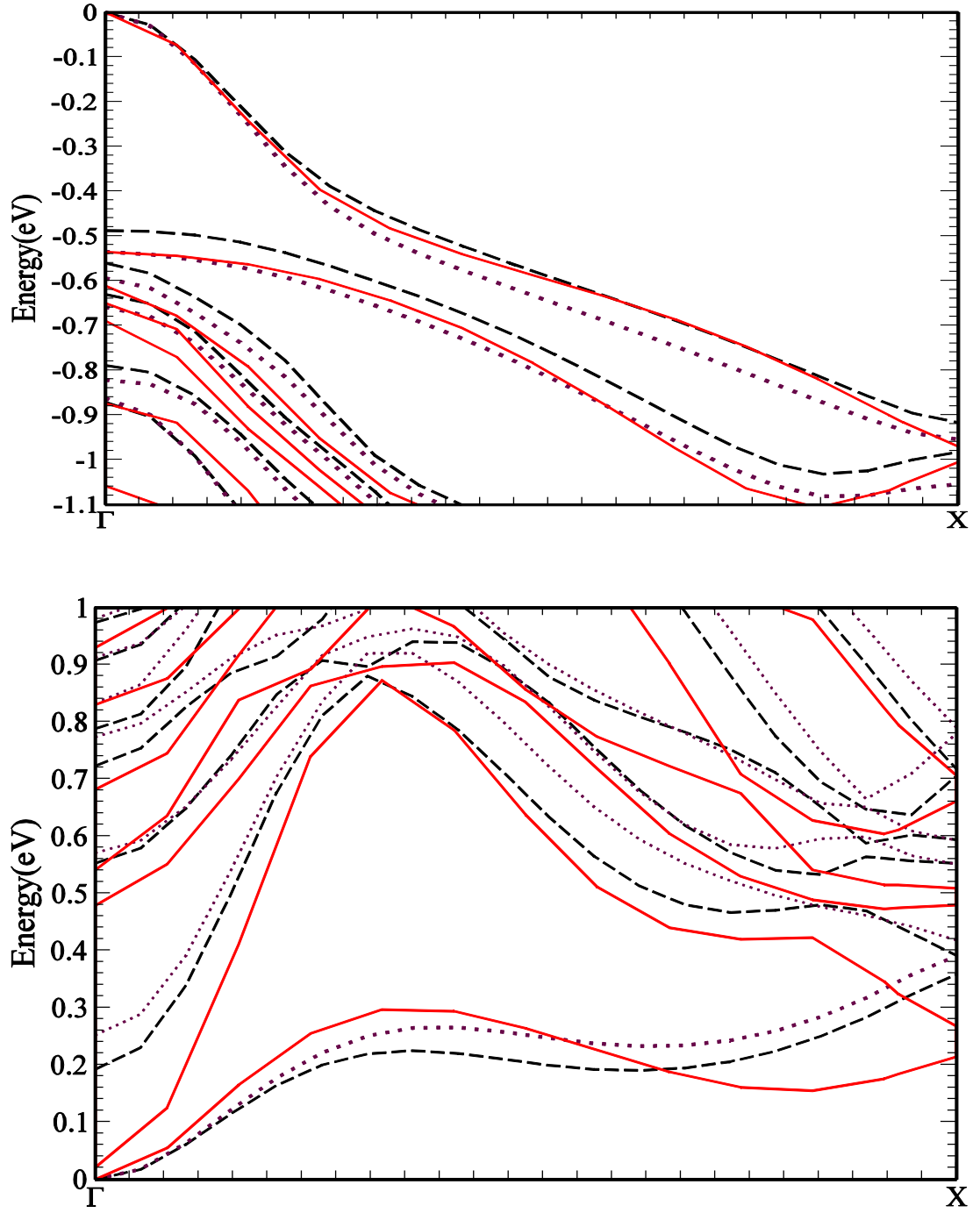


**Figure 3.4:** Comparison of the (a) valence and (b) conduction (sub-) bands of hydroxylated silicon nanowires (Si<sub>24</sub>O<sub>16</sub>H<sub>16</sub>) calculated using plane waves (red solid lines), double-zeta polarized NAOs (purple dotted lines) and optimized double-zeta polarized NAOs (black dashed lines). All curves have been referenced to the top (bottom) of the valence (conduction) bands.

The band gap obtained from the plane wave calculation is 0.96 eV. This is smaller than the 1.27 eV band gap of SiNW:H and it is attributed to orbital hybridisation.<sup>65</sup> The respective values for the NAO basis sets are 2.23 eV for SiNW:H and 1.25 eV for SiNW:OH. Using the PW result as a benchmark, the NAO implementation consistently overestimates the band gap, similarly to the hydrogenated SiNWs. The comparison between the PW and NAO band structures is shown in Figures 3.4(a) and 3.4(b) for the first few valence and conduction sub-bands, respectively. The fair agreement for the occupied states compared to the empty conduction band states is confirmed. A graphical representation of the results shown in Table 3.3 is shown in the Figure 3.5.

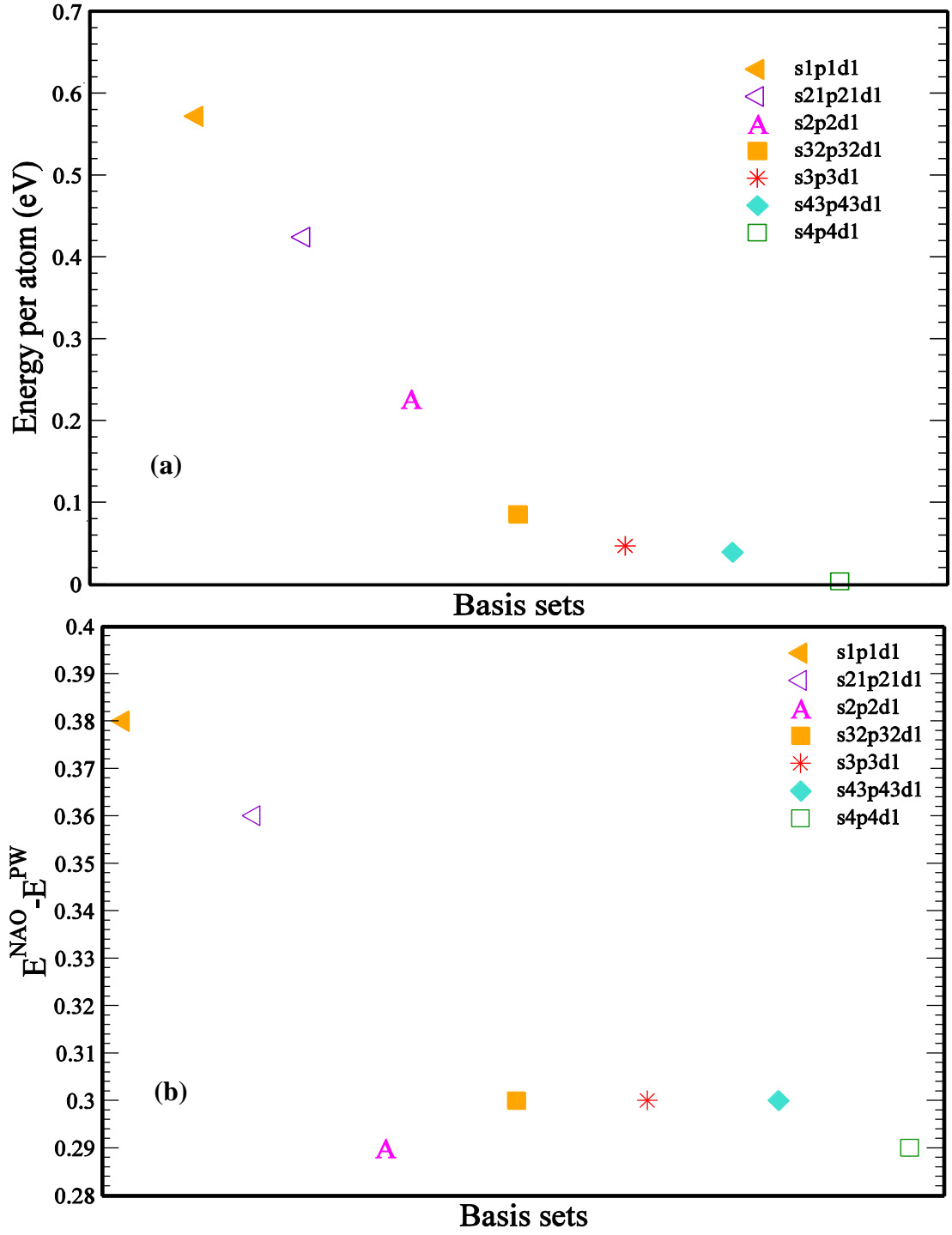


**Figure 3.5:** (a) Variation of the total energy per atom in  $\langle 110 \rangle$ -oriented hydroxylated silicon nanowire ( $\text{Si}_{24}\text{O}_{16}\text{H}_{16}$ ) for different numerical atomic basis sets with respect to s4p4d1. (b) Difference in the band gap energies obtained from the numerical atomic orbital basis sets with respect to plane waves.

### 3.3 Analysis of band structure properties

Deviations in the second and first derivatives of the various sub-bands, which yield

respectively the effective masses  $m_i = \hbar^2 \left( d^2 E / dk^2 \right)_i^{-1}$  and group velocities  $v_g^i =$

$\hbar^{-1} (dE/dk)_i$ , have a quantitative effect on the calculation of transport quantities

such as conductivity and mean free path. In the theory of mesoscopic transport and

in the relaxation time approximation, the conductivity is,  $\sigma = e^2 \sum_{i=1}^{N_C} \frac{n_i \tau_i}{m_i}$ , where

$N_C$  is the number of contributing subbands and  $n_i$ ,  $m_i$  and  $\tau_i$  are electron density,

effective mass and relaxation time of the  $i$ -th sub-band at the energy of the injected

charge carriers; the average mean free path equals  $l = 1 / N_C \sum_{i=1}^{N_C} v_g^i \tau_i$ .<sup>129</sup> To study

the sub-bands properties for different NAO basis sets and compare with the PW

method, the effective mass and group velocity of hydrogenated SiNW for the first

three sub-bands above (conduction) and below (valence) the Fermi level is

calculated. This covers the typical energy range of injected charge carriers. For this

purpose, each sub-band was fitted in a small interval near the  $\Gamma$ -point and elsewhere

in the first Brillouin zone. A polynomial method was implemented for fitting curves

yielding first and second derivatives for the calculation of  $v_g^i$  and  $m_i$ , respectively.

In Table 3.4, results for both electrons (conduction bands) and holes (valence bands)

are summarised for the commonly referenced  $\Gamma$ -point. They are in good agreement

with other computational works which are close to  $0.15m_e$  for electron effective

mass and  $0.20 m_e$  for hole effective mass.<sup>58,68,69</sup> The effective mass and group

velocity for the top-valence and bottom-conduction bands are plotted in Figures 3.6

and 3.7, respectively, for  $k$  values corresponding to the indicated energy range

(which is within 0.1 eV from band extrema). It is observed that the effective masses

predicted from the various NAO basis are slightly overestimated compared to the values derived from the PW calculations. The opposite holds for the group velocity  $v_g^i$ . These results indicate that there is a minor underestimation of the mean free path by at most 4%, whereas, variations in the effective mass may yield up to 65% lower conductivity.

**Table 3.4:** Predicted electron and hole effective masses at the  $\Gamma$ -point using various basis sets.

<b>Basis sets</b>	<b>Electron effective mass (<math>m_e</math>)</b>	<b>Hole effective mass (<math>m_e</math>)</b>
plane waves	0.15	0.20
s2p2d1	0.12	0.11
s32p32d1	0.12	0.12
s43p43d1	0.12	0.12

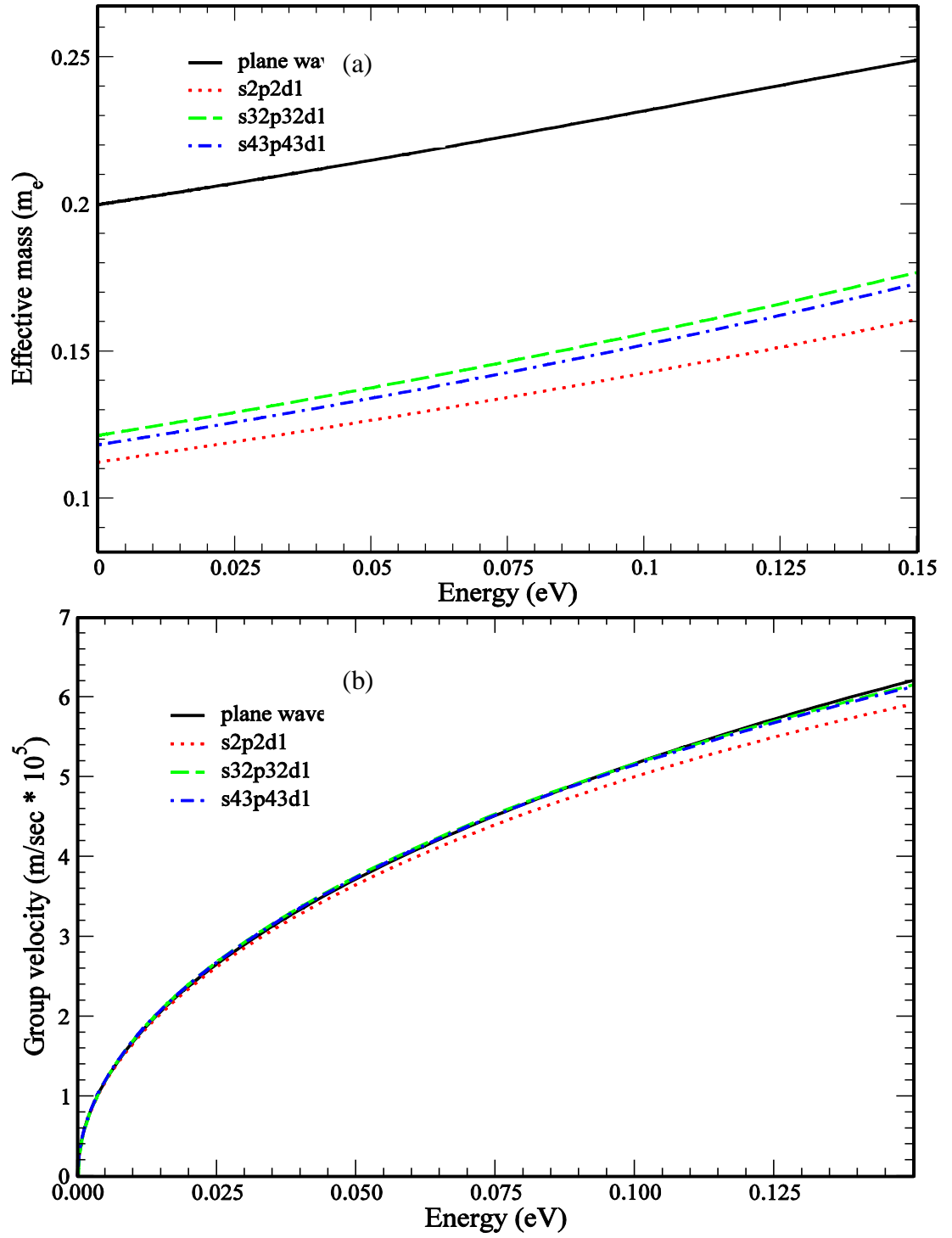


**Figure 3.6:** Predicted (a) effective mass and (b) group velocity of carriers within the energy range of the first valence band using the basis sets as indicated.



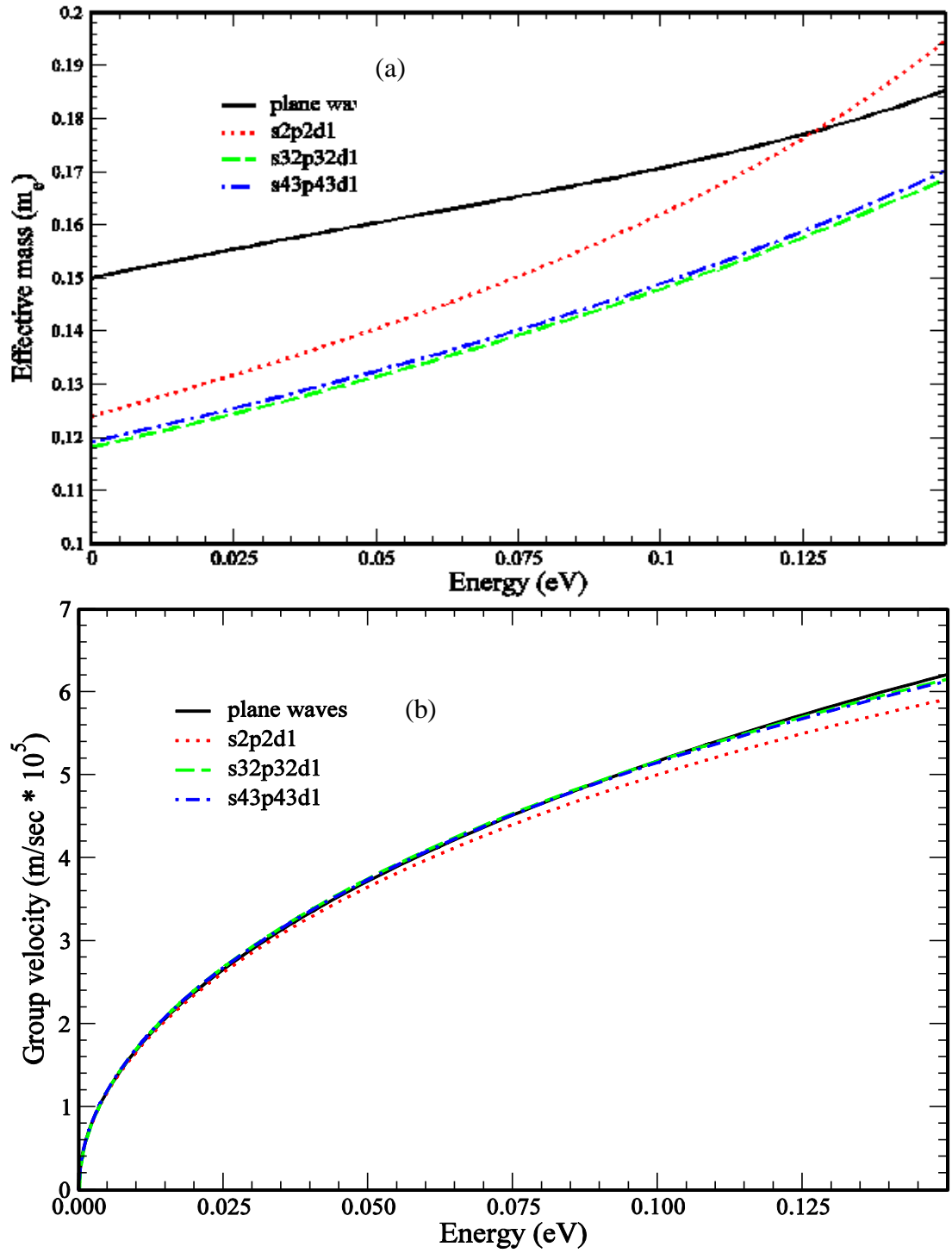


**Figure 3.7:** Predicted (a) effective mass and (b) group velocity of carriers within the energy range of the first conduction band using the basis sets as indicated.

In Table 3.4, results for both electrons (conduction bands) and holes (valence bands) are summarised for the commonly referenced  $\Gamma$ -point. They are in good agreement with other computational works.<sup>58,68,69</sup> The effective mass and group velocity for the

top-valence and bottom-conduction bands are plotted in Figures 3.6 and 3.7, respectively, for  $k$  values corresponding to the indicated energy range (which is within 0.1 eV from band extrema). It is observed that the effective masses predicted from the various NAO basis are slightly overestimated compared to the values derived from the PW calculations. The opposite holds for the group velocity  $v_g^i$ . These results indicate that there is a minor underestimation of the mean free path by at most 4%, whereas, variations in the effective mass may yield up to 65% lower conductivity.

### 3.4 Transferability of optimised numerical atomic orbitals

The transferability of optimised orbitals is explored by two types of control calculations. First, by considering hydrogenated SiNWs with three different orientations  $\langle 100 \rangle$ ,  $\langle 110 \rangle$  and  $\langle 111 \rangle$  (see Figure 3.1(a) and inset of Figure 3.8) the NAOs as obtained from different systems and compared their electronic structure are exchanged. For example, the contracted orbitals obtained after orbital optimisation in  $\langle 110 \rangle$ -oriented SiNW:H as inputs for calculations with  $\langle 100 \rangle$ - and  $\langle 111 \rangle$ -oriented SiNW:H are taken. For a fixed orientation, the total energies obtained after geometry relaxation are equal for the various NAO basis sets independent on the wire orientation used for the orbital optimisation. This procedure also yields almost identical band structures as shown in Figure 3.7.

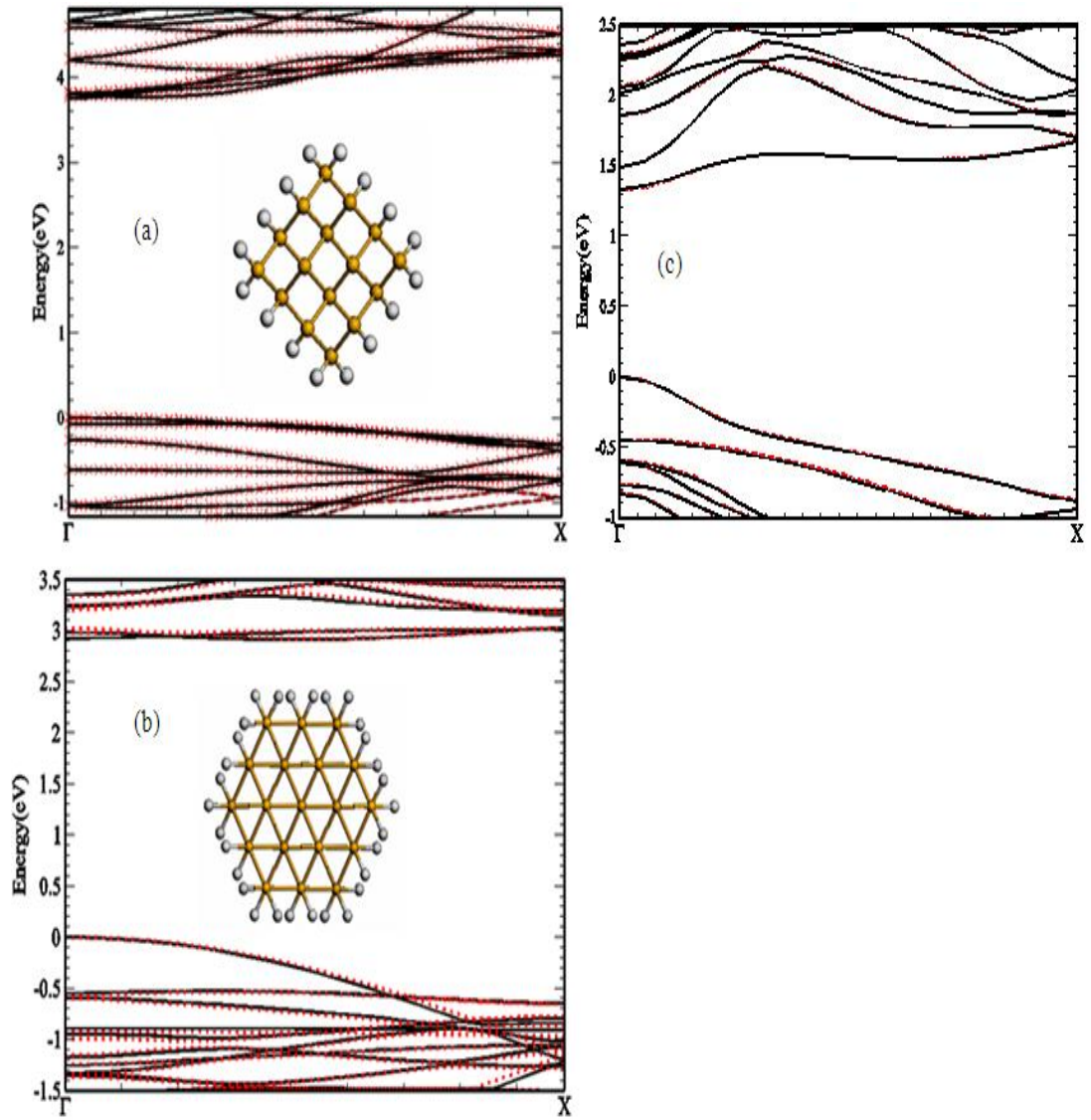


**Figure 3.8:** Transferability comparison of optimised numerical atomic orbitals. (a) Band structure of <100>-oriented SiNW:H using optimised orbitals obtained from <110>-oriented SiNW:H (black solid line) and by performing orbital optimisation for <100>-oriented SiNW:H (red dotted line). (b) Band structure of <111>-oriented SiNW:H using optimised orbitals obtained from <110>-oriented SiNW:H (black solid line) and by performing orbital optimisation for <111>-oriented SiNW:H (red dotted line). (c) Band structure of <110>-oriented SiNW:OH using optimised orbitals (silicon) for <110>-oriented SiNW:H (black solid line) and by performing orbital optimisation for <110>-oriented SiNW:OH (red dotted line).

In the second and more intriguing test, the NAOs that describe the Si atoms in hydrogenated SiNWs are taken, optimised them and used them as inputs for calculations with hydroxylated SiNWs. The same procedure was applied vice versa (i.e., optimised Si-atom NAOs from SiNW:OH used in SiNW:H). Also in this case electronic structure results do not depend on the optimisation environment, as demonstrated by the identical band structures in Figure 3.8. This procedure can prove very efficient in larger nanowires (or indeed other systems) where orbitals can be optimised in a small controlled environment and then transferred to the bigger system.

### 3.5 Conclusions

In this chapter the implementation of numerical atomic basis sets by studying the structure is evaluated, total energy and electronic bands of silicon nanowires with hydrogen and hydroxyl terminations. It has been shown that there is systematic improvement with respect to the basis size and orbital optimisation. It was estimated that the mean free path is not significantly affected but predictions of the conductivity can be up to 65% lower. Total energies converge by adding contractions with higher angular momentum. Both plane wave basis set and atomic orbital basis set give qualitative and quantitative similar valence bands whereas conduction bands improve with higher atomic basis sets. However, optimised NAOs offer a good compromise to study SiNWs with fixed basis size, in particular, within the double-zeta polarised approximation. It is also established that there is some transferability of optimised NAOs which can be used to address nanowire calculations in more complex (larger) environments. These results put on a firm basis the use of NAOs as an efficient method, alternative to plane waves, to calculate the properties of silicon nanowires.

## **Chapter 4: Structural, electronic and transport properties of doped silicon nanowires**

### **4.1 Chapter introduction**

One can change the electronic and optical properties through doping of the SiNWs<sup>128</sup> as demonstrated by evidence on tuneable control of their conductivity and photoluminescence.<sup>20,129</sup> Therefore a detailed understanding of the structural and electronic properties of doped SiNWs is important. In particular, there is a growing need to address materials transport properties and large-scale device simulations from first principles where dopants are introduced in the source and drain regions as well as in the channel due to unintentional or intentional doping. Such examples are discussed Chapters 5 and 6. To this end, a good compromise between efficiency and accuracy is sought<sup>112</sup> and atomic orbitals offer a tractable basis sets. Nevertheless, as discussed in the previous chapter a systematic approach is needed prior to applying them in practice.<sup>94,114</sup>

In this chapter DFT is employed to investigate the electronic structure of <100>-oriented hydrogenated SiNWs with diameter of 1.15 nm and highly-doped with boron, phosphorous, arsenic and gallium. These nanostructures are particularly relevant for the recent proposal of junctionless transistors<sup>55</sup> where doping concentrations as high as  $10^{21} \text{ cm}^{-3}$  are required. The convergence of different expansions of primitive and contractions of optimised NAOs by studying the structural and electronic properties of SiNWs with an uneven distribution of dopants has been reported.

The structure of the chapter is as follows. In Section 4.2 the implementation of numerical atomic basis sets by studying the total energy and electronic bands of

silicon nanowires with hydrogen surface terminations and doped with B, P, As and Ga atoms (see Figure 4.1) has been reported. In section 4.3 a first discussion of how charge-carrier transport properties are affected in the conduction and valence bands depending on the dopant type has been reported. An estimate of the mean free path is also derived.

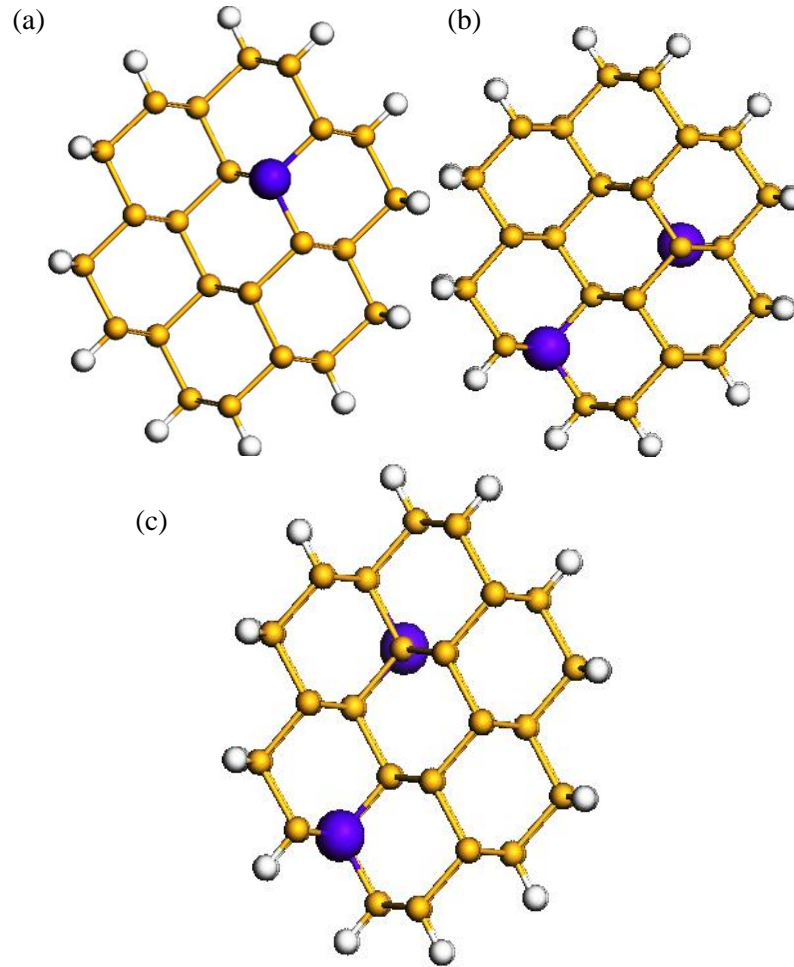


**Figure 4.1:** Cross section of  $\langle 110 \rangle$ -oriented (geometrically optimised) doped silicon nanowires. In (a), a single gallium atom acts as substitutional dopant ( $\text{Si}_{23}\text{Ga}_1\text{H}_{16}$ ). Substitutional dopants (B, Ga, As, P) are distributed at two different uneven locations assigned as configuration 1 in (b) and configuration 2 in (c).

## 4.2 Electronic properties of doped silicon nanowires

Three models of SiNWs are considered. Firstly, gallium has been placed substitutionally at 2.5% (see Figure 4.1(a)). To study the effect of dopant-dopant interaction, we doubled the supercell size and placed dopants at uneven sites. These are configurations 1 and 2 in Figures 4.1(b) and 4.1(c). Substitutional doping of hydrogen passivated SiNWs is achieved by exchanging silicon atoms in the supercell with B, P, Ga and As atoms.

DFT calculations were performed with the PBE generalized gradient approximation (GGA) to the exchange and correlation functional. Norm-conserving fully relativistic pseudopotentials and numerical atomic basis functions are generated by the software package ADPACK.<sup>156</sup> A Monkhorst-Pack k-point sampling on a  $15 \times 1 \times 1$  and  $7 \times 1 \times 1$  grid in the Brillouin zone along the nanowire axis direction is used for the unit cell and the doubled supercell respectively. The SiNW is put in a supercell with more than  $24 \text{ \AA}$  spacings in the lateral directions to avoid any interactions between the neighbouring image nanowires. The SiNWs and the unit cell lattices are fully relaxed. Structural optimisation calculations are performed until the absolute value of force acting on each atom is less than  $0.01 \text{ eV/\AA}$ . The geometry-optimised cross-section of the Ga-doped SiNW is shown in Figure 4.1(a).

The systematic convergence of the quality of the basis sets is performed by increasing the number of primitive orbitals describing the valence electrons and by adding higher angular momentum functions (d-polarisation). The total energy and electronic structure calculated using a hierarchy of basis sets, from single- $\zeta$  minimal to multiple- $\zeta$  with polarization orbitals were compared. The basis size for the silicon and dopant atoms was varied while keeping a minimal basis set (s1) for H. The

minimal basis set for Ga and As is s1p1d1 and the starting point is to include d-orbital polarisation functions also for Si.

The convergence of the energy per atom is shown in Table 4.3. The calculated total energy for the various NAO basis sets reduces with increasing the basis size and/or applying orbital optimisation as can be seen in Figures 4.2, 4.3 and 4.4. Unless explicitly indicated, there is no difference between the dopant configurations 1 and 2 in Figures 4.2 and 4.3. By increasing the contraction and adding d-orbital polarisation functions, the total energy per atom converges to less than 0.01 eV per atom. This is a minimum requirement regarding the basis set sufficiency of NAOs and it is demonstrated here for the extended system of SiNWs. The respective convergent band gap values for the NAO basis sets using s32p32d1 basis sets are 2.04 eV, 1.89 eV, 1.63 eV and 2.46 eV for SiNWs doped with B, P, As and Ga, respectively. The optimisation of orbitals overall yields significant improvement and it becomes less important as the number of contractions increases as may be expected.

A simple inspection of Figures 4.2 to 4.4 may suggest that optimised orbitals do not yield significant improvements when multiple- $\zeta$  basis sets are used. This may hold well for the structural properties. But the previous comparison with plane wave benchmark calculations for the hydrogenated and hydroxylated SiNWs of Chapter 3 has indicated that electronic structure features and transport properties derived thereafter greatly improve by orbital optimisation. This is demonstrated in Figure 4.5 (in particular 4.5(b)) by comparing the band structures between primitive and optimised double- $\zeta$  polarised NAOs for the first few valence and conduction sub-bands. The sensitivity to orbital optimisation is smaller for the valence electronic states.



**Table 4.3:** The total energy per atom of the <110>-oriented nanowire with unit cell  $\text{Si}_{23}\text{Ga}_1\text{H}_{16}$ , calculated using numerical atomic orbital basis sets as implemented in OpenMX. Various expansion schemes are shown along with optimized basis sets.

Basis set on Si and Ga	Total energy per atom (eV)
s1p1d1	-118.5932
s21p21d1	-118.865
s2p2d1	-118.9959
s32p32d1	-119.1376
s3p3d1	-119.1676
s43p43d1	-119.1752
s4p4d1	-119.187

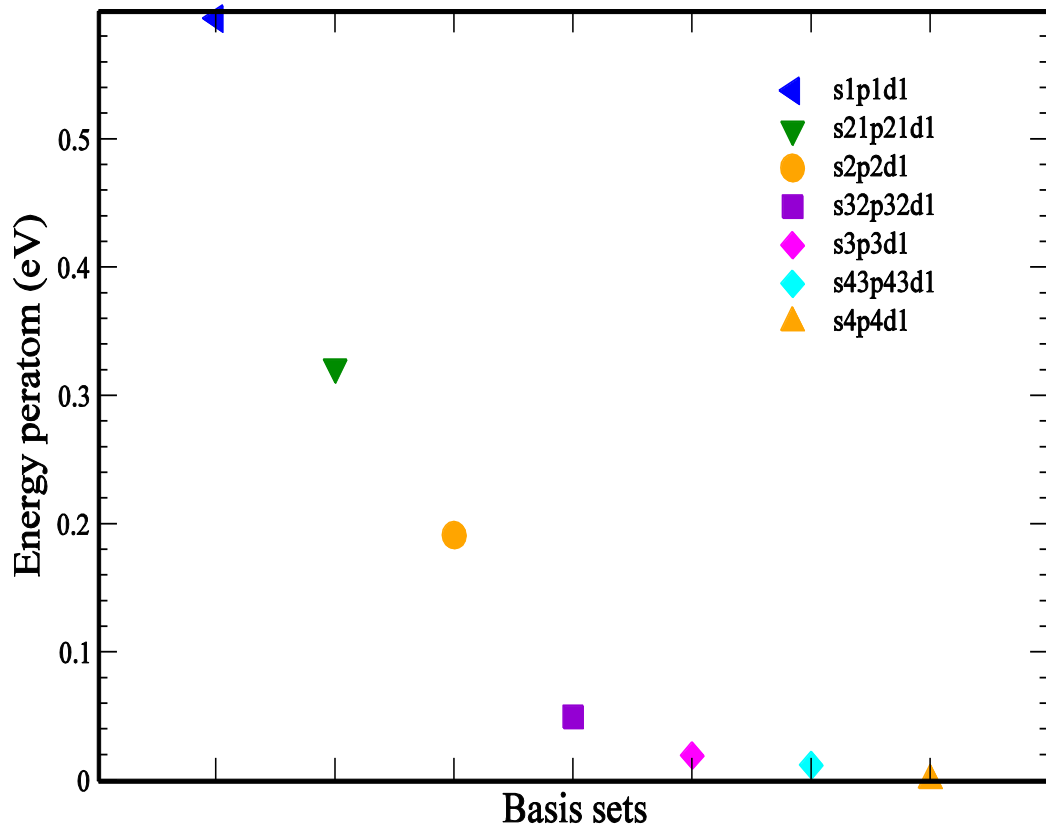


**Figure 4.2:** Variation of the total energy per atom in  $\langle 110 \rangle$ -oriented Ga-doped silicon nanowire ( $\text{Si}_{23}\text{Ga}_1\text{H}_{16}$ ) for different numerical atomic orbitals basis sets. All values are referenced to the calculation using the s4p4d1 NAOs.

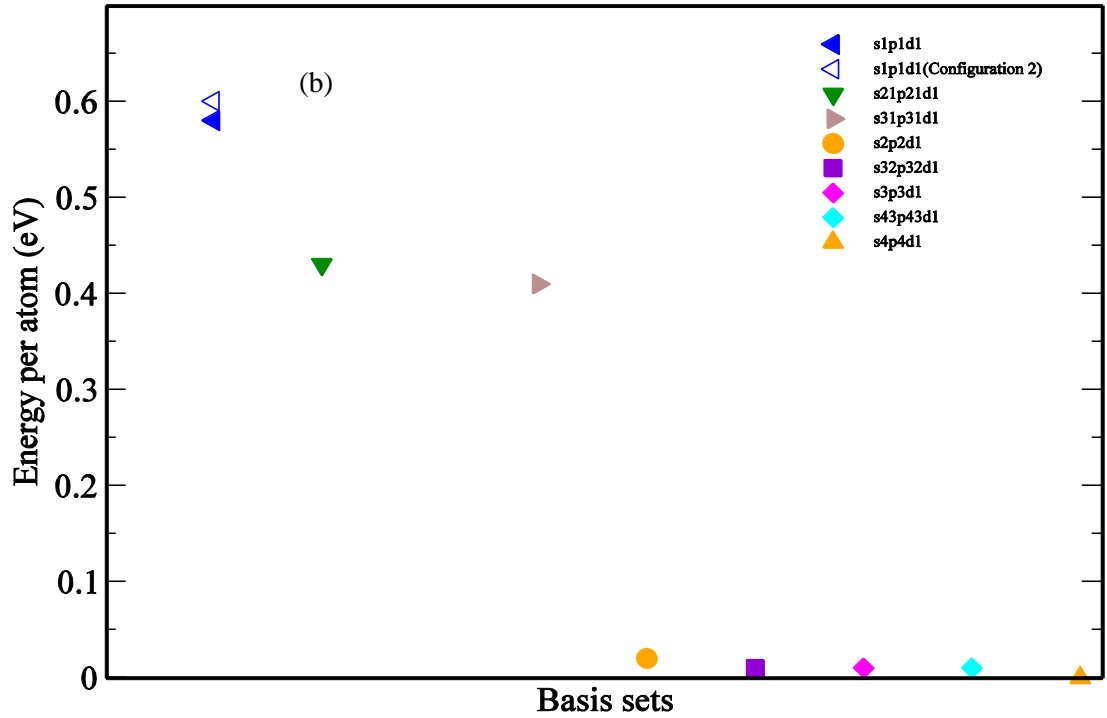
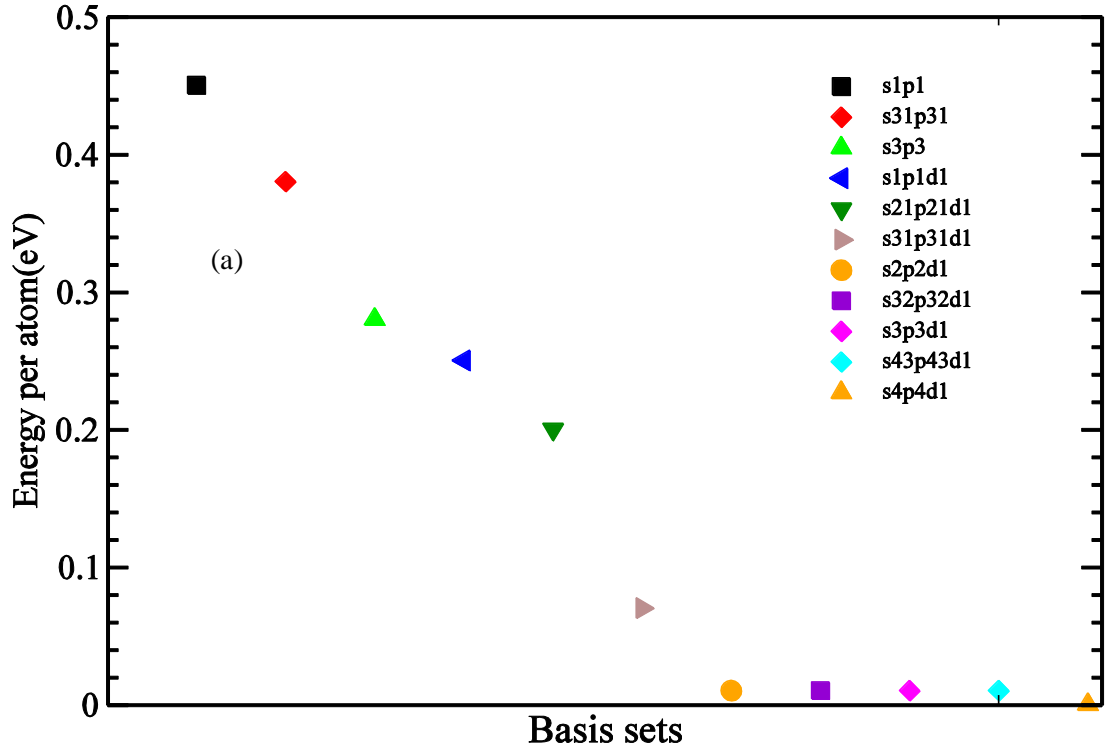


**Figure 4.3:** Variation of the total energy per atom in  $\langle 110 \rangle$ -oriented silicon nanowires for different numerical atomic orbitals basis sets and p-type dopants that is, (a) boron doped ( $\text{Si}_{46}\text{B}_2\text{H}_{32}$ ) and (b) gallium doped ( $\text{Si}_{46}\text{Ga}_2\text{H}_{32}$ ). All values are referenced to the calculation using the s4p4d1 NAOs.

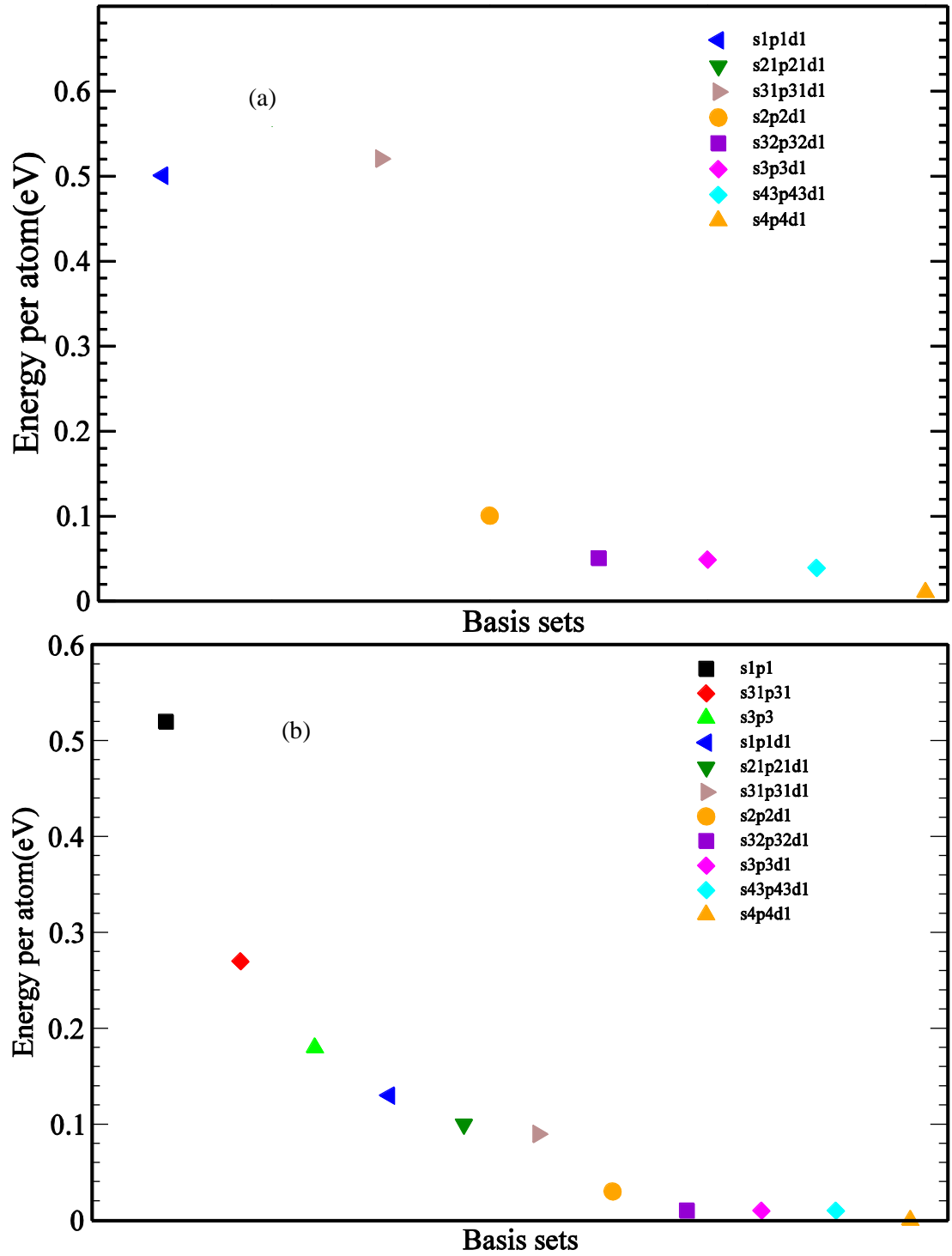


**Figure 4.4:** Variation of the total energy per atom in <110>-oriented silicon nanowires for different numerical atomic orbitals basis sets and n-type dopant atoms, that is, (a) phosphorous doped (Si<sub>46</sub>P<sub>2</sub>H<sub>32</sub>) and (b) arsenic doped (Si<sub>46</sub>As<sub>2</sub>H<sub>32</sub>). All values are referenced to the calculation using the s4p4d1 NAOs.

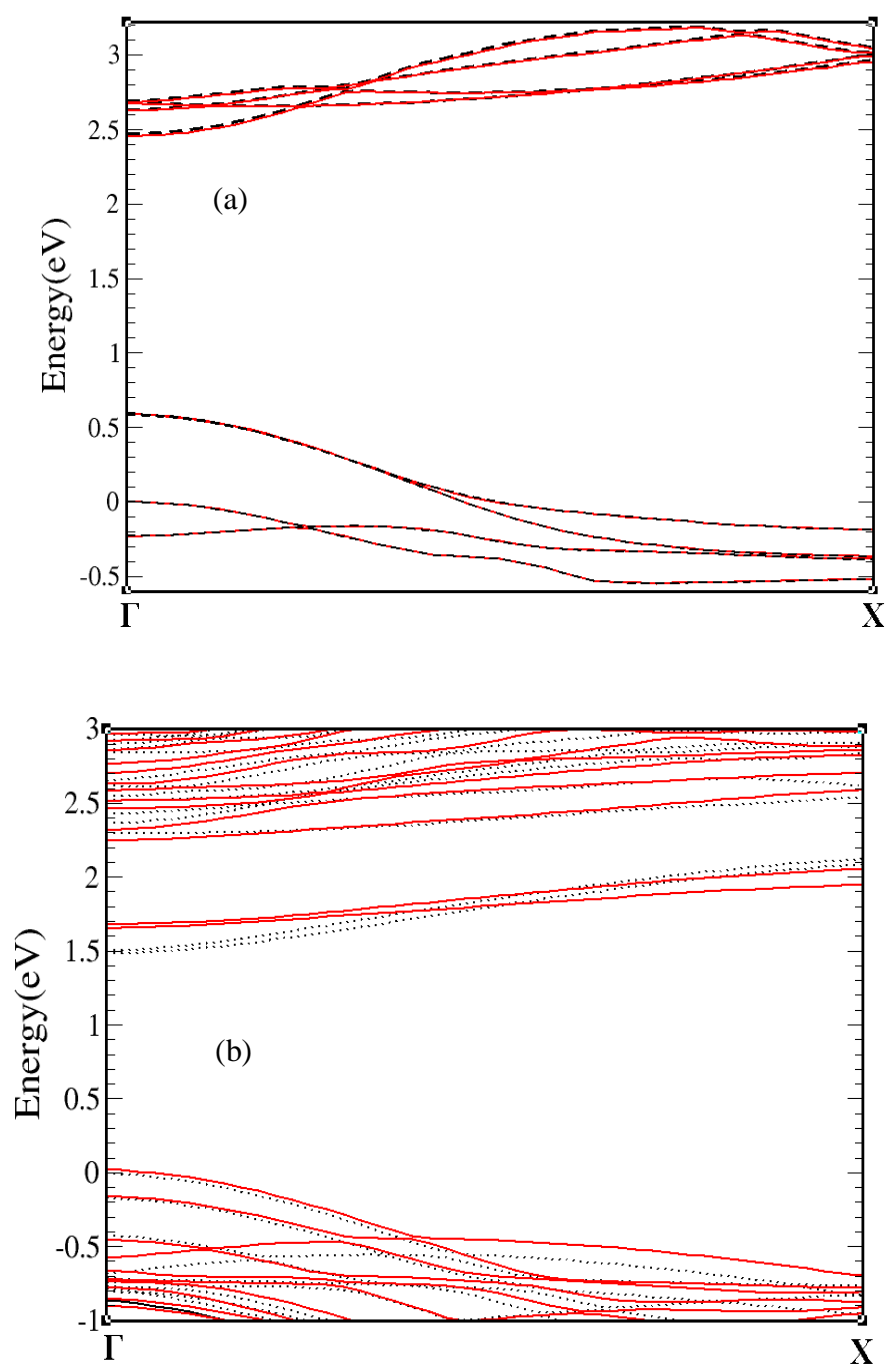


**Figure 4.5:** Comparison of the first few valence and conduction (sub-)bands of (a) gallium doped ( $\text{Si}_{46}\text{Ga}_2\text{H}_{32}$ ) and (b) arsenic doped silicon nanowire ( $\text{Si}_{46}\text{As}_2\text{H}_{32}$ ) calculated using primitive (red solid lines) and optimized double-zeta polarized NAOs (black solid lines).

Finally, the transferability of optimised orbitals is explored by two types of control calculations. First, we consider phosphorus doped SiNWs with three different orientations  $\langle 100 \rangle$ ,  $\langle 110 \rangle$  and  $\langle 111 \rangle$ . The NAOs as obtained from the various systems and compare their electronic structure were exchanged. For example, the contracted orbitals obtained after orbital optimisation in  $\langle 110 \rangle$ -oriented P-doped SiNW as inputs for calculations with  $\langle 100 \rangle$ - and  $\langle 111 \rangle$ -oriented P-doped SiNWs were taken. For a fixed orientation, the total energies obtained after geometry relaxation are equal for the various NAO basis sets independent on the wire orientation used for the orbital optimisation. This procedure also yields almost identical band structures. The result of the comparison for the  $\langle 100 \rangle$  orientation is shown in Figure 4.6. This procedure can prove very efficient in larger nanowires (or indeed other systems) where orbitals can be optimised in a small controlled environment and then transferred to the bigger system.

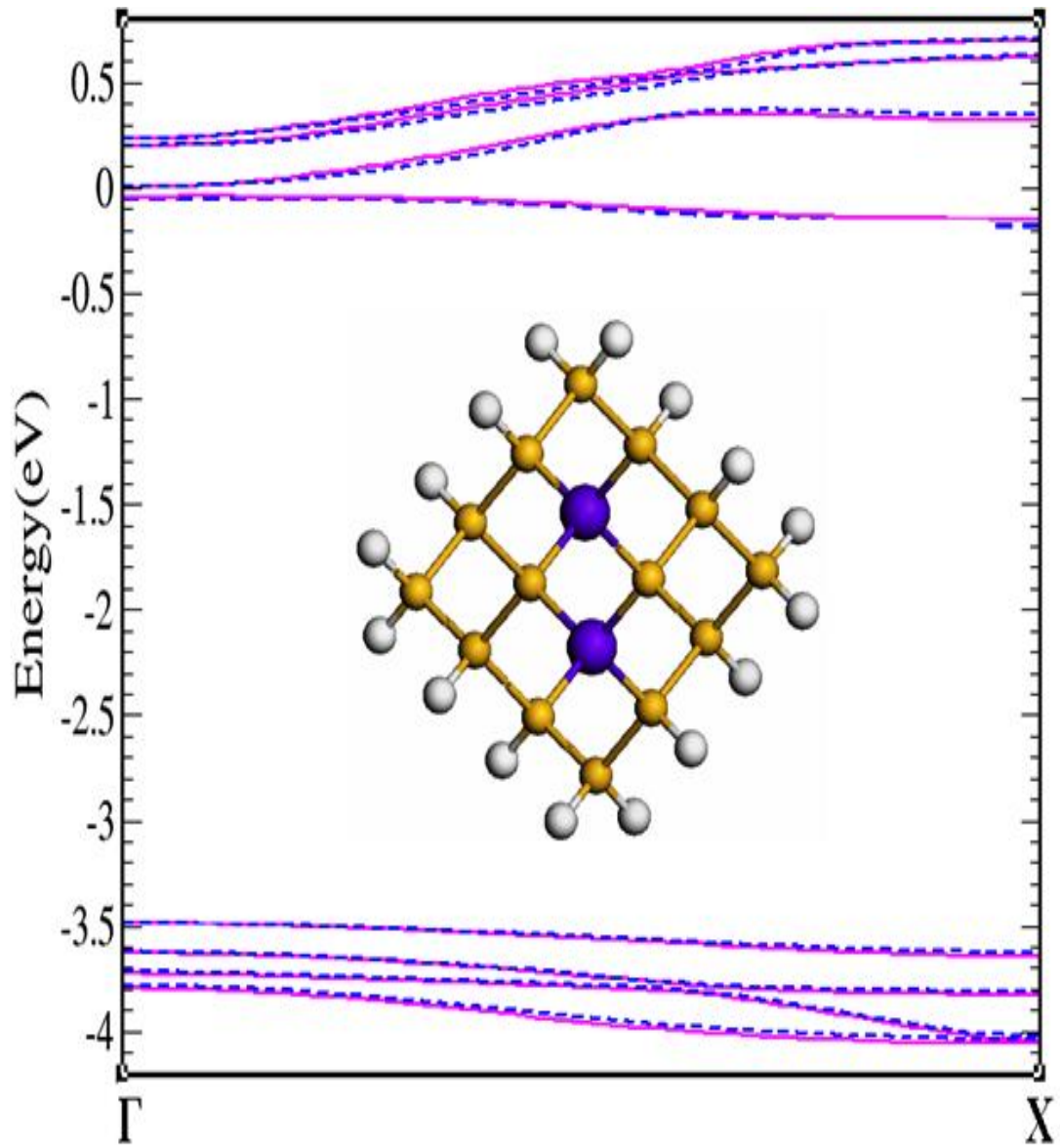


**Figure 4.6:** Transferability comparison of optimised numerical atomic orbitals. The band structure of a  $\langle 100 \rangle$ -oriented P-doped is shown as calculated using orbitals obtained either from optimisation within the same structure (magenta solid lines) or from optimisation performed on  $\langle 110 \rangle$ -oriented nanowires (blue dashed lines).

## 4.3 Scattering properties of n- and p-type dopants in silicon nanowires

In the present section the impact of a single dopant on charge-carrier transport properties is focused. In particular, the scattering of electrons and holes for various n- and p-type dopants is discussed. These are boron and gallium (electron acceptors) and arsenic and phosphorus (electron donors). The transmission is calculated using the Green's function formalism and Kohn-Sham Hamiltonians obtained from OpenMX as indicated in Sections 2.3.2 and 2.5.3. Optimised double zeta basis sets with d polarization (s32p32d1) have been used for these calculations. The supercell used to define the scattering region is depicted in the inset of Figure 4.7. It is noted that the supercell extends to seven unit cells ( $26.88\text{\AA} \times 25\text{\AA} \times 25\text{\AA}$ ) to ensure that there is no residual interaction between the leads, thereby allows use the projection of the leads to self-energies as computational method (see Section 2.3.2). The wire axis is oriented along the  $\langle 110 \rangle$  crystallographic direction and the diameter is 1.15 nm.

In Figure 4.7(a) the transmission for SiNW with a single impurity for energies below the valence band edge and for the first subband have been plotted. Evidently boron and gallium atoms act as strong scatterers. This is attributed to their electronic states closely aligned to the valence band edge. However, the exact dependence is expected to depend on orientation and diameter. Holes injected within the first valence subband would show weak scattering in the presence of P and As dopants; for example, this configuration could arise in  $n^+p\text{-}n^+$  transistor junctions. In contrast, strong (weak) scattering is observed for P and As (B and Ga) in the first conduction subband. The results are shown in Figure 4.7(b).



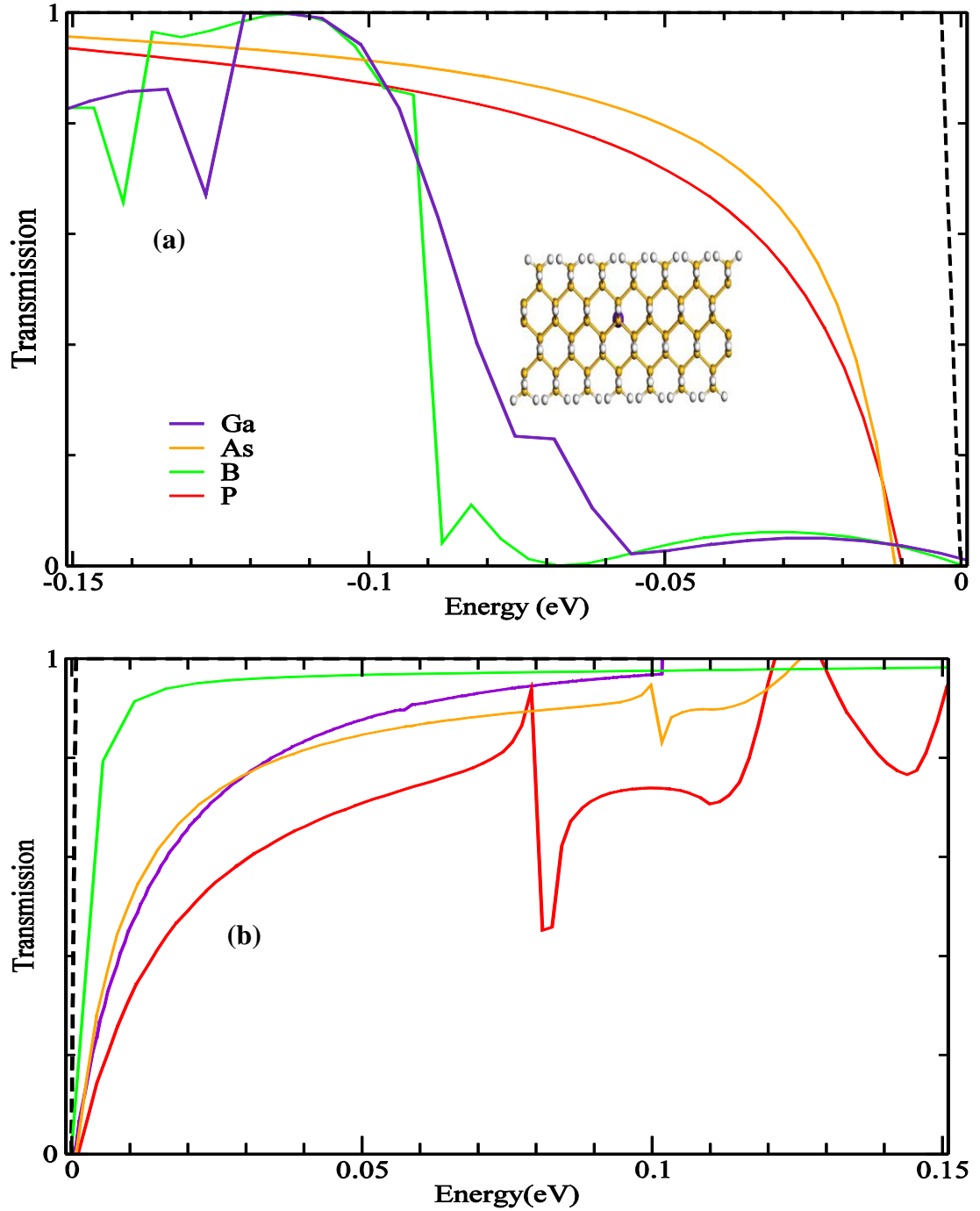


**Figure 4.7:** Transmission function across <110>-oriented SiNWs with 1.15 nm diameter and doped with single substitutional dopants as indicated. All calculations are performed using optimised double zeta basis sets. Results are shown for the first valence band in (a) and conduction band in (b). Energies are referenced to band extrema. The black dash line indicates transmission of ideal wire.

The features observed in the transmission function affect the mean free path  $\lambda(E)$ . Using the approximation of scattering from independent atoms, this can be readily estimated from the transmission curves of nanowires with a single impurity. The relation holds  $\lambda(E) = \frac{T_s(E)}{N_{ch} - T_s(E)} * l_d$ , where  $T_s$  is the transmission value across the wire with the dopant impurity,  $N_{ch}$  is the number of channel eigenstates as defined in section 2.3.1, and  $l_d$  is the mean distance between defects. We provide below a brief derivation of this relation.

In the diffusive regime the transmission  $T$  is given by

$$T = N_{ch} \cdot \frac{\lambda}{L} \quad \mathbf{4.1}$$

which by inverting and multiplying by  $\frac{h}{2e^2}$  gives

$$R = R_C \cdot \frac{L}{\lambda} \quad \mathbf{4.2}$$

Here,  $L$  is the length of the conductor/sample,  $\lambda$  is the mean free path, and  $R_C$  is the contact resistance.<sup>155</sup> If impurities are considered as classical resistances added in series then the total resistance is the contact resistance plus the resistance from all the impurities in the sample

$$R = R_C + R_S \cdot \frac{L}{l_d} \quad \mathbf{4.3}$$

where  $R_S$  is the resistance of a single impurity. For long conductors, i.e., where the diffusive regime has been established, the impurity scattering contribution will dominate over  $R_C$ . This yields

$$R = R_S \cdot \frac{L}{l_d} \quad \mathbf{4.4}$$

From Equations 4.2 and 4.4

$$\lambda(E) = \frac{R_C(E)}{R_S(E)} \cdot l_d \quad 4.5$$

The resistance of a single impurity can be obtained by subtracting from the resistance of a sample with a single impurity the contact resistance, that is,

$$R_S(E) = \frac{h}{2e^2} \cdot \left( \frac{1}{T_S} - \frac{1}{N} \right) = \frac{h}{2e^2} \cdot \left( \frac{N-T_S}{N \cdot T_S} \right) \quad 4.6$$

Substitution of 4.6 in 4.5 yields the used formula for the calculation of the mean free path. We note that  $R_S \rightarrow 0$  then  $N - T_S \rightarrow 0$  which gives an infinite mean free path as expected.

Here, we assume a doping density of  $2.5 \cdot 10^{19} \text{cm}^{-3}$  which gives  $l_d = 19.2 \text{ nm}$ . This dopant concentration is typical in the setup of junctionless nanowire transistors. Results are shown in Figure 4.8. Evidently, the mean free path depends on the type of dopant. For weak scatterers of charge-carriers in the valence (conduction) band, that is P and As (B and Ga), the mean free path can be orders of magnitude larger than the sub-10 nm lengths envisioned in ultrascaled junctioned transistors. Together with other investigations<sup>69,76</sup> this implies that long-range roughness may be the dominant scattering mechanism in these devices. However, strong scattering by the B and Ga atoms (P and As) near the valence (conduction) band edge has a significant effect in the reduction of the on-current in junctionless transistors as observed experimentally.<sup>55</sup>

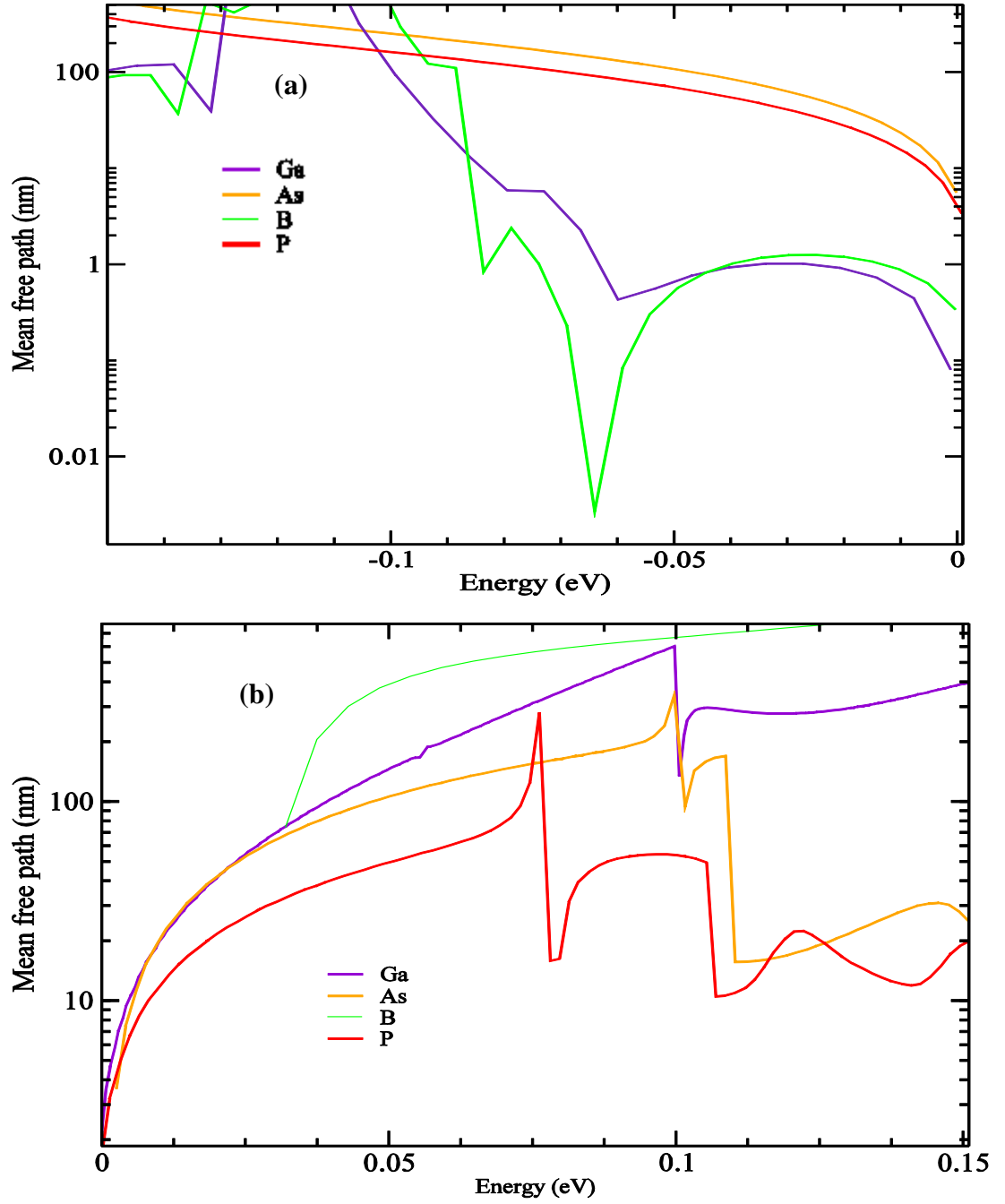


**Figure 4.8:** Mean free path of <110>-oriented SiNWs with 1.15 nm diameter and doped with single substitutional dopants as indicated. All calculations are performed using optimised double zeta basis sets. Results are shown for the first valence band in (a) and conduction band in (b). Energies are referenced to band extrema. The distance between impurities is assumed to be 19.2 nm and corresponds to doping density  $2.5 \times 10^{19} \text{ cm}^{-3}$ .

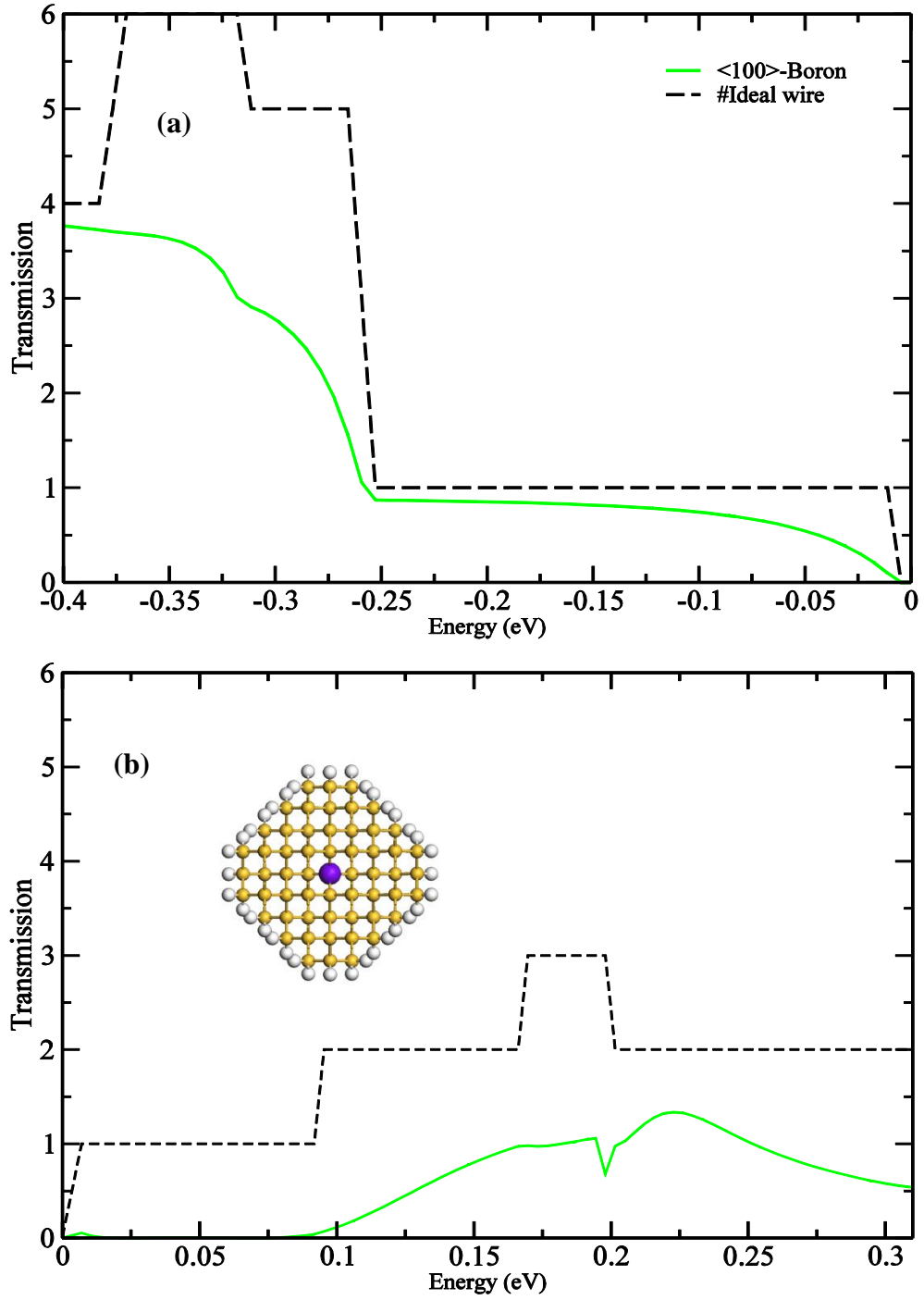


**Figure 4.9:** Transmission function across <100>-oriented SiNWs with 1.27 nm diameter and with single substitutional boron impurity as indicated. All calculations are performed using optimised double zeta basis sets. Results are shown for the valence subbands in (a) and conduction subbands in (b). Energies are referenced to band extrema.

For completeness, in Figure 4.9 the transmission of  $\langle 100 \rangle$  oriented SiNW with diameter 1.27 nm across a single boron impurity substituting a Si atom in the centre is presented. In this case boron acts as a weak scatterer in the valence band whereas strong scattering is observed in the conduction band. This indicates that for small diameter nanowires the scattering properties of dopant impurities depend strongly on the wire-axis orientation.

## 4.4 Conclusions

In summary, the implementation of numerical atomic basis sets by studying the total energy and electronic bands of silicon nanowires with hydrogen surface terminations and doped with B, P, As and Ga atoms is evaluated. It has been shown that there is systematic improvement with respect to the expansion and contraction scheme. Whilst total energies may converge with increasing basis size, optimised NAOs offer a better option to study the electronic properties of SiNWs with fixed basis size. In particular, the optimised double-zeta polarized basis set offers a reasonable approximation. It was also shown that there is some transferability of optimised NAOs which can be used to address nanowire calculations in more complex (larger) environments. These results complement the results of Chapter 3. The scattering properties of n- and p-type dopants is also examined. Fixing the impurity position and the diameter, it is found that in nanowires with a small cross-section both the dopant type and the wire axis orientation play a significant role in determining the transport properties.

## Chapter 5: Basis set dependence of transport properties and electrical device characteristics in Si nanowire setups

### 5.1 Chapter introduction

The continuous miniaturization of electronic transistors pursued by semiconductor industries enables more functionality for fixed die area. However, scaling devices to sub-deca nanometer gives rise to short-channel and quantum tunneling effects that degrade device performance<sup>21,130</sup> and to keep up with scaling research has motivated new transistors designs that use a range of nanostructured materials.<sup>9,21,55,131</sup> These types of devices require taking explicitly into account new physical phenomena and materials properties at the nanoscale. For example, strong quantum confinement in one- and two-dimensions occurs respectively in ultrathin body and nanowire-based FETs<sup>9,26,82,132</sup> and the high surface to volume ratio allows for the manifestation of size effects<sup>65,82</sup> and body inversion.<sup>21,133-135</sup> Direct source-drain quantum mechanical tunneling<sup>84,131</sup> and gate-tunneling leakage arise,<sup>55,83,84,133</sup> obstructing the way to reducing power consumption<sup>15,21,55,136</sup>. Manifestations of differing properties of nanoscale materials compared to their bulk counterparts have also been demonstrated. For the prototypical material of silicon nanowires, surface functionalization schemes result in tuning the electronic and transport properties,<sup>76,137</sup> the effective masses of charge carriers become heavier,<sup>80</sup> dopants may deactivate,<sup>138</sup> and the deformation potentials and electron-phonon scattering can become highly anisotropic.<sup>69</sup> Various semi-classical methods have been elaborated to simulate the current-voltage of conventional transistors and are commonly used to reduce costs and shorten the design cycle.<sup>55,83,141</sup> The need to develop such *a priori* technology evaluation that extends to the nanoscale is recognizably significant as the traditional trial-and-error

experimental design of nanodevices becomes even more time consuming and expensive. Over the last decade the description of electronic quantum transport based on computational methods has become one of the core topics in atomic-scale modelling and device simulations<sup>9,21,55,142</sup> and the explicit electronic structure of materials has been considered from approximate methods that use empirical bulk parameterization<sup>143,144</sup> to first-principles approaches<sup>92,118,121</sup> and approximations thereof.<sup>76,83</sup>

Theoretical studies based on first-principles DFT is one of the widely used methods to describe accurately the atomic geometry and to provide materials design guidelines in an affordable computational time without introducing system dependent parameters. In Chapter 3, numerical atomics orbitals are benchmarked with plane waves basis sets and discussed the impact of basis set on the electronic properties of SiNWs. PWs provide extremely accurate calculations and simple to converge, however computational requirements have limited their use in studies of quantum transport. On the other hand, basis sets made of atomic orbitals (AOs) can be more efficient and their implementation for large-scale order-N calculations is highly motivated.<sup>99</sup> There have been numerous studies of AO implementations on the structural properties and electronic spectra of various systems including my own work on SiNWs as discussed in Chapters 3 and 4. Surprisingly, with few exceptions a similar elaboration on transport properties has attracted little attention despite the need to reach the same level of confidence for device design and evaluation.

Strange *et al.* performed benchmark calculations of the transmission spectrum for a set of five single-molecule junctions.<sup>95</sup> Using a Wannier transformation on DFT Hamiltonians in the PW basis sets enabled them to calculate the transmission



function and to compare with a NAOs implementation. They concluded that a double zeta polarized basis sets suffices for the particular systems. This confirmed earlier work by Bauschlicher *et al.* on the gold-benzene-1,4-dithiol-gold junction.<sup>145</sup> In Ref. 94 Driscoll and Varga study the dependence of quantum conductance on basis sets by comparing localized basis sets with extended non-localized polarized basis. They find that convergence with localized basis sets is more demanding due to sensitivity in describing the self consistent potential. Hermann *et al.* also identify issues with the use of large non-orthogonal Gaussian-type AOs.<sup>146</sup> They show that basis sets of triple-zeta quality or higher sometimes result in an artificially high transmission. These results imply that despite the extensive study of convergence properties of AOs in quantum chemistry for decades<sup>103,104</sup> it is necessary to check the transferability of tabulated AOs as well as the construction of NAOs in different chemical environments for *a priori* evaluation of nanoscale devices.

In this chapter, the TiMeS modularity is used to interface with a full flavor DFT package based on numerical atomic orbitals as described previously (see Section 2.5.3). Its flexibility is demonstrated by applying it to study the basis set dependence of the mean free path in silicon nanowires with dopant and surface oxygen impurities and the current-voltage characteristics of ultrascaled nanowire devices. These calculations are based on Hamiltonian matrix descriptions with varying NAO expansions as obtained from OpenMX and combining with Green's functions methods to calculate the quantum-mechanical scattering matrix (see S-matrix in Section 2.3.2). Charge self-consistency in the presence of applied voltages is treated within the non-equilibrium Green's functions framework as discussed in Section 2.3.3.

The structure of this chapter is as follows. In Section 5.2 some preliminaries regarding the computations are provided which are used to obtain the results present in Sections 5.3 and 5.4. In Section 5.3, TiMeS is applied to the calculation of the mean free path and the basis set convergence for silicon nanowires with dopant and surface oxygen impurities is established. Optimized double zeta polarized basis sets give a reasonable compromise between converged results and efficiency. The current-voltage characteristics of ultrascaled (3 nm long) nanowire-based transistors with p-i-p and p-n-p doping profiles is investigated in Section 5.4. The quantitative interplay between basis set dependence and charge self-consistency is analyzed and it is found that the latter has a more profound effect on the device characteristics. Interestingly, these devices yield relatively large source-drain tunneling (currents of the order of 0.5 nA and 2 nA for the p-n-p and p-i-p junctions, respectively) which can have a detrimental effect in the device performance.

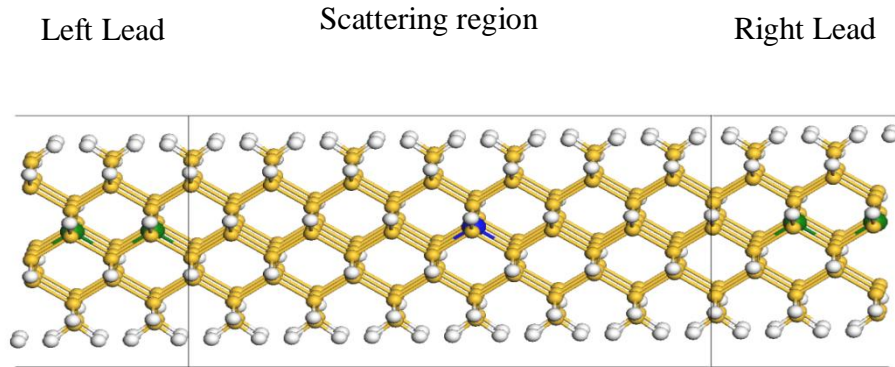


**Figure 5.1:** Schematic setup of one of the investigated nanowire structures. A silicon nanowire grown along the  $\langle 110 \rangle$  direction is depicted with p-n-p doping profile. Substitutional boron (green sphere) is used to dope the semi-infinite periodic leads whereas the “scattering region” incorporates a phosphorus dopant (blue sphere).

## 5.2 Computational details

Throughout the simulations the PBE generalized gradient approximation (GGA) to the exchange correlation potential was used together with norm-conserving pseudopotentials. The focus is on hydrogenated silicon nanowires grown along the  $\langle 110 \rangle$  crystallographic direction with lattice constant of 3.84 Å and diameter equal to 1.15 nm. Impurities are introduced in the supercell by either substitution of silicon atoms in the pristine structure with dopants (see Figure 5.1) or changing the surface termination and introducing oxygen defects for the model described in Ref. 76 (see inset of Figure 5.2). The structures were geometry optimized with force threshold of 0.01 eV/Å and using optimized double zeta polarized basis set (s32p32d1) for both silicon and impurity atoms. Surface-passivating hydrogens are treated in the minimal basis set. Total energy calculations using these bases are well converged as shown previously.<sup>147</sup> The supercell consisted of eleven unit cells and its size extended by 42.24 Å x 25 Å x 25 Å to introduce sufficient vacuum separation between periodic images of the nanowires. In the presence of an applied gate bias in the FET setup the supercell was extended to 17 unit cells, that is 65.28 Å x 25 Å x 25 Å, to ensure a proper redistribution of charges in non-equilibrium. Monkhorst-Pack k-point sampling was applied on a 4x1x1 grid along the nanowire axis. As mentioned in Chapter 2, the TiMeS transport module requires only a single particle Hamiltonian of the relaxed structures of the studied system expressed in a localised basis set which in the present work is obtained from OpenMX.

### 5.3 Transport properties

The impact of numerical atomic orbitals in materials transport properties focusing on charge carrier scattering in SiNWs with common impurities is discussed. The example of Ref. 76 is taken as initial system of reference, where there is a detailed discussion on the scattering behavior due to oxygen defects varying the oxidation state of the Si surface. In this model the surface Si atom is locally oxidized to the formally  $\text{Si}^{2+}$  state by forming a Si-O-Si back bond and using a hydroxyl instead of hydrogen for passivating the surface dangling bond (see inset of Figure 5.1). The presence of the oxygen defect is the origin for surface roughness at the atomic scale.

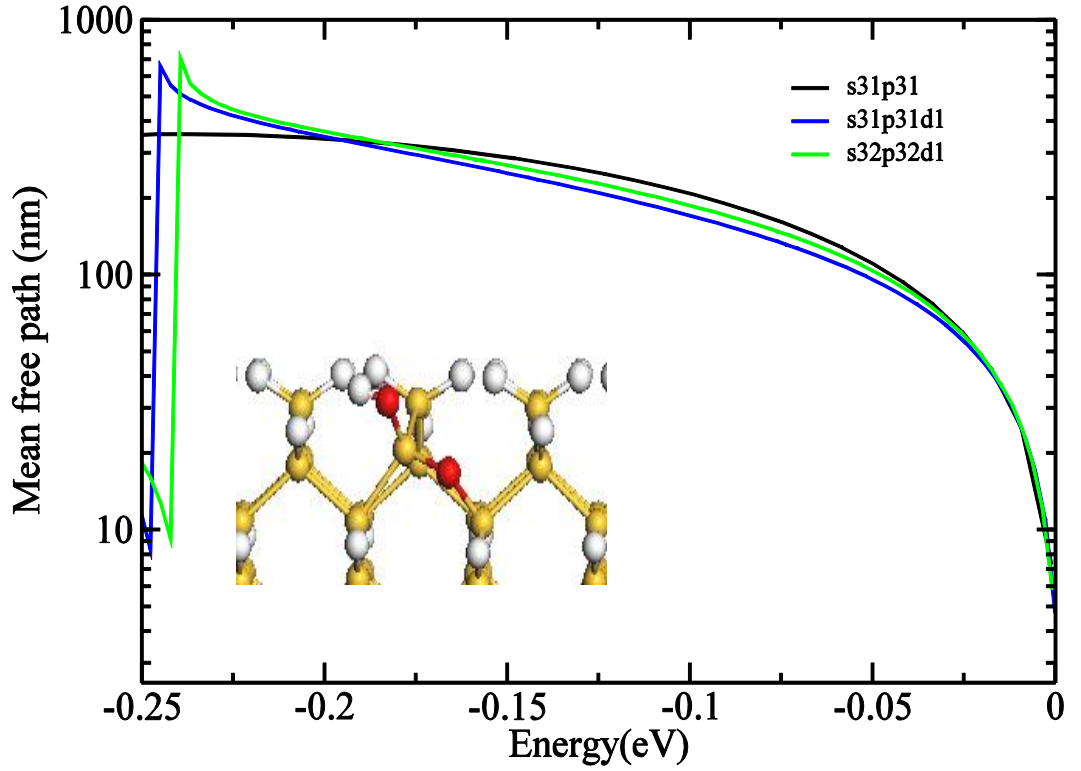


**Figure 5.2:** Mean free path of locally oxidized Si nanowire (structure described in text) for the indicated basis sets and defect density  $n = 5 * 10^{-19} \text{cm}^{-3}$  (mean distance impurities  $l_d = 9.6 \text{ nm}$ ). The energy range corresponds to the first valence sub-band of the electronic structure obtained with the double-zeta polarized basis set.

Following the method in Ref. 76, the mean free path for electrons injected at energy  $E$  is estimated from  $\lambda(E) = \frac{T_s(E)}{T_c(E)} \cdot l_d$ , where  $T_s$  and  $T_c$  are the transmission values across the wire with and without local oxidation and  $l_d$  the mean distance between defects. The mean free path in the energy range of the first valence sub-band is shown in Figure 5.2 for various basis sets, namely, single-zeta, single-zeta polarized and double-zeta polarized. Here,  $l_d = 9.6 \text{ nm}$  which corresponds to a defect density  $n = 5 \times 10^{19} \text{ cm}^{-3}$ . There is overall good agreement with Ref. 76 where a minimal basis set was used within the Density Functional Tight Binding approximation. Interestingly, the mean free path obtained from the various basis sets shows variation of just up to 0.01% using the double-zeta polarized results as a base within an energy range of 0.2 eV.

The above transport results confirm the weak dependence of  $\lambda$  on the basis set when the prevalent scattering mechanism is non-resonant scattering which is regularly observed for typical dopant impurities,<sup>146</sup> surface functionalizations,<sup>73</sup> and oxidation defects.<sup>76</sup> Using a simple analysis based on band structures, previous predictions attribute the mean free path variations to small changes in the group velocity.<sup>145</sup> It may be expected that differing group velocity and effective mass will have most significant impact in the transport coefficients when different electronic structures are used, hence, the need to calibrate to the experiment is introduced.

To consider the case of strong scattering, the common example of a boron substitutional impurity which could act as a  $p$ -type dopant<sup>147</sup> is studied. The transmission of holes injected at energies within the first-valence sub-band is plotted in Figure 5.3. Calculations using single-zeta, single-zeta polarized, double-zeta polarized and triple-zeta polarized bases are shown. There is overall qualitative

agreement between the various sets notwithstanding the evident resonant backscattering that strongly suppresses transmission near the top of the first valence subband and just below -0.125 eV. However, the quantitative discrepancy may lead to significant overestimations of the nanowire conductivity. Similar results are obtained for an n-type dopant impurity, namely, substitutional phosphorus. This behaviour is similar to conductance estimations in transport across molecular junctions where convergence needs to be ensured by enlarging the size of the basis set.<sup>145</sup> It is evident from Figure 5.3 that using the basis set with double-zeta and polarization closely tracks the result obtained with triple-zeta polarized basis. This would provide a good compromise between size and accuracy in the application of atomic basis sets to predict from first-principles the characteristic transport lengthscales and intrinsic transport properties in materials.

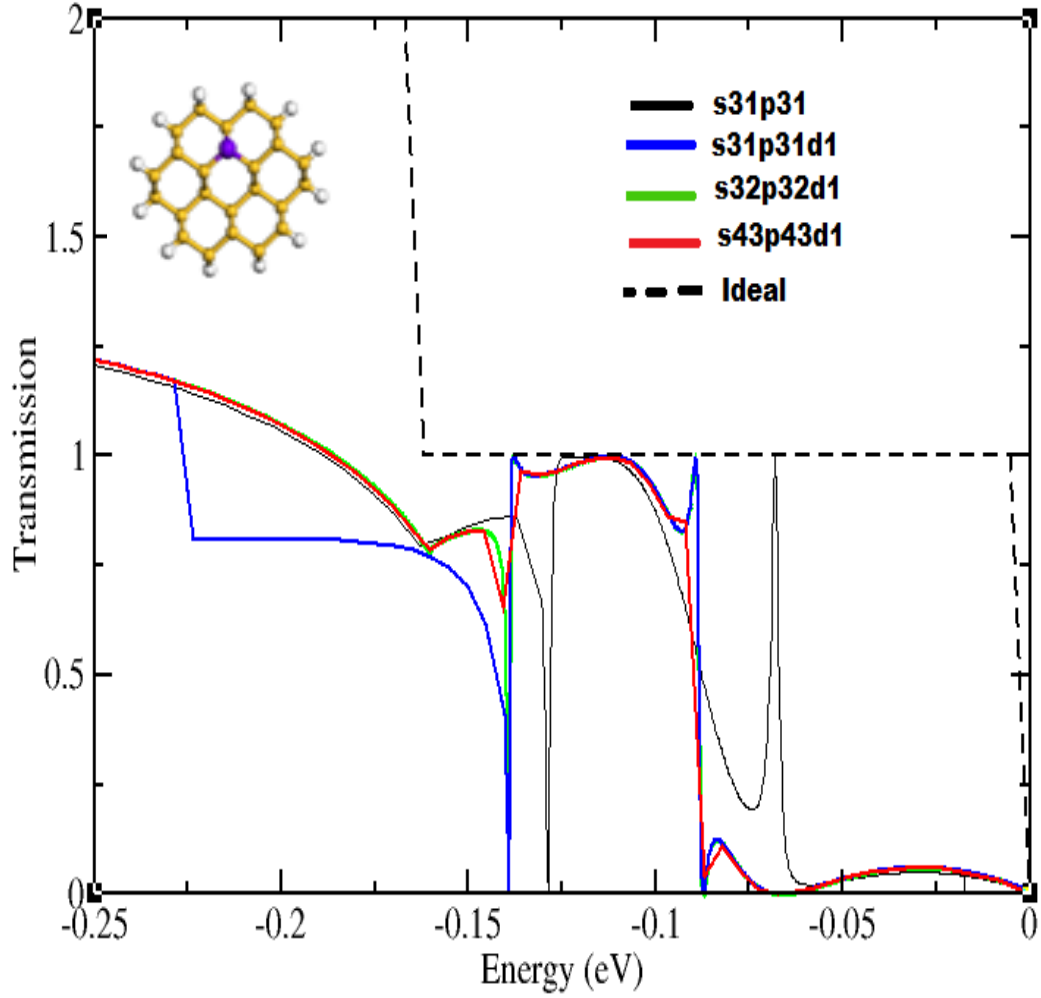


**Figure 5.3:** Transmission of holes across a silicon nanowire with boron impurity (structure described in text) for the indicated basis sets. The energy range corresponds to the first valence sub-band of the electronic structure obtained with the double-zeta polarised basis set <110>.

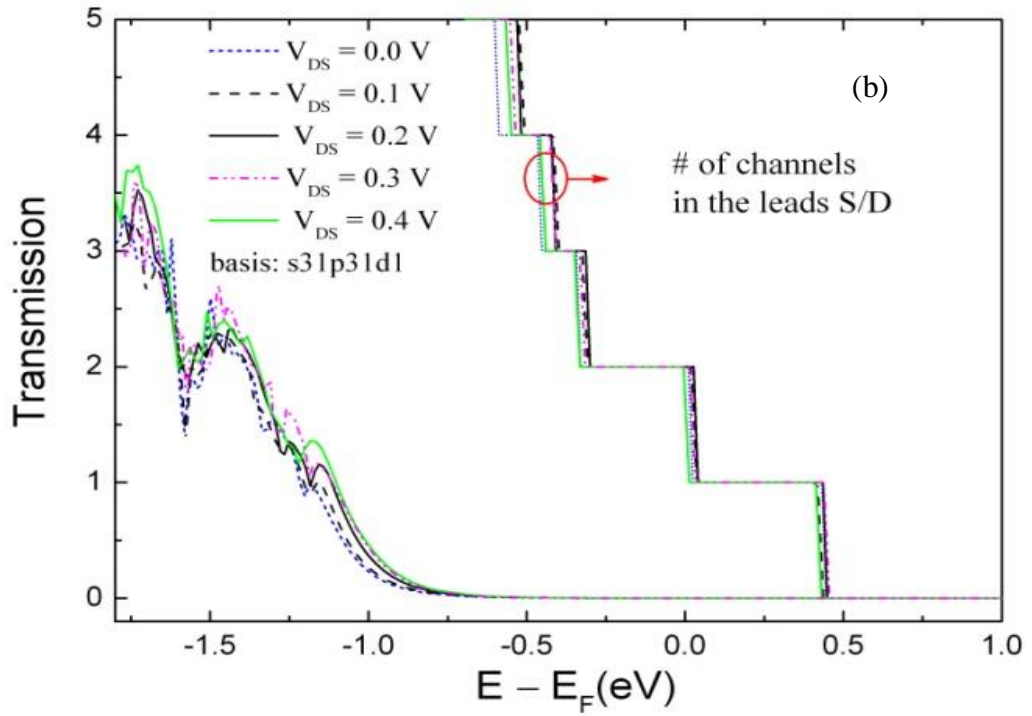
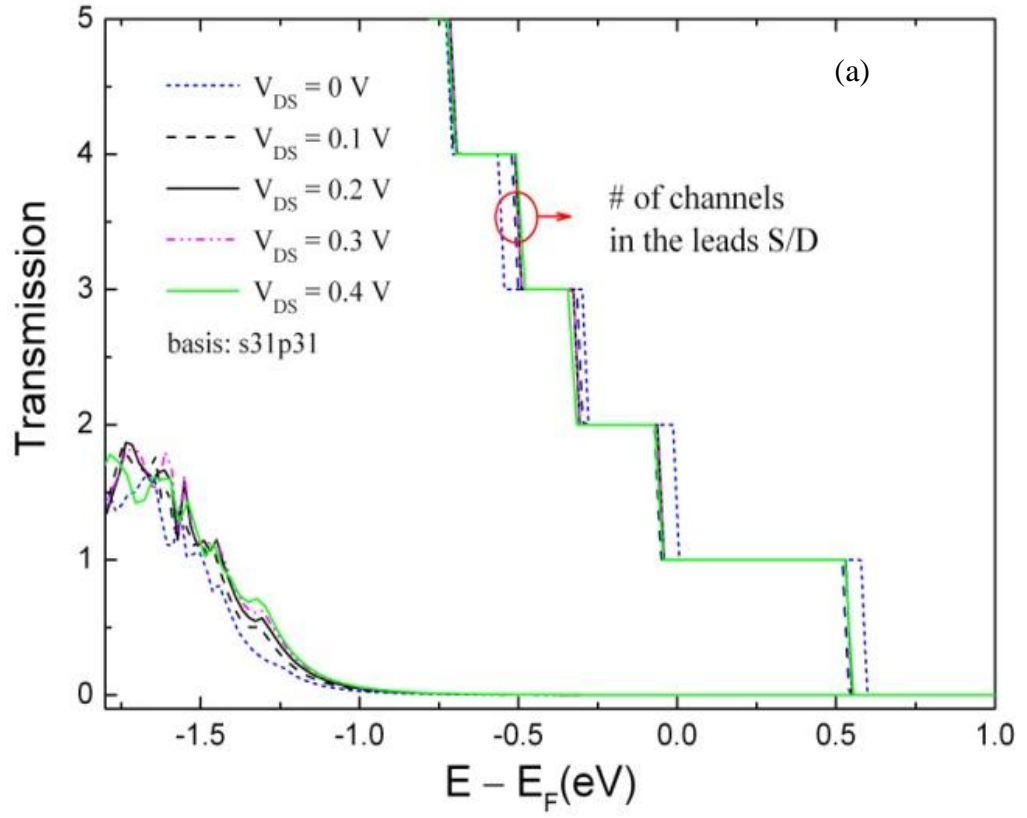
## 5.4 Electrical characteristics

Applying the electronic transmission methodology, in this section the electrical characteristics of SiNW based p-n-p and p-i-p junctions will be explored. The p-n-p junction is constructed from boron doped leads with an n-type scattering region between the two p-type leads (see Figure 5.1). The scattering region is made by introducing one phosphorus dopant in the nanowire lattice. For the p-i-p junctions,

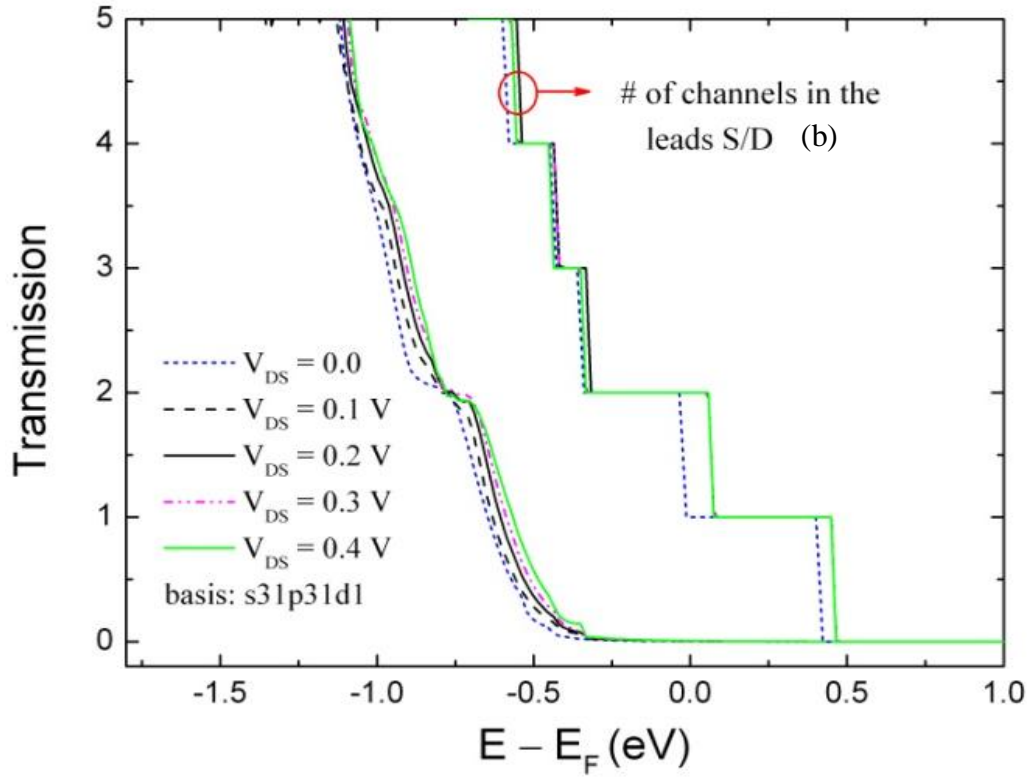
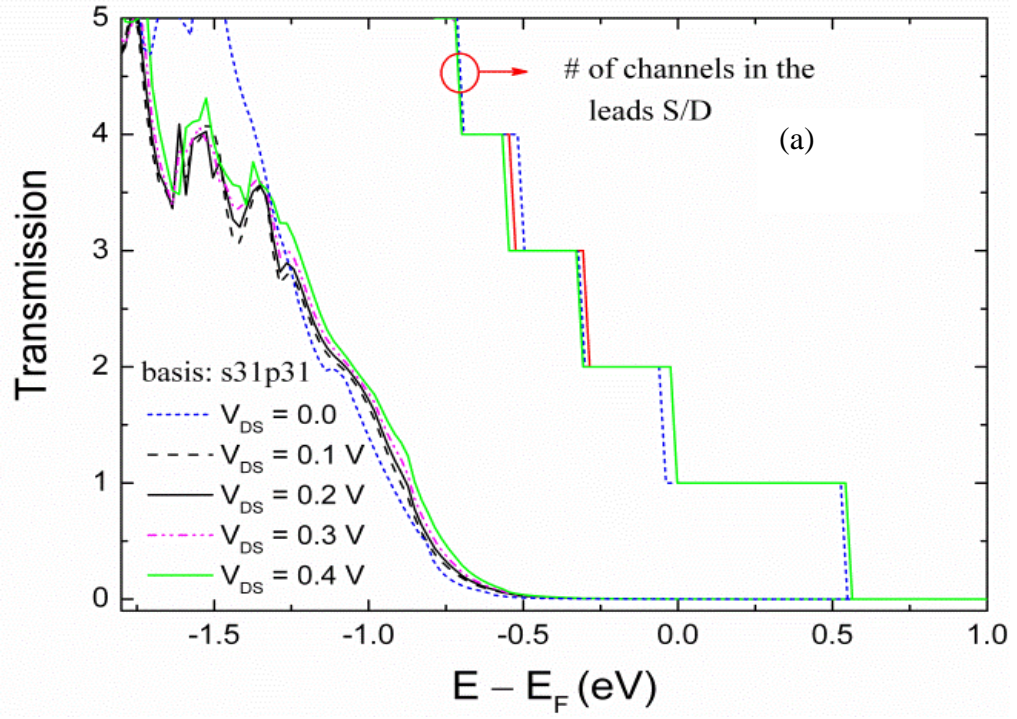
the scattering region is intrinsic. The total length of the scattering region is 2.7 nm. In the GAA setup of a nanowire-based FET this is surrounded by the cylindrical gate, thereby forming the transistor channel. Given that the localization radius of dopant impurity states is approximately 1.5 nm and that the channel length should be at least two times larger than the nanowire diameter for effective electrostatic gating<sup>83</sup>, these are model structures for the smallest junctioned nanowire transistors.

Figure 5.4 and Figure 5.5 illustrates the transmission properties of the p-n-p and p-i-p SiNW junctions at different source-drain bias voltages, applied along the nanowire axis, as predicted from different orbital basis sets. The results are obtained using the two different transport algorithms which have already been described in Section 2.5.3. As expected, Figure 5.4 and Figure 5.5 shows that at small source-drain bias voltages the self-consistent converged transmission  $T(E, V_{DS})$  does not differ from the linear-response approximation  $T(E)$  considerably. However, for larger bias applying the NEGF self-consistence loop increases the transmission for all basis sets used. It is apparent that the addition of d-polarization functions does not change significantly the dependence of transmission on the applied voltage. The main effect of the larger basis is on the electronic structure alignment of the scattering region with the available channels of the leads as seen by the comparison of the transmission between minimal and polarized basis sets.





**Figure 5.4:** Transmission properties of p-n-p junctions using (a) s31p31 and (b) s31p31d1 basis sets. The Fermi level is the reference energy.



**Figure 5.5:** Transmission of the p-i-p junctions considering (a) s31p31 and (b) s31p31d1 orbital basis sets, respectively. The Fermi level is the reference energy.

The current-voltage (I-V) characteristics of p-n-p and p-i-p junctions based on  $T(E, V_{DS})$  and  $T(E)$  are plotted in Figures 5.6 (a) and (b), respectively. The I-V characteristics using the double-zeta polarized basis set and without self-consistency (based on  $T(E)$ ) is also illustrated in Figure 5.6 for comparison. The minimum orbital basis set (s31p31) predicts higher current flow for both junctions compared to orbital basis sets with polarization (s31p31d1). For example, at  $V_{DS} = 0.4$  V, the p-n-p junction with s31p31 basis set, the current is 0.12 times larger if we consider the current characteristic of s31p31d1 as the reference in the fully self-consistent approach. Also, this figure confirms that the difference between SC and non-SC results is greater at larger bias voltages for both structures, as is intuitively expected.

The currents calculated with the NSC loop are lower than applying the computationally more demanding NEGF method. This is attributed to an overestimation of the polarization effect induced when a bias is applied, whereas, SC allows for the redistribution of charges at non-equilibrium. This is important to take into account when simulating current-voltage characteristics to extract the device performance. Here, this yields an underestimation of the source-drain tunneling current. Elsewhere, we have shown that transistor estimates of switching between off and on states are much worse if self-consistency is disregarded. From Figure 5.4 and Figure 5.5 it is deduced that the potential error is more significant than using a lower quality basis set.

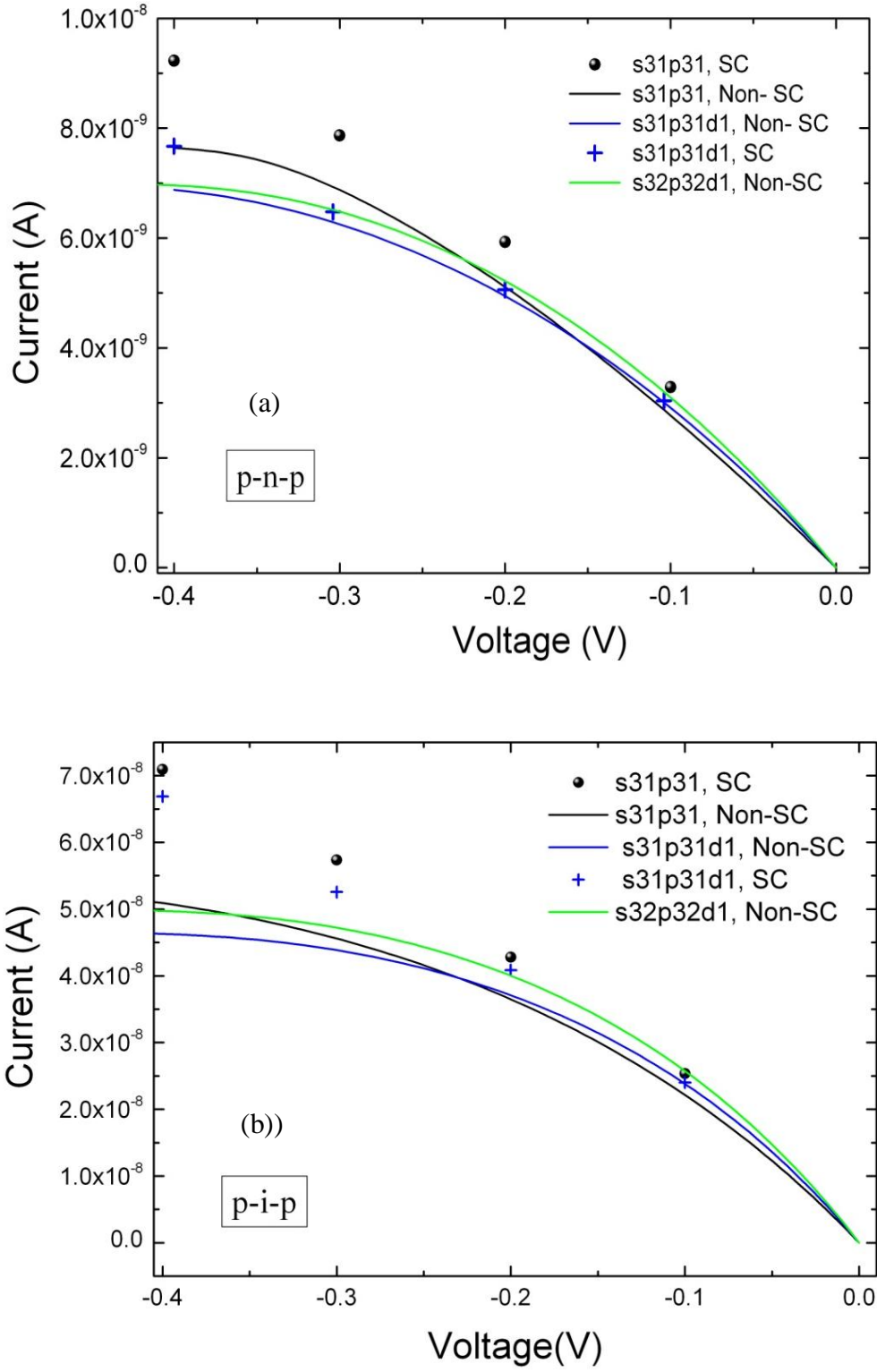


**Figure 5.6:** Current-voltage characteristics of (a) p-n-p and (b) p-i-p junctions. The different orbital basis sets is compared for both structures. The scattering points shows the results based on  $T(E, V_{DS})$  and the lines are corresponding to  $T(E)$ .

The I-V characteristic of the p-i-p junction shows more sensitivity at higher bias voltages compared to the p-n-p junction. The reason is that there is larger scattering for the p-n-p junction due to the larger band offset compared to the p-i-p junction (see Figure 5.4 and Figure 5.5). This corresponds to higher level of available electronic charges in the p-i-p junction yielding higher current level at larger bias. Finally, the source-drain tunneling currents of the devices for the two doping profiles are around 0.5 nA (p-n-p junction) and 2 nA (p-i-p junction). These values are two to four orders of magnitude higher compared to junctionless Si nanowire devices, that is, FETs with homogeneous source-channel-drain doping, of similar channel dimensions and orientation. This suggests that at such scales the distribution of charge carriers around the dopant blurs the boundaries of a junction over a distance comparable to the channel length. Therefore, besides being very difficult to fabricate junctioned FET designs would fail to keep carriers out of the channel.

## 5.5 Conclusions

To summarise, in this chapter the impact of numerical atomic orbitals is evaluated on electron transport properties mainly on charge carrier scattering in  $\langle 110 \rangle$  oriented SiNWs with dopant impurities. The mean free path is weakly dependent on atomic orbitals basis sets for non-resonant scattering. It is found that optimised single-zeta and double-zeta orbitals with d functions reproduce the results with triple-zeta polarised basis thereby giving a reasonable compromise between converged results and efficiency. The current-voltage characteristics of ultrascaled (3 nm length) nanowire-based transistors with p-i-p and p-n-p doping profiles was also investigated. It was found that charge self-consistency affects the device characteristics more significantly than the choice of the basis set. These devices yield source-drain tunneling currents of the order of 0.5 nA and 2 nA for p-n-p junction and p-i-p

junction, respectively which implies that junctioned transistor designs would likely fail to keep carriers out of the channel.

## Chapter 6: Hole mobility in low-doped silicon nanowires

### 6.1 Chapter introduction

Significant control of the semiconducting behaviour of SiNWs can be achieved via doping to tune their electronic and transport properties. The main reason for doping a material is to increase the carrier density. Unintentional doping is also present due to the fabrication process of electronic devices and the prohibitive cost of producing wafers with very low dopant impurity concentrations. As discussed in the introductory Chapter 1 several applications of SiNWs require being able to tune the doping profile; these include solar cells, photodiodes and FETs for sensors and logic gates. Typically boron and phosphorous are used as *p*- and *n*-type dopants respectively but Ga and As have also been used. Common methods to incorporate dopants are during the VLS growth and ion implantation in bottom-up and top-down fabrication respectively.

As seen in Chapter 4 when a dopant is introduced into the silicon lattice it causes scattering of charge carriers. This is due to the new chemical environment (potential) introduced by the dopant which modifies the periodicity of the lattice. In bulk semiconductors there are two sources of scattering from dopant impurities, namely, neutral and ionised impurity scattering. The typical ionisation energy in bulk silicon for various dopants is  $\sim 50$  meV which implies that at room temperature ionised impurity scattering is the dominant mechanism. However, this may not be the case for highly-doped silicon nanowires where the impurity bands strongly overlap with the charge carrier channels.<sup>83</sup> Also quantum confinement and the dielectric mismatch with the surrounding material can significantly increase the ionisation energy in low-

doped silicon nanowires, thereby, making dopants inactive.<sup>138,148</sup> As demonstrated in Chapter 4 neutral impurity scattering can be quite significant in small diameter nanowires and in this case it can act as a limiting factor to the mobility which plays an important role in the device performance such as drive current and speed.

A factor to consider in electronic devices based on SiNWs are sample-to-sample fluctuations since it is expected that as the width of the nanowire decreases the enhanced impurity scattering can depend on the exact number of dopants and their location along the radial direction. Moreover charge carrier mobilities are limited by other scattering mechanisms like surface roughness and phonon scattering which have not been systematically studied. Experimental data have just started to emerge and are difficult to interpret. In early measurements, the mobility of  $\langle 100 \rangle$ - and  $\langle 110 \rangle$ -oriented SiNWs has been estimated by using a capacitance-voltage method<sup>151</sup>. The authors find that both electron and hole mobilities decrease monotonically with nanowire width and that the electron mobilities of nanowires along the  $\langle 100 \rangle$ - and  $\langle 110 \rangle$ -axis are comparable. This contradicts more recent studies. In Ref. 150, it is shown that the  $\langle 110 \rangle$ -orientation yields enhanced mobility in agreement with theoretical results.<sup>151</sup>

In this chapter we are motivated by the results of Ref. 26 where quantum confinement has been studied in  $\langle 110 \rangle$ -channels made of silicon nanowires. The authors perform detailed electrical characterisation in SiNW FETs with sub-5 nm channel width and nominally doped with boron (doping density  $2 \times 10^{15} \text{ cm}^{-3}$ ). They find that the mobility is enhanced due to quantum confinement compared to a nanobelt control sample; hole mobilities in the range of  $400\text{-}1200 \text{ cm}^2/(\text{Vs})$  are reported. The hole mobility in boron-doped  $\langle 110 \rangle$ -oriented Si nanowires with different diameters (1.15 nm-4.47 nm) for various low dopant concentrations and



place the substitutional dopant impurity at different positions in the cross-section to estimate the mobility variations due to neutral impurity scattering is calculated.

The structure of the chapter is as follows. Section 6.2 provides details on the preliminary calculations regarding the electronic structure as well as the scattering properties of single boron impurities as a function of nanowire diameter and dopant position. These calculations are based on first-principles using OpenMX and TiMeS as discussed in previous chapters. In Section 6.3 the results on the hole mobility is discussed. Here, the estimations are based on considering scattering from independent impurities and applying the relaxation time approximation within the Boltzmann transport method.

## **6.2 Electronic structure and transmission properties**

Structural relaxations and electronic structure calculations were performed using the OpenMX code with the GGA-PBE functional and norm conserving pseudopotentials. The structures were geometry optimised with force threshold of  $0.01 \text{ eV/\AA}$ . A Monkhorst-Pack k-point sampling on a  $15 \times 1 \times 1$  grid in the Brillouin zone and an optimised double-zeta polarised basis set were used. In Figure 6.1 (a-d), The band structure of ideal SiNWs surface-passivated with hydrogen and varying width (diameter ranges from 1.15 to 4.47 nm) is plotted. The cross-section of the nanowires is displayed in the insets. The effective mass is calculated from the band structure by taking the second derivative of the first valence band at the gamma  $\Gamma$  point as described in Section 3.3. the results in Table 6.1 is tabulated along with the band gap. The band gap increases with decreasing nanowire width as expected from the stronger quantum confinement and the effective mass increases slightly with the width. These results agree with Refs 82, 154.

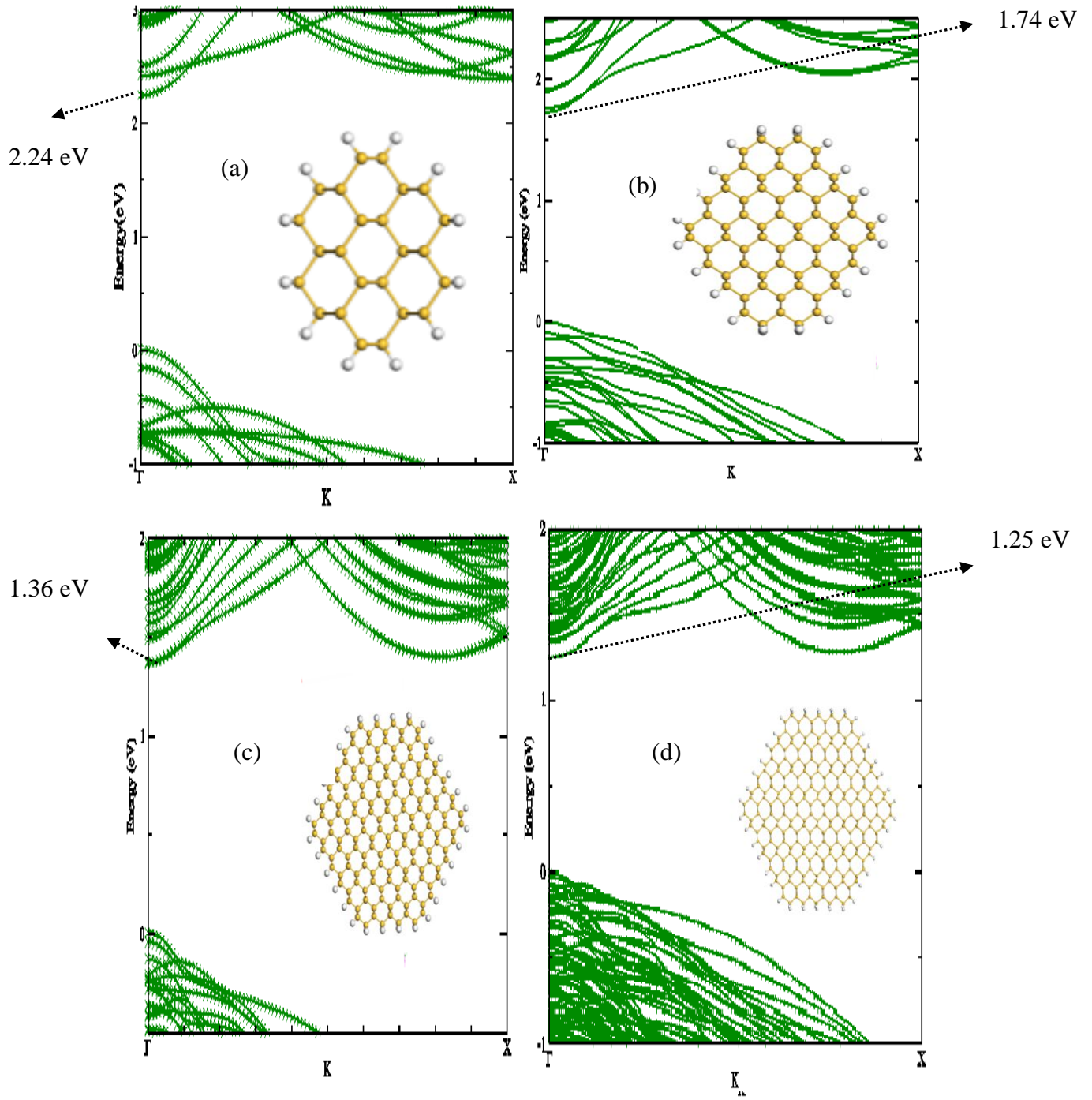


**Figure 6.1:** Band structures of  $\langle 110 \rangle$ -oriented Si nanowires with increasing width (diameter: 1.15 nm, 2.22 nm, 3.34 nm and 4.47 nm). The cross-sections are given as insets. The calculated band gap of bulk Si is 0.96 eV.

**Table 6.1:** Band gap and hole effective mass of <110>-oriented Si nanowires and increasing width.

SiNW diameter (nm)	Band gap (eV)	Effective mass ( $m_e$ ) calculated here
1.15	2.24	0.14
2.24	1.74	0.17
3.34	1.36	0.18
4.47	1.25	0.19

In Ref. 73 it is shown that a dopant substituting a Si atom in the ‘bulk’ body of a nanowire induces stronger back scattering than a surface dopant interacting with a dangling bond, in which case ballistic transport occurs. Here, the effect of dangling bond saturation by dopant impurities but take into account the possibility of dopant substitution in various positions is disregarded. The different distribution of boron substitutional dopants in the cross-section of nanowires with increasing width is shown in Figure 6.2. For the smallest nanowire with width ( $d=1.15$  nm), one position in the silicon body and one at the surface is considered. For the nanowire with diameter of 2.22 nm six different positions are considered – three sites for ‘bulk’ doping and three dopant positions at the surface. Similarly seven and eight different positions for the 3.34 nm and 4.47 nm nanowires respectively are considered. The structures are optimised using a supercell of  $19.2\text{\AA} \times 25\text{\AA} \times 25\text{\AA}$  with the nanowire axis oriented along the x-direction and an optimised double-zeta polarised basis set as before. However, the approximate single-zeta basis set to perform transport calculations within TiMeS is used. Based on the results of chapter 5 this is sufficient for a first qualitative discussion of the effect of dopant position and nanowire diameter on the hole mobilities.

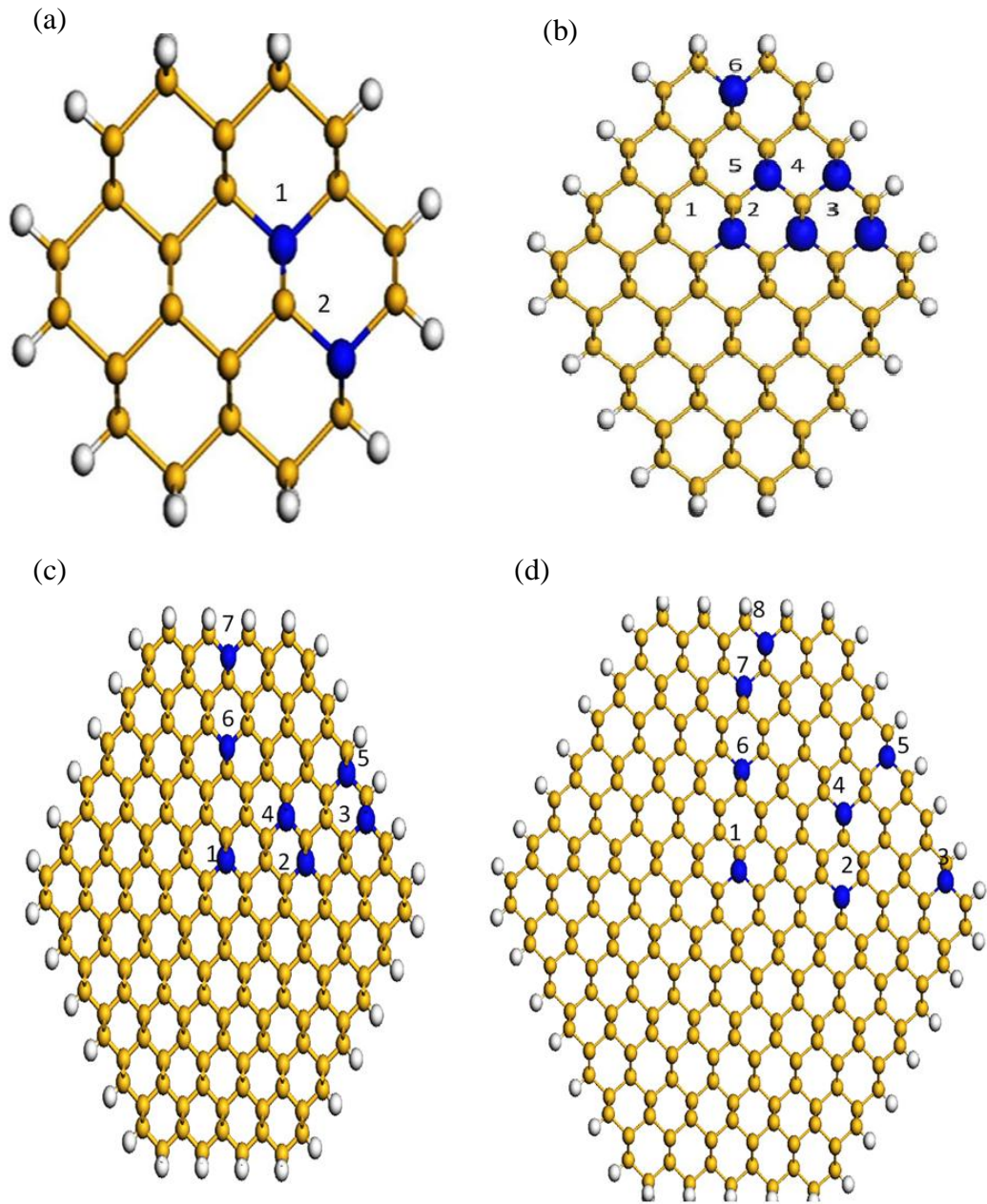


**Figure 6.2:** Cross-sections of the  $\langle 110 \rangle$ -oriented silicon nanowires with boron substitutional impurities. The various positions of the boron atoms are indicated. The diameter of the nanowires of radius (a) 1.15 nm, (b) 2.22 nm, (c) 3.34 nm and (d) 4.47 nm.

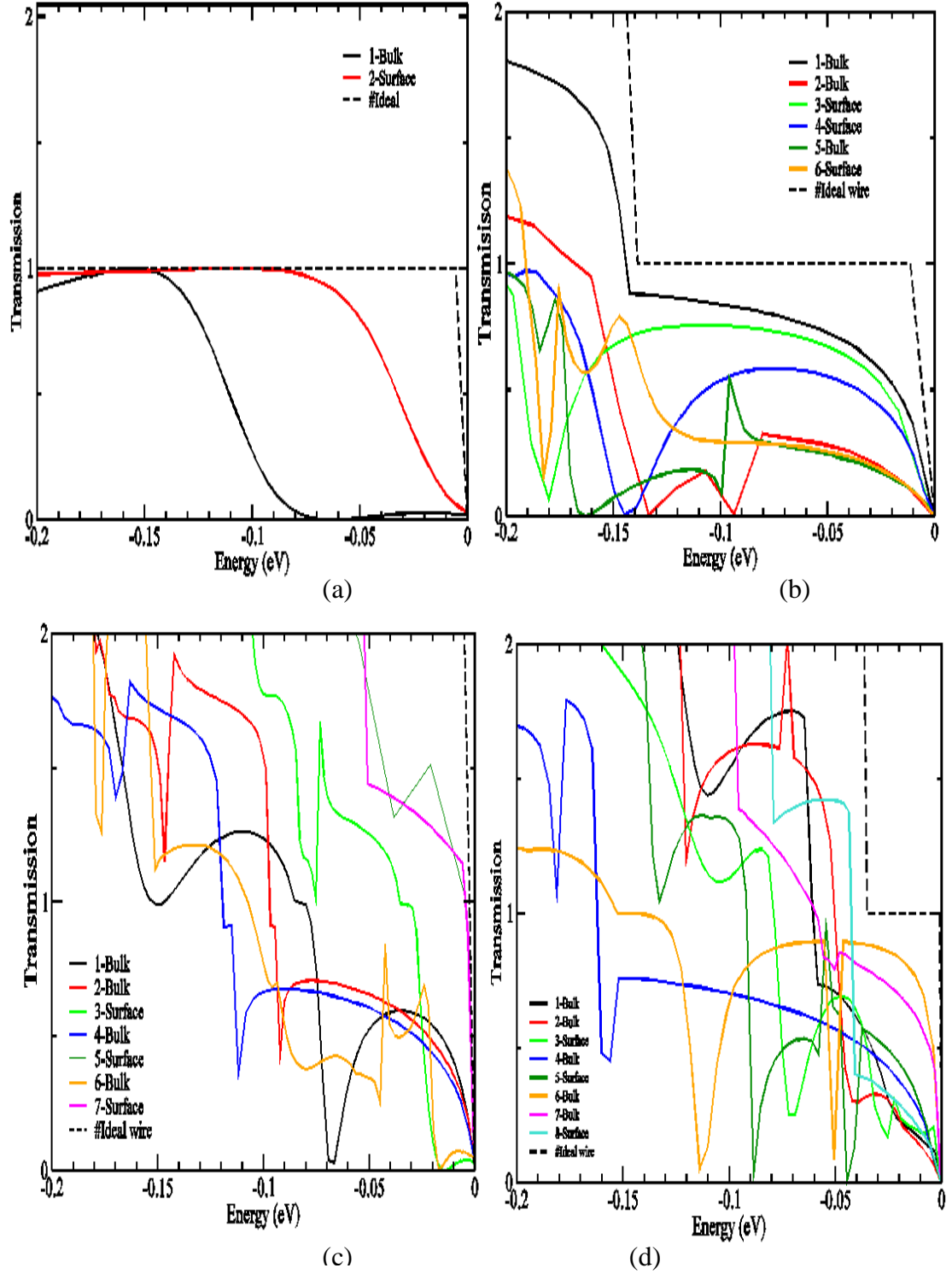


**Figure 6.3:** Transmission at different dopant location of boron doped SiNWs with width versus eigenenergies of valence band edge (a) 1.15 nm (b) 2.2 nm (c) 3.34 nm and (d) 4.47 nm.

The transmission of holes across the considered SiNWs with a single boron impurity is shown in Figure 6.3. For the same dopant position the scattering properties are different with varying nanowire widths. For example, backscattering is observed with the transmission dropping to zero when the boron atom is positioned exactly at the centre (bulk) and the diameter is 1.15 nm but for larger nanowires there is no such strong scattering for this dopant position. For SiNWs with width 2.22 nm and 4.47 nm backscattering is seen for both bulk and surface locations of the dopant atom. However at nanowire with 3.34 nm width back scattering is seen mostly in the bulk site except at position 6 where the dopant is located near the surface. This shows that dopants located at the surface can also act as strong scatterers. These results show that the scattering behaviour is strongly dependent on nanowire width along with dopant location which may explain some of the variations seen in electrical characterisation experiments.

## 6.4 Hole mobility

The mobility  $\mu$  of a semiconductor material can be obtained from the Boltzmann transport equation within relaxation time approximation

$$\mu = \frac{e\langle\tau_m\rangle}{m^*} \quad 6.1$$

where  $e$  the electron charge and  $m^*$  is the effective mass calculated from the band structure of the undoped SiNWs.<sup>157</sup> The average momentum relaxation time  $\langle\tau_m\rangle = \langle\tau_m(v)\rangle$  is

$$\langle\tau_m\rangle = \int_{-\infty}^{\infty} \tau_m(v) \cdot v_x \left(-\frac{\partial f_0}{\partial v_x}\right) d^3v / \int_{-\infty}^{+\infty} f_0(E) d^3v \quad 6.2$$

where the Fermi-Dirac distribution  $f_0(E) = \frac{1}{1 + \exp \frac{(E - E_f)}{k_B T}}$  and the group velocity  $v_x$

is calculated from the first derivative of the bands as described in Section 3.3. For a one dimensional system  $\langle \tau_m \rangle$  the integral of Equation 6.2 can be expressed as a function of energy via the mean free path  $\lambda$

$$\langle \tau_m \rangle = \frac{m^*}{K_B T} \int_0^\infty \lambda(E) \cdot f_0 \cdot (1 - f_0) dE / \int_0^\infty f_0 \frac{1}{v_x} dE \quad 6.3$$

Substituting Equation 6.3 in Equation 6.1 gives the mobility as

$$\mu = \frac{e}{K_B T} \int_0^\infty \lambda(E) \cdot f_0 \cdot (1 - f_0) dE / \int_0^\infty f_0 \frac{1}{v_x} dE \quad 6.4$$

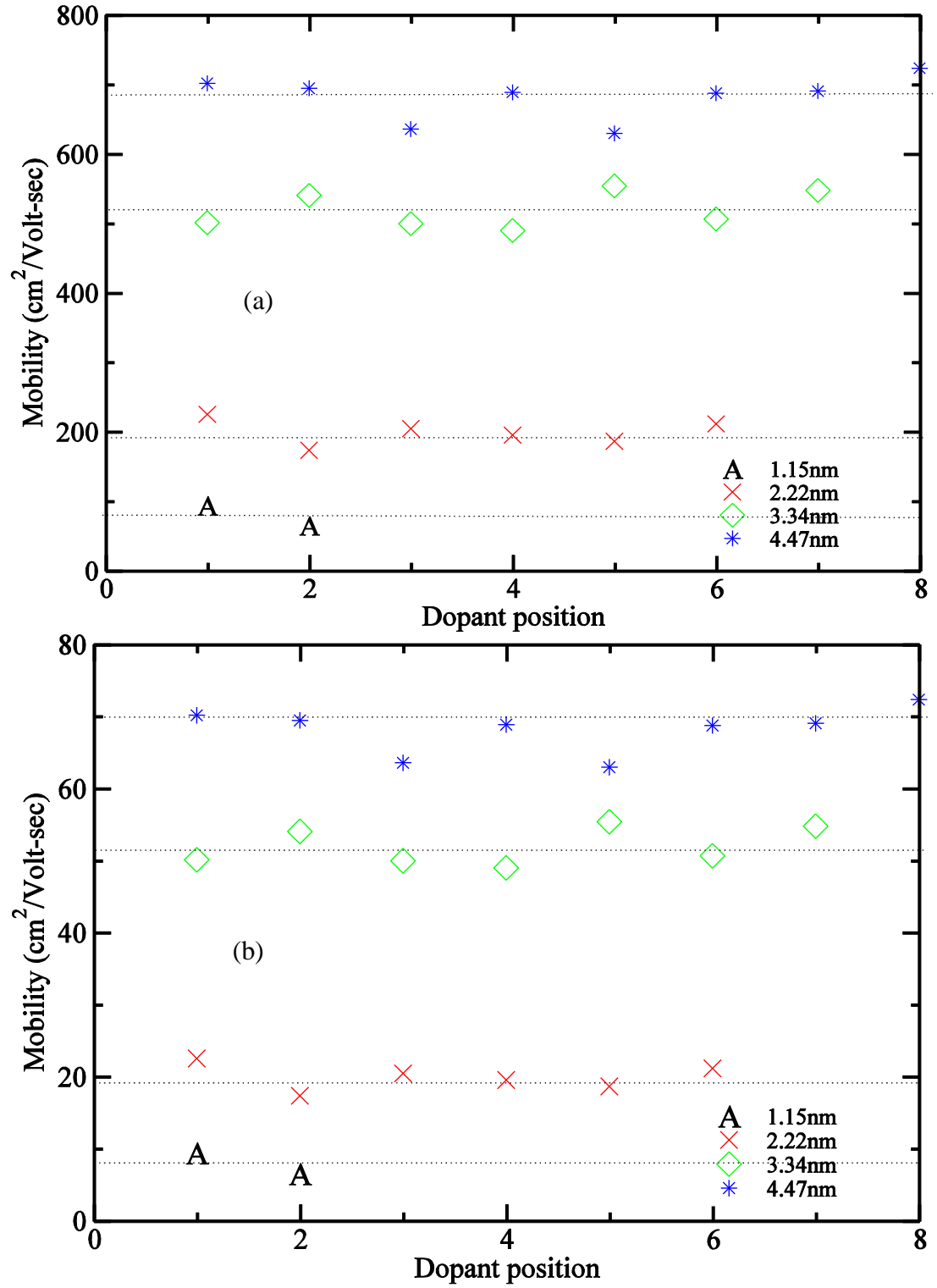
To estimate the mean free path we use the implicit assumption of scattering from independent impurities. As in Chapters 4 and 5, this is calculated via  $\lambda(E) = \frac{T_s(E)}{N_{ch} - T_s(E)} * l_d$ , where  $T_s$  is the transmission value across the wire with the impurity and  $N_{ch}$  the number of modes as defined in Section 2.3.1. These are taken from the calculations in the previous section.  $l_d$  is the mean distance between dopants which for a fixed dopant concentration decreases with increasing width as shown in Table 6.2. Here, low-doped SiNWs with nominal doping density  $\sim 10^{15} \text{ cm}^{-3}$  is assumed.

**Table 6.2:** Estimates of the distance  $l_d$  between dopants for varying (low-)dopant density and nanowire width. This is calculated from  $\pi(\frac{W}{2})^2 \cdot 2l_d \cdot n = 1$  where W is the nanowire diameter and n is the doping concentration.

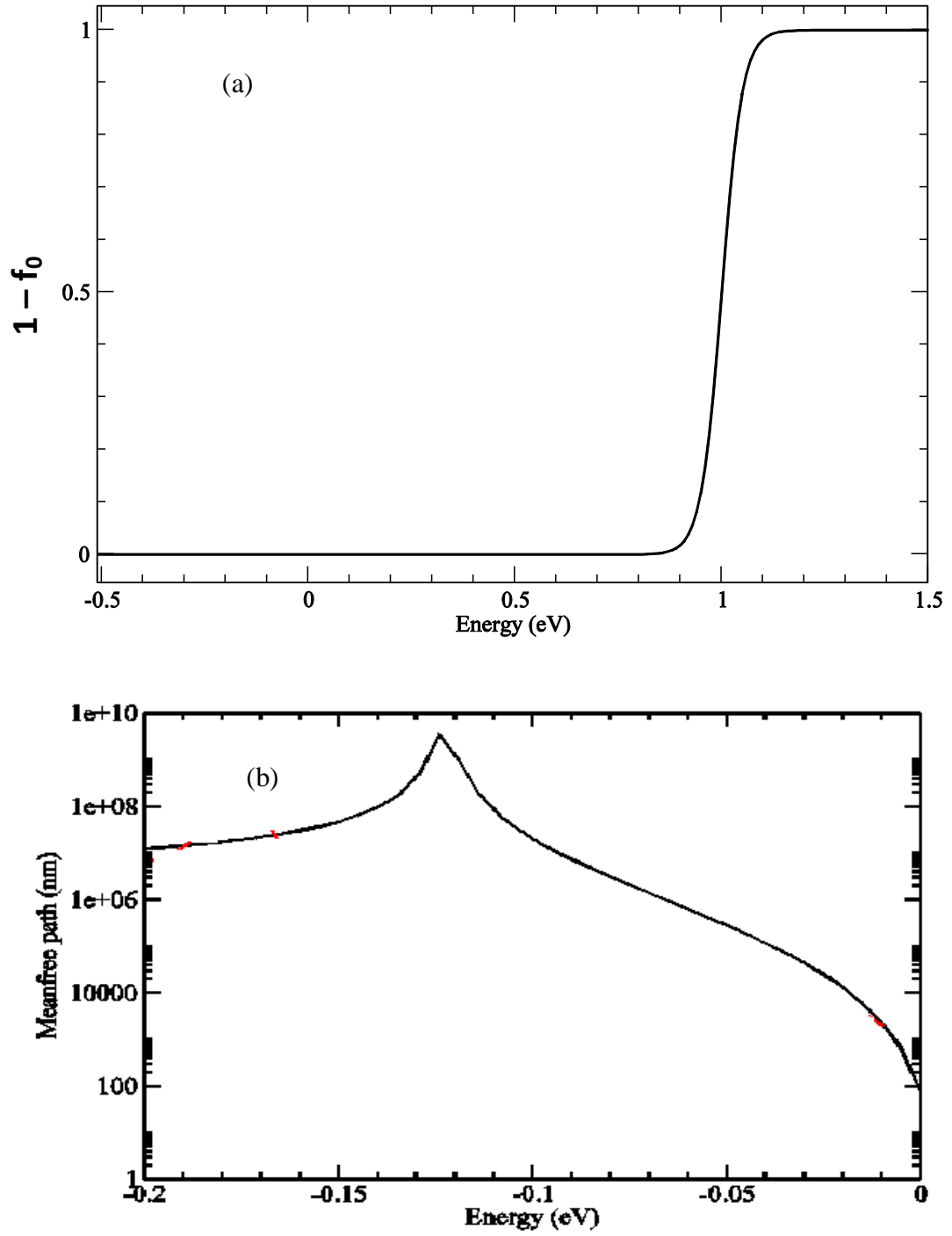
W (nm)	$l_d$ ( $\mu\text{m}$ ) at n $1 * 10^{15} \text{cm}^{-3}$	$l_d$ ( $\mu\text{m}$ ) at n $2 * 10^{15} \text{cm}^{-3}$	$l_d$ ( $\mu\text{m}$ ) at n $3 * 10^{15} \text{cm}^{-3}$	$l_d$ ( $\mu\text{m}$ ) at n $4 * 10^{15} \text{cm}^{-3}$	$l_d$ ( $\mu\text{m}$ ) at n $2 * 10^{16} \text{cm}^{-3}$
1.15	482	241	160	120	24
2.22	129	65	43	32	6
3.34	57	28	19	14	2.8
4.47	32	16	11	8	1.6

Figure 6.5 shows the hole mobilities as a function of diameter and for various dopant positions. Evidently, although mobility variations are observed depending on the dopant position a much weaker dependence than expected is exhibited. This is attributed to the cut-off introduced in the integral of Equation 6.4 by the distribution function, shown in Figure 6.6(a), which suppresses any prominent features observed in the scattering properties much below the top of the valence band (e.g., the mean free path dependence shown in Figure 6.6(b)). At such low-dopant densities, the most significant dependence is observed with respect to increasing nanowire diameter and decreasing doping concentration. In both cases the mobility monotonically increases due to weaker scattering.





**Figure 6.5:** Hole mobility of <110>-oriented SiNWs with diameter as indicated and lightly-doped with boron atoms at various sites (both at surface and bulk). Doping density is (a)  $2 \times 10^{15} \text{ cm}^{-3}$  and (b)  $2 \times 10^{16} \text{ cm}^{-3}$ .



**Figure 6.6:** (a) The statistical distribution function for holes and (b) mean free path of boron doped SiNW with diameter 1.15 nm. Energies have been referenced to the top of the valence (sub-)band.

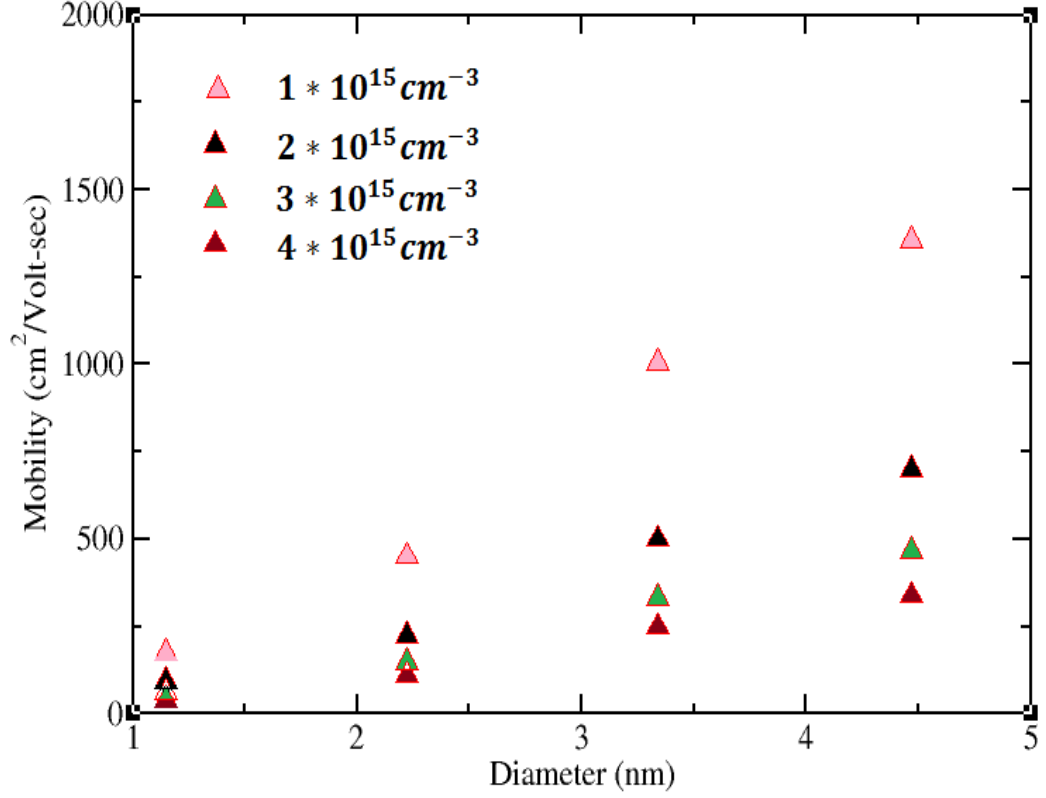


**Figure 6.7:** Hole mobility of <110>-oriented SiNWs with varying width and distance between dopants as indicated in Table 6.2. Doping density is  $\sim 10^{15} \text{ cm}^{-3}$ . Boron substitutional dopants are located in the bulk of the SiNW (referred as location 1 in Figure 6.2).

Comparing the calculated values with those of the experiment at doping density  $2 * 10^{15} \text{ cm}^{-3}$  and nanowire width 4.47 nm,<sup>26</sup> the results show good agreement. They may also explain the observed variations between difference channel lengths and nanowire diameters. Using the distance  $l_d$  between dopants as a parameter that captures the statistical variations between samples, in Figure 6.7 the hole mobility assuming ‘bulk’ boron dopants (position 1 in Figure 6.2) is plotted. It is found that for nanowires with similar width and nominally doped at  $\sim 10^{15} \text{ cm}^{-3}$  the hole mobility shows similar variation as in the experiment, namely, in the range of 340-1360  $\text{cm}^2/(\text{Vs})$  for the nanowire with 4.47 nm width.

## 6.5 Conclusions

In summary the impact of dopant position and nanowire width on the transmission and mobility of SiNWs nominally doped with substitutional boron is evaluated. The scattering properties of single dopant impurities strongly depend on both the nanowire size and dopant location. Backscattering and weak scattering may be observed when a impurity is placed either in the bulk or near the surface. However, despite strong backscattering for many of the dopant positions the hole mobility limited by neutral impurity scattering increases monotonically with increasing nanowire width at fixed doping density. The opposite behaviour is expected with increasing dopant concentration. Most importantly, it is found that the mobility can show significant variations in nominally doped nanowires. For example, at 4.47 nm width and  $n \approx 10^{15} \text{ cm}^{-3}$  the hole mobility is in the range of 340-1360  $\text{cm}^2/(\text{Vs})$  which is in agreement with experimental observations.

## **Chapter 7: Concluding remarks and outlook**

In the second half of 1980s, advances in fabrication and characterisation techniques allowed the fabrication of submicron electronic devices that gave birth to the field of mesoscopic physics and materials band engineering. Using a combination of interfaces and chemical composition, effects such as size quantum confinement, quantum mechanical tunnelling, interference and ballisticity have been observed in electron transport properties and used in applications. In parallel, the study of nanoparticles in chemistry and the detection of fullerenes in 1985 have been placing the foundations for the re-discovery of carbon nanotubes in the early 1990s and the rise of nanomaterials (in particular one-dimensional) as an alternative to scientific and technological advances towards smaller lengthscales. Materials properties as determined not only by the bulk structure and stoichiometry but also by nanostructuring took a central place. With the convergence of these branches towards smaller dimensions along with the needs of microelectronics industry, it has been only a matter of time until semiconductor nanowires (predominantly made of Si but also of Ge and III-V materials) would become one of the most important nanomaterials. In the last decade scientific interest has led to a wealth of discoveries regarding their materials properties as well as to a range of old and new applications in the field of sensing, electronics and energy harvesting and storage. These have unambiguously demonstrated their potential and their wide employment now and in the future.

Notwithstanding a wealth of open issues, atomic-scale modelling and simulations have been very useful in predicting and interpreting experimental results and efforts have focused on developing methods for *a priori* technology evaluation. To this end,

theoretical studies based on first-principles are needed to describe accurately and efficiently the electronic and transport properties of nanomaterials as well as the electrical characteristics of devices. This has been the aim of this thesis. Focusing on SiNWs with diameter less than 5 nm and using density functional theory, my thesis started with a critical examination of the methodology – which has been (and still is) revisited – to enable in the later part a discussion of the possibility to realise certain silicon nanowire devices and an explanation of their transport properties.

Regarding the examination of the methodology, one of the application challenges in DFT is accuracy versus efficiency and implementations of numerical atomic orbitals as basis sets hold great promises. Nevertheless, as it is made quite clear in this thesis this is not straightforward and one has to systematically study their convergence for the particular system of interest. Starting from simple models of SiNWs with hydrogen and hydroxyl terminations the structural and electronic properties with increasing size of NAO basis sets is investigated and for various contraction schemes. These studies to included p- and n-type dopant impurities (that is, B, Ga, P, and As atoms used as substitutions on Si sites) since doping plays a significant role in tuning the electronic and optical properties of such semiconducting nanomaterials are extended. There is systematic improvement in band structure and total energy with respect to the basis size and orbital optimisation. Not only the convergence is established with increasing the basis size but a great improvement in the quality with the optimisation of the contraction for a fixed basis size is shown; the double zeta polarised basis offers a reasonable approximation to study structural and electronic properties. This is most important to reduce the computational cost. The establishment of the transferability is equally interesting in order to put on a firm basis the use of NAOs as an efficient method, alternative to plane waves, to calculate

the properties of silicon nanowires. Here, using pre-optimised orbitals it is shown that this is possible in various silicon nanowires structures which can be used to address nanowire calculations in more complex (larger) environments.

This thesis started discussing the application of NAOs in calculations of transport properties by using a simple band analysis. It was concluded that once structural optimisation has been accurately performed, estimates of the mean free path are not significantly affected by the use of approximate NAOs whereas predictions of the conductivity can vary more extensively. This result allowed me to examine the scattering properties and the mean free path in silicon nanowires doped with n- and p-type dopant impurities. It is showed for the first time that the transport properties in nanowires with a small cross-section are determined not only by the dopant type but also by the wire axis orientation.

The relatively weak dependence of the mean free path on the NAO basis set has been confirmed (less than 0.01% between basis sets within an energy range of 0.2eV) in explicit calculations of quantum transport combining DFT with the Green's function formalism. For the case of weak scattering from impurities the choice of the NAOs basis is considerably less important than for impurities inducing strong backscattering. However, even in the case of suppressed transmission the double zeta polarised basis offers a good compromise whereas the single zeta basis set yields qualitatively correct results. We also assessed the impact of various numerical atomic orbital approximations on the transport properties of silicon nanowire setups with  $p^+ - n - p^+$  and  $p^+ - i - p^+$  doping profiles. Interestingly, although the current-voltage characteristics of such ultrascaled (3 nm length) nanowire-based transistors shows the expected sensitivity (from the conductivity estimates) to the choice of the NAOs basis set, it was found that charge self-consistency affects more significantly the on-

current. Regarding the possibility to use these devices, it is concluded that the source-drain tunneling currents are quite high – of the order of 0.5 nA and 2 nA for p-n-p junction and p-i-p junction, respectively) – to achieve good device performance.

Finally, motivated by recent experiments the hole mobility in <110>-oriented SiNWs of different widths (diameters in the range 1.15 nm to 4.47 nm) and nominally doped with boron (doping density  $\sim 10^{15} \text{ cm}^{-3}$ ) is calculated. To this end, we combined first-principles results on the band analysis and scattering from single impurities with the Boltzmann transport approach within the relaxation time approximation. In addition to our previous finding on the importance of the wire axis on the scattering properties of single dopants we have shown that there is interplay with dopant position and wire diameter regarding the effect of neutral dopant impurities in transport properties. Unlike earlier calculations, it has identified examples where backscattering and weak scattering may be observed when an impurity is placed either in the bulk or near the surface. Interestingly, for such low-doping concentrations the cut-off imposed by the Fermi-Dirac distribution function implies a weak dependence of the mobility from this effect (hence, also the basis set). This has as an effect that the hole mobility limited by neutral impurity scattering is determined predominantly by the nanowire width and the doping density. The hole mobility decreases monotonically with decreasing nanowire width at fixed doping density and increasing dopant concentration. Most importantly, it is shown that the mobility can show significant variations which can explain experimental observations.

Electronic quantum transport based on first-principles computational methods has become one of the core topics in atomic-scale modelling and device simulations.



Here, only the surface is scratched. On the one hand, there are fundamental issues like the systematic underestimation of the band gap by density functional theory which even accurate plane wave calculation cannot predict correctly. This requires extending the basic methodology to include many-body corrections to the description of electronic excitations. Although most of the results in this thesis do not depend on determining the band gap with experimental accuracy, this is a limiting factor of the computational methodology regarding interpretation of experiment, predictive strength and *a priori* technology evaluation. These issues form a large part of ongoing research. On the other hand, more simulations are needed to predict materials transport properties and electrical device characteristics for systems of experimental interest. For example, one should consider the effect of explicitly treating the oxide surrounding the silicon nanowires as well as core-shell structures to account for possible interface defects, recombination and charge traps. Regarding the various limiting scattering mechanisms to the mobility there is much more work to be done, including an analysis of ionised impurity scattering and a complete statistical analysis.

It is expected to have achieved in contributing our share by examining and establishing the use of numerical atomic orbital in predicting the electronic and transport properties of silicon nanowire structures from first-principles.

## 8. Bibliography

- (1) Guichard, A. R.; Barsic, D. N.; Sharma, S.; Kamins, T. I.; Brongersma, M. L. *Nano Lett* **2006**, 6, 2140.
- (2) Ansari, L.; Fagas, G.; Colinge, J.-P.; Greer, J. C. *Nano Lett* **2012**, 12, 2222.
- (3) Boukai, A. I.; Bunimovich, Y.; Tahir-Kheli, J.; Yu, J.-K.; Goddard Iii, W. A.; Heath, J. R. *Nature* **2008**, 451, 168.
- (4) Cui, Y.; Wei, Q. Q.; Park, H. K.; Lieber, C. M. *Science* **2001**, 293, 1289.
- (5) Hahm, J.; Lieber, C. M. *Nano Lett* **2004**, 4, 51.
- (6) Zheng, G. F.; Patolsky, F.; Cui, Y.; Wang, W. U.; Lieber, C. M. *Nat Biotechnol* **2005**, 23, 1294.
- (7) Yang, C.; Barrelet, C. J.; Capasso, F.; Lieber, C. M. *Nano Lett* **2006**, 6, 2929.
- (8) Cui, Y.; Zhong, Z.; Wang, D.; Wang, W. U.; Lieber, C. M. *Nano Lett* **2003**, 3, 149.
- (9) Singh, N.; Agarwal, A.; Bera, L. K.; Liow, T. Y.; Yang, R.; Rustagi, S. C.; Tung, C. H.; Kumar, R.; Lo, G. Q.; Balasubramanian, N.; Kwong, D. L. *Ieee Electr Device L* **2006**, 27, 383.
- (10) Song, Y.; Zhou, H.; Xu, Q.; Niu, J.; Yan, J.; Zhao, C.; Zhong, H. *Ieee Electr Device L* **2010**, 31, 1377.
- (11) Ginet, P.; Akiyama, S.; Takama, N.; Fujita, H.; Kim, B. *J Micromech Microeng* **2011**, 21, 065008.
- (12) Nah, J.; Liu, E.-S.; Varahramyan, K. M.; Shahrjerdi, D.; Banerjee, S. K.; Tutuc, E. *Ieee T Electron Dev* **2010**, 57, 491.
- (13) Wang, D. W.; Sheriff, B. A.; McAlpine, M.; Heath, J. R. *Nano Res* **2008**, 1, 9.
- (14) McAlpine, M. C.; Ahmad, H.; Wang, D.; Heath, J. R. *Nat Mater* **2007**, 6, 379.
- (15) Ionescu, A. M.; Riel, H. *Nature* **2011**, 479, 329.
- (16) Zhang, S.; Lou, L.; Lee, C. *Appl Phys Lett* **2012**, 100, 023111.
- (17) He, L.; Jiang, C.; Wang, H.; Lai, D.; Rusli. *Acs Applied Materials & Interfaces* **2012**, 4, 1704.
- (18) Ahn, J. H.; Choi, S. J.; Han, J. W.; Park, T. J.; Lee, S. Y.; Choi, Y. K. *Nano Lett* **2010**, 10, 2934.
- (19) In *Finfets and Other Multi-Gate Transistors*; Colinge, J. P., Ed. **2008**, p 1.
- (20) Wang, Y. F.; Lew, K. K.; Ho, T. T.; Pan, L.; Novak, S. W.; Dickey, E. C.; Redwing, J. M.; Mayer, T. S. *Nano Lett* **2005**, 5, 2139.
- (21) Colinge, J.-P. *Solid State Electron* **2004**, 48, 897.
- (22) Ma, D. D. D.; Lee, C. S.; Au, F. C. K.; Tong, S. Y.; Lee, S. T. *Science* **2003**, 299, 1874.
- (23) Singh, N.; Agarwal, A.; Bera, L. K.; Liow, T. Y.; Yang, R.; Rustagi, S. C.; Tung, C. H.; Kumar, R.; Lo, G. Q.; Balasubramanian, N.; Kwong, D. L. *Ieee Electr Device L* **2006**, 27, 383.
- (24) Mongillo, M.; Spathis, P.; Katsaros, G.; Gentile, P.; De Franceschi, S. *Nano Lett* **2012**, 12, 3074.
- (25) Za'bah, N. F.; Kwa, K. S. K.; Bowen, L.; Mendis, B.; O'Neill, A. *J Appl Phys* **2012**, 112, 024309.

- (26) Trivedi, K.; Yuk, H.; Floresca, H. C.; Kim, M. J.; Hu, W. *Nano Lett* **2011**, *11*, 1412.
- (27) Fukata, N.; Takiguchi, R.; Ishida, S.; Yokono, S.; Hishita, S.; Murakami, K. *Acs Nano* **2012**, *6*, 3278.
- (28) To, W.-K.; Tsang, C.-H.; Li, H.-H.; Huang, Z. *Nano Lett* **2011**, *11*, 5252.
- (29) Liu, Q. X.; Wang, C. X.; Xu, N. S.; Yang, G. W. *Phys Rev B* **2005**, *72*, 085417.
- (30) Yang, Y. H.; Wu, S. J.; Chin, H. S.; Lin, P. I.; Chen, Y. T. *J Phys Chem B* **2004**, *108*, 846.
- (31) Goldberger, J.; Hochbaum, A. I.; Fan, R.; Yang, P. *Nano Lett* **2006**, *6*, 973.
- (32) Garnett, E. C.; Yang, P. *J Am Chem Soc* **2008**, *130*, 9224.
- (33) Hofmann, S.; Ducati, C.; Neill, R. J.; Piscanec, S.; Ferrari, A. C.; Geng, J.; Dunin-Borkowski, R. E.; Robertson, J. *J Appl Phys* **2003**, *94*, 6005.
- (34) Heitsch, A. T.; Fanfair, D. D.; Tuan, H.-Y.; Korgel, B. A. *J Am Chem Soc* **2008**, *130*, 5436.
- (35) Jia, G. B.; Steglich, M.; Sill, I.; Falk, F. *Sol. Energy Mater. Sol. Cells* **2012**, *96*, 226.
- (36) Wang, N.; Tang, Y. H.; Zhang, Y. F.; Lee, C. S.; Bello, I.; Lee, S. T. *Chem Phys Lett* **1999**, *299*, 237.
- (37) Zhong, Z. H.; Wang, D. L.; Cui, Y.; Bockrath, M. W.; Lieber, C. M. *Science* **2003**, *302*, 1377.
- (38) Cui, Y.; Lieber, C. M. *Science* **2001**, *291*, 851.
- (39) Gao, A.; Lu, N.; Dai, P.; Li, T.; Pei, H.; Gao, X.; Gong, Y.; Wang, Y.; Fan, C. *Nano Lett* **2011**, *11*, 3974.
- (40) Patolsky, F.; Zheng, G.; Lieber, C. M. *Nat Protoc* **2006**, *1*, 1711.
- (41) Ng, H. T.; Han, J.; Yamada, T.; Nguyen, P.; Chen, Y. P.; Meyyappan, M. *Nano Lett* **2004**, *4*, 1247.
- (42) Garnett, E.; Yang, P. *Nano Lett* **2010**, *10*, 1082.
- (43) Kim, S.-K.; Day, R. W.; Cahoon, J. F.; Kempa, T. J.; Song, K.-D.; Park, H.-G.; Lieber, C. M. *Nano Letters* **2012**, *12*, 4971.
- (44) Peng, K.-Q.; Lee, S.-T. *Advanced Materials* **2011**, *23*, 198.
- (45) Chan, C. K.; Peng, H.; Liu, G.; McIlwrath, K.; Zhang, X. F.; Huggins, R. A.; Cui, Y. *Nat Nano* **2008**, *3*, 31.
- (46) Hahm, J.-i.; Lieber, C. M. *Nano Lett* **2003**, *4*, 51.
- (47) Gao, A.; Lu, N.; Dai, P.; Li, T.; Pei, H.; Gao, X.; Gong, Y.; Wang, Y.; Fan, C. *Nano Lett* **2011**, *11*, 3974.
- (48) Patolsky, F.; Zheng, G. F.; Hayden, O.; Lakadamyali, M.; Zhuang, X. W.; Lieber, C. M. *P Natl Acad Sci USA* **2004**, *101*, 14017.
- (49) Chiesa, M.; Cardenas, P. P.; Oton, F.; Martinez, J.; Mas-Torrent, M.; Garcia, F.; Alonso, J. C.; Rovira, C.; Garcia, R. *Nano Lett* **2012**, *12*, 1275.
- (50) Kim, A.; Ah, C. S.; Yu, H. Y.; Yang, J.-H.; Baek, I.-B.; Ahn, C.-G.; Park, C. W.; Jun, M. S.; Lee, S. *Appl Phys Lett* **2007**, *91*, 103901.
- (51) Ahn, J.-H.; Choi, S.-J.; Han, J.-W.; Park, T. J.; Lee, S. Y.; Choi, Y.-K. *Nano Lett* **2010**, *10*, 2934.
- (52) Gao, A.; Lu, N.; Wang, Y.; Dai, P.; Li, T.; Gao, X.; Wang, Y.; Fan, C. *Nano Lett* **2012**, *12*, 5262.
- (53) Mu; Shi; Chang, J. C.; Lee, S.-T. *Nano Lett* **2007**, *8*, 104.

- (54) Huang, Y.; Duan, X.; Cui, Y.; Lauhon, L. J.; Kim, K.-H.; Lieber, C. M. *Science* **2001**, 294, 1313.
- (55) Colinge, J.-P.; Lee, C.-W.; Afzalian, A.; Akhavan, N. D.; Yan, R.; Ferain, I.; Razavi, P.; O'Neill, B.; Blake, A.; White, M.; Kelleher, A.-M.; McCarthy, B.; Murphy, R. *Nat Nano* **2010**, 5, 225.
- (56) Moon, K.-J.; Lee, T.-I.; Lee, W.; Myoung, J.-M. *J Mater Chem* **2012**, 22, 1527.
- (57) Najmzadeh, M.; Bouvet, D.; Grabinski, W.; Ionescu, A. M. In *Solid-State Device Research Conference (ESSDERC), 2011 Proceedings of the European* **2011**, p 311.
- (58) Vo, T.; Williamson, A. J.; Galli, G. *Phys Rev B* **2006**, 74, 045116.
- (59) Read, A. J.; Needs, R. J.; Nash, K. J.; Canham, L. T.; Calcott, P. D. J.; Qteish, A. *Phys Rev Lett* **1992**, 69, 1232.
- (60) Yan, J.-A.; Yang, L.; Chou, M. Y. *Phys Rev B* **2007**, 76, 115319.
- (61) Svizhenko, A.; Leu, P. W.; Cho, K. *Phys Rev B* **2007**, 75, 125417.
- (62) Zhang, W.; Delerue, C.; Niquet, Y.-M.; Allan, G.; Wang, E. *Phys Rev B* **2010**, 82, 115319.
- (63) Kallesøe, C.; Wen, C.-Y.; Booth, T. J.; Hansen, O.; Bøggild, P.; Ross, F. M.; Mølhave, K. *Nano Lett* **2012**, 12, 2965.
- (64) Leu, P. W.; Svizhenko, A.; Cho, K. *Phys Rev B* **2008**, 77, 235305.
- (65) Nolan, M.; O'Callaghan, S.; Fagas, G.; Greer, J. C.; Frauenheim, T. *Nano Lett* **2006**, 7, 34.
- (66) Ng, M.-F.; Zhou, L.; Yang, S.-W.; Sim, L. Y.; Tan, V. B. C.; Wu, P. *Phys Rev B* **2007**, 76, 155435.
- (67) Ponomareva, I.; Menon, M.; Richter, E.; Andriotis, A. N. *Phys Rev B* **2006**, 74, 125311.
- (68) Svizhenko, A.; Leu, P. W.; Cho, K. *Phys Rev B* **2007**, 75, 125417.
- (69) Murphy-Armando, F.; Fagas, G.; Greer, J. C. *Nano Lett* **2010**, 10, 869.
- (70) Schmidt, V.; Senz, S.; Gösele, U. *Nano Lett* **2005**, 5, 931.
- (71) Migas, D. B.; Borisenko, V. E. *J Appl Phys* **2009**, 105, 104316.
- (72) Chan, T.-L.; Ciobanu, C. V.; Chuang, F.-C.; Lu, N.; Wang, C.-Z.; Ho, K.-M. *Nano Lett* **2006**, 6, 277.
- (73) Fernández-Serra, M. V.; Adessi, C.; Blase, X. *Nano Lett* **2006**, 6, 2674.
- (74) Markussen, T.; Rurali, R.; Jauho, A.-P.; Brandbyge, M. *Phys Rev Lett* **2007**, 99, 076803.
- (75) Fukata, N.; Ishida, S.; Yokono, S.; Takiguchi, R.; Chen, J.; Sekiguchi, T.; Murakami, K. *Nano Lett* **2011**, 11, 651.
- (76) Fagas, G.; Greer, J. C. *Nano Lett* **2009**, 9, 1856.
- (77) Rurali, R.; Markussen, T.; Suñé, J.; Brandbyge, M.; Jauho, A.-P. *Nano Lett* **2008**, 8, 2825.
- (78) Khanal, D. R.; Levander, A. X.; Yu, K. M.; Liliental-Weber, Z.; Walukiewicz, W.; Grandal, J.; Sanchez-Garcia, M. A.; Calleja, E.; Wu, J. *J Appl Phys* **2011**, 110, 033705.
- (79) Neophytou, N.; Kosina, H. *Appl Phys Lett* **2011**, 99, 092110.
- (80) Shin, M. *Appl Phys Lett* **2011**, 99, 143503.
- (81) Luisier, M.; Schenk, A.; Fichtner, W. *Appl Phys Lett* **2007**, 90, 102103.
- (82) Rurali, R. *Reviews of Modern Physics* **2010**, 82, 427.

- (83) Ansari, L.; Feldman, B.; Fagas, G.; Colinge, J.-P.; Greer, J. C. *Appl Phys Lett* **2010**, *97*, 062105.
- (84) Ansari, L.; Feldman, B.; Fagas, G.; Colinge, J.-P.; Greer, J. C. *Solid State Electron* **2012**, *71*, 58.
- (85) Kohn, W.; Sham, L. J. *Physical Review* **1965**, *140*, 1133.
- (86) Payne, M. C.; Teter, M. P.; Allan, D. C.; Arias, T. A.; Joannopoulos, J. D. *Reviews of Modern Physics* **1992**, *64*, 1045.
- (87) Kresse, G.; Furthmüller, J. *Phys Rev B* **1996**, *54*, 11169.
- (88) Galli, G.; Parrinello, M. *Phys Rev Lett* **1992**, *69*, 3547.
- (89) Junquera, J.; Paz, Ó.; Sánchez-Portal, D.; Artacho, E. *Phys Rev B* **2001**, *64*, 235111.
- (90) Talman, J. D. *Phys Rev Lett* **2000**, *84*, 855.
- (91) Kenny, S. D.; Horsfield, A. P.; Fujitani, H. *Phys Rev B* **2000**, *62*, 4899.
- (92) Ozaki, T.; Kino, H. *Phys Rev B* **2004**, *69*, 195112.
- (93) Ozaki, T.; Kino, H. *J Chem Phys* **2004**, *121*, 10879.
- (94) Driscoll, J. A.; Varga, K. *Phys Rev B* **2010**, *81*, 115412.
- (95) Strange, M.; Kristensen, I. S.; Thygesen, K. S.; Jacobsen, K. W. *J Chem Phys* **2008**, *128*, 114714.
- (96) Hohenberg, P.; Kohn, W. *Phys Rev B* **1964**, *136*, B864.
- (97) Jones, R. O.; Gunnarsson, O. *Reviews of Modern Physics* **1989**, *61*, 689.
- (98) Slater, J. C. *Physical Review* **1951**, *81*, 385.
- (99) Goedecker, S. *Reviews of Modern Physics* **1999**, *71*, 1085.
- (100) Ordejon, P.; Drabold, D. A.; Martin, R. M.; Grumbac, M. P. *Phys Rev B* **1995**, *51*, 1456.
- (101) Ordejon, P. *Comp Mater Sci* **1998**, *12*, 157.
- (102) Skylaris, C. K.; Haynes, P. D.; Mostofi, A. A.; Payne, M. C. *J Chem Phys* **2005**, *122*, 084119.
- (103) Huzinaga, S. *Computer Physics reports* **1985**, *2*, 281.
- (104) Blum, V.; Gehrke, R.; Hanke, F.; Havu, P.; Havu, V.; Ren, X.; Reuter, K.; Scheffler, M. *Comput Phys Commun* **2009**, *180*, 2175.
- (105) Soler, J. M.; Artacho, E.; Gale, J. D.; Garcia, A.; Junquera, J.; Ordejon, P.; Sanchez-Portal, D. *J Phys-Condens Mat* **2002**, *14*, 2745.
- (106) Artacho, E.; Anglada, E.; Dieguez, O.; Gale, J. D.; Garcia, A.; Junquera, J.; Martin, R. M.; Ordejon, P.; Pruneda, J. M.; Sanchez-Portal, D.; Soler, J. M. *J Phys-Condens Mat* **2008**, *20*, 2745.
- (107) Skylaris, C. K.; Haynes, P. D.; Mostofi, A. A.; Payne, M. C. *J Phys-Condens Mat* **2005**, *17*, 5757.
- (108) Mostofi, A. A.; Haynes, P. D.; Skylaris, C. K.; Payne, M. C. *Mol Simulat* **2007**, *33*, 551.
- (109) Elstner, M.; Frauenheim, T.; Kaxiras, E.; Seifert, G.; Suhai, S. *Phys Status Solidi B* **2000**, *217*, 357.
- (110) Junquera, J.; Paz, O.; Sanchez-Portal, D.; Artacho, E. *Phys Rev B* **2001**, *64*, 235111.
- (111) Ozaki, T. *Phys. Rev. B* **2003**, *67*, 155108.
- (112) Gusso, M. *J Chem Phys* **2008**, *128*, 044102.
- (113) Talman, J. D. *Physical Review A* **2010**, *82*, 052518.
- (114) Landauer, R. *J. Math. Phys.* **1996**, *37*, 5259.

- (115) Ke, S. H.; Baranger, H. U.; Yang, W. T. *Phys Rev B* **2004**, 70, 085410.
- (116) Giannozzi, P.; Baroni, S.; Bonini, N.; Calandra, M.; Car, R.; Cavazzoni, C.; Ceresoli, D.; Chiarotti, G. L.; Cococcioni, M.; Dabo, I.; Dal Corso, A.; de Gironcoli, S.; Fabris, S.; Fratesi, G.; Gebauer, R.; Gerstmann, U.; Gougoussis, C.; Kokalj, A.; Lazzeri, M.; Martin-Samos, L.; Marzari, N.; Mauri, F.; Mazzarello, R.; Paolini, S.; Pasquarello, A.; Paulatto, L.; Sbraccia, C.; Scandolo, S.; Schlauzero, G.; Seitsonen, A. P.; Smogunov, A.; Umari, P.; Wentzcovitch, R. M. *J Phys-Condens Mat* **2009**, 21, 395502.
- (117) Elstner, M.; Porezag, D.; Jungnickel, G.; Elsner, J.; Haugk, M.; Frauenheim, T.; Suhai, S.; Seifert, G. *Phys Rev B* **1998**, 58, 7260.
- (118) Shelley, M.; Poilvert, N.; Mostofi, A. A.; Marzari, N. *Comput Phys Commun* **2011**, 182, 2174.
- (119) Brandbyge, M.; Mozos, J.-L.; Ordejón, P.; Taylor, J.; Stokbro, K. *Phys Rev B* **2002**, 65, 165401.
- (120) Rungger, I.; Sanvito, S. *Phys Rev B* **2008**, 78, 035407.
- (121) Lee, B.; Rudd, R. E. *Phys Rev B* **2007**, 75, 195328.
- (122) Nelson, J. S.; Stechel, E. B.; Wright, A. F.; Plimpton, S. J.; Schultz, P. A.; Sears, M. P. *Phys Rev B* **1995**, 52, 9354.
- (123) Kresse, G.; Hafner, J. *Phys Rev B* **1994**, 49, 14251.
- (124) Read, A. J.; Needs, R. J.; Nash, K. J.; Canham, L. T.; Calcott, P. D. J.; Qteish, A. *Phys Rev Lett* **1992**, 69, 1232.
- (125) Kaschner, R.; Frauenheim, T.; Köhler, T.; Seifert, G. *J Comput-Aided Mater* **1997**, 4, 53.
- (126) Liu, F.; Garofalini, S. H.; Kingsmith, D.; Vanderbilt, D. *Phys Rev B* **1994**, 49, 12528.
- (127) Heinrichs, J. *Phys Rev B* **2007**, 76, 033305.
- (128) Cui, Y.; Duan, X. F.; Hu, J. T.; Lieber, C. M. *J Phys Chem B* **2000**, 104, 5213.
- (129) Vallett, A. L.; Minassian, S.; Kaszuba, P.; Datta, S.; Redwing, J. M.; Mayer, T. S. *Nano Lett* **2010**, 10, 4813.
- (130) Declerck, G. In *VLSI Technology, 2005. Digest of Technical Papers. 2005 Symposium on* **2005**, p 6.
- (131) Philip Wong, H. S. *Solid State Electron* **2005**, 49, 755.
- (132) Van Wees, B. J.; van Houten, H.; Beenakker, C. W. J.; Williamson, J. G.; Kouwenhoven, L. P.; van der Marel, D.; Foxon, C. T. *Phys Rev Lett* **1988**, 60, 848.
- (133) Colinge, J. P. *Microelectron Eng* **2007**, 84, 2071.
- (134) Pan, H.; Feng, Y. P. *Acs Nano* **2008**, 2, 2410.
- (135) Tseng, G. Y.; Ellenbogen, J. C. *Science* **2001**, 294, 1293.
- (136) Davari, B.; Dennard, R. H.; Shahidi, G. G. *Proceedings of the IEEE* **1995**, 83, 595.
- (137) Hu, J.; Odom, T.; Lieber\*, C. *Acc. Chem. Res.* **1999**, 32, 435.
- (138) Rurali, R.; Aradi, B.; Frauenheim, T.; Gali, Á. *Phys Rev B* **2009**, 79, 115303.
- (139) Ferain, I.; Colinge, C. A.; Colinge, J.-P. *Nature* **2011**, 479, 310.
- (140) Singh, A. K.; Kumar, V.; Note, R.; Kawazoe, Y. *Nano Lett* **2006**, 6, 920.
- (141) Seifert, G.; Porezag, D.; Frauenheim, T. *Int J Quantum Chem* **1996**, 58, 185.

- (142) Jancu, J.-M.; Scholz, R.; Beltram, F.; Bassani, F. *Phys Rev B* **1998**, 57, 6493.
- (143) Bauschlicher Jr, C. W.; Lawson, J. W.; Ricca, A.; Xue, Y.; Ratner, M. A. *Chem Phys Lett* **2004**, 388, 427.
- (144) Herrmann, C.; Solomon, G. C.; Subotnik, J. E.; Mujica, V.; Ratner, M. A. *The Journal of Chemical Physics* **2010**, 132, 024103.
- (145) Sharma, D.; Arefi, H. H.; Fagas, G. *Computational and Theoretical Chemistry* **2012**, 991, 32.
- (146) Markussen, T.; Rurali, R.; Jauho, A. P.; Brandbyge, M. *Phys Rev Lett* **2007**, 99, 076803.
- (147) Cui, Y.; Duan, X.; Hu, J.; Lieber, C. M. *The Journal of Physical Chemistry B* **2000**, 104, 5213.
- (148) Bjork, M. T.; Schmid, H.; Knoch, J.; Riel, H.; Riess, W. *Nat Nano* **2009**, 4, 103.
- (149) Jiezhi, C.; Saraya, T.; Kousuke, M.; Shimizu, K.; Hiramoto, T. In *VLSI Technology, 2008 Symposium on* **2008**, p 32.
- (150) Packan, P.; Cea, S.; Deshpande, H.; Ghani, T.; Giles, M.; Golonzka, O.; Hattendorf, M.; Kotlyar, R.; Kuhn, K.; Murthy, A.; Ranade, P.; Shifren, L.; Weber, C.; Zawadzki, K. In *Electron Devices Meeting. IEDM 2008. IEEE International* **2008**, p 1.
- (151) Buin, A. K.; Verma, A.; Svizhenko, A.; Anantram, M. P. *Nano Lett* **2008**, 8, 760.
- (152) Harris, C.; O'Reilly, E. P. *Physica E: Low-dimensional Systems and Nanostructures* **2006**, 32, 341.
- (153) Migita, S; Morita, Y; Masahara, M; Ota, H, International Electron Devices Meeting (IEDM) **2012** pp. 191-194.
- (154) Electronic Structure: Basic Theory and Practical Methods by Martin, M, Richard Cambridge University Press **2004**.
- (155) Electronic transport in mesoscopic systems by Datta, Supriyo, Cambridge University Press **1999**.
- (156) <http://www.openmx-square.org/>
- (157) Semiconductor Physics: An Introduction by Seeger, K Springer-Verlag Berlin Heidelberg New York 9<sup>th</sup> Edition.